Journal of
Materials Chemistry A

ROYAL SOCIETY
OF CHEMISTRY

REVIEW

View Article Online
View Journal | View Issue

Check for updates

Cite this: *J. Mater. Chem. A*, 2025, **13**, 2537

Fluorinated catalysts for the oxygen evolution reaction: a comprehensive review of synthesis, structure, and performance

Zhiping Luo

Electrochemical water splitting is considered one of the most viable, effective, and environmentally friendly approaches for renewable energy conversion and storage. Nevertheless, due to its slow reaction kinetics, the oxygen evolution reaction (OER) at the anode remains a significant challenge. Researchers have discovered that incorporating fluorine into catalysts in the past few years can significantly improve their OER performance. This enhancement is attributed to fluorine's unique characteristic of possessing the highest electronegativity among all the elements. Consequently, fluorine forms highly ionic metal–fluorine bonds, which promote the electrocatalytic reactions necessary for the OER. This approach has led to considerable advancements in catalyst development for OER applications. This review encompasses various types of state-of-the-art fluorinated catalysts, including binary, ternary, and high-entropy transition-metal fluorides, oxyfluorides, fluorinated versions of oxides, (oxy)hydroxides, carbonate hydroxides, carbides, nitrides, phosphides, sulfides, and carbons. Research has shown that fluorine-containing catalysts demonstrate exceptional performance in the OER, with some outperforming industry standards such as IrO_2 or RuO_2. Incorporating fluorine through doping has emerged as a successful approach to enhance the OER performance of catalysts, significantly decreasing the overpotential and Tafel slope while improving durability. The data indicate that fluorination leads to an average reduction of 21.6% in overpotential and 29.6% in the Tafel slope. When a new OER catalyst is developed, improving its OER performance through fluorination might be worth exploring if this has not been done. The OER performances of these catalysts are closely linked to their synthesis methods and structural characteristics.

Received 22nd September 2024
Accepted 19th November 2024

DOI: 10.1039/d4ta06767c

rsc.li/materials-a

1. Introduction

With the rapidly increasing global demand for energy consumption, reliance on traditional fossil fuels has led to an energy crisis due to their gradual depletion and the environmental pollution they cause when burned. Consequently, scientists are actively seeking alternative clean and renewable energy sources. Electrochemical water splitting is considered to be one of the most viable, effective, and eco-friendly approaches for renewable energy conversion and storage.[1,2] The hydrogen produced through this process is a clean, renewable, and energy-efficient fuel, offering a way to store renewable energy and overcome its intermittency.[3] The water-splitting process involves the oxygen evolution reaction (OER) at the anode and the hydrogen evolution reaction (HER) at the cathode. The OER is particularly critical and kinetically sluggish due to its complex four-electron transfer. Currently, IrO_2 and RuO_2 are the most effective OER catalysts; however, their high costs limit the scalability of this technology. Thus, finding highly efficient catalysts from earth-abundant materials is of significant scientific and technological importance.

Significant progress has been made in identifying efficient OER catalysts, including Group IA compounds (hydrates), Group IVA compounds (carbon-based catalysts and silicates), Group VA pnictogenides (nitrides and phosphides), Group VIA compounds (oxides, sulfides, and selenides), and Group VIIA compounds (fluorides and chlorides).[2,4–8] Among them, oxides are the most extensively studied catalysts due to their high performance, wide availability, and lasting durability.

In the early stage of OER catalyst development, metal fluorides did not attract much attention for OER catalysts because of their low conductivity of pure fluorides M_xF_y.[9–11] In recent years, researchers have recognized the merits of fluorine (F) because of its unique features that may have significant potential impacts on the OER process. With the highest electronegativity (3.98) and a similar ionic radius to O ions (F 1.31 Å and O 1.38 Å), fluorine is an ideal n-type dopant,[12] which forms weak metal–F bonds compared to metal–O bonds in oxides.[12–14] These weak metal–F bonds exhibiting higher ionic character can be readily dissociated in the electrolyte, facilitating surface reconstruction (SR).[15,16] For example, a binary cobalt fluoride

---

Department of Chemistry, Physics and Materials Science, Fayetteville State University, Fayetteville, North Carolina 28301, USA. E-mail: zluo@uncfsu.edu

(CoF_2) nanorod catalyst, even without doping, requires only 285 mV overpotential to achieve 10 mA cm^{-2} current density, outperforming the benchmark IrO_2 catalyst, which requires 310 mV in the experiment.[9] However, serious corrosion of the fluorides occurred by forming oxidation layers on the surface of the fluorides. The low conductivity and corrosion resistance of fluoride catalysts with low structural stability limit their OER applications.

To improve the OER performance of metal fluorides, several materials design strategies have been proposed, including synthesizing nanostructured morphology,[9,15] surface reconstruction,[15–17] heteroatomic doping,[10,17–19] and hybrid heterocatalysts.[20] Nanostructured surfaces expose more active sites to facilitate proton transport and the OER. For instance, a surface-reconstructed NiFe-OH-F-SR catalyst exhibits higher electrical conductivity than the original NiFe-OH-F.[15] Following fluoride leaching under OER conditions, the surface undergoes self-reconstruction, resulting in a highly porous and amorphous NiFe oxide structure with a hierarchical arrangement. This transformation leads to a substantial 58-fold enhancement in OER activity at 220 mV. Fe doping in CoF_2 nanowires reduces the overpotential at 10 mA cm^{-2} from 300 mV to 230 mV and Tafel slope from 82 to 59 mV dec^{-1}, with improved stability.[18] The doped Fe^{3+} to this fluoride is thought to create more defects and provide more catalytically active sites, thus improving the OER catalytic activities. The nanosheet structure formed after the stability test favored rapid electron conduction. In $KNi_xCo_{1-x}F_3$ perovskite fluoride, Ni species enhance electrochemical activity and Co species improve the electronic conductivity and electrochemical stability, leading to superior OER performance compared to RuO_2.[17] Fe-doped $KCo_{0.8}Fe_{0.2}F_3$ also demonstrates superior OER performance due to the enhanced conductivity of Fe species and the synergistic effect of Fe and Co.[19] Additionally, incorporating oxygen into metal fluorides to form oxyfluoride ($M_xO_yF_z$) can enhance electronic conductivity while preserving key characteristics for the OER.[10] As an example, a hybrid heterocatalyst composed of mixed Fe_2O_3 and FeF_2 shows superior OER properties compared to Fe_2O_3 alone, due to the higher electroconductivity enabled by the coexistence of Fe–O and Fe–F bands.[20]

Besides using transition-metal (TM) fluorides as effective OER catalysts, another strategy is doping F into existing OER catalysts. For example, Chen *et al.* introduced F into Co-based catalysts (CoOOH and Co_3O_4).[13] Benefiting from the strong ionicity of weak metal–F bonds, a dynamic migration of F anions from the interior to the surface was observed, significantly enhancing OER activity. The overpotential of F-doped CoOOH was reduced from 370 to 310 mV at 50 mA cm^{-2}, a reduction of 16.2%. For F-doped Co_3O_4, the overpotential decreased from 460 to 370 mV, a reduction of 19.6%. The Tafel slope was reduced from 83 to 54 mV dec^{-1} for CoOOH, a reduction of 34.9%, and from 160 to 70 mV dec^{-1} for Co_3O_4, a reduction of 56.3%. In another study, the F doping of a $NiTiO_3$/C catalyst reduced the overpotential from 680 mV to 270 mV at 50 mA cm^{-2}, a reduction as high as 60.3%.[21] Successful fluorination across various catalysts appears to be a promising strategy for further enhancing the OER activity.

Given the high performance of fluorinated catalysts, this paper comprehensively reviews current fluorinated catalysts for the OER. First, it outlines the benefits of fluorination, such as highly ionic metal–fluorine bonds for the OER, improved electrical conductivity, water wettability, surface reconstruction, reduced energy barriers, optimized band structure, and favorable charge redistribution. The review then details the high performance of specific fluorinated catalysts, including TM fluorides, oxyfluorides, and various fluorinated catalysts. The strategies for fluorinating these catalysts and their structural modulations are discussed, highlighting the significant enhancements in OER properties due to fluorination.

2. Benefits of fluorination

2.1 OER mechanism

To understand the impacts of fluoridation, we first review the OER mechanisms. During the OER process, O_2 is formed from H_2O on the anode side through four steps involving coupled electron–proton transfer processes:

$$2H_2O \rightarrow O_2 + 4H^+ + 4e^- \quad (1)$$

Several OER mechanisms have been proposed in the literature.[5,22–24] Here, we present the well-accepted adsorbate evolution mechanism (AEM) and lattice oxygen mechanism or lattice oxygen-participation mechanism (LOM), as illustrated in Fig. 1. In an acidic medium, as shown in Fig. 1a, the AEM involves the following steps:[23,24]

$$\text{Step 1: } * + H_2O\ (l) \rightarrow *OH + H^+ + e^- \quad (2)$$

$$\text{Step 2: } *OH \rightarrow *O + H^+ + e^- \quad (3)$$

$$\text{Step 3: } *O + H_2O\ (l) \rightarrow *OOH + H^+ + e^- \quad (4)$$

$$\text{Step 4: } *OOH \rightarrow * + O_2\ (g) + H^+ + e^- \quad (5)$$

where * represents the active site of the catalyst and l and g denote the liquid and gas states, respectively.

In an alkaline medium, as shown in Fig. 1b, the AEM is composed of these reactions:[24]

$$\text{Step 1: } * + OH^- \rightarrow *OH + e^- \quad (6)$$

$$\text{Step 2: } *OH + OH^- \rightarrow *O + H_2O\ (l) + e^- \quad (7)$$

$$\text{Step 3: } *O + OH^- \rightarrow *OOH + e^- \quad (8)$$

$$\text{Step 4: } *OOH + OH^- \rightarrow * + O_2\ (g) + H_2O\ (l) + e^- \quad (9)$$

The LOM requires the presence of oxygen in the lattice to form an oxygen vacancy through coupling.[25–27] In the acidic medium, as illustrated in Fig. 1c, the LOM can be described by the following reactions:[27]

$$\text{Step 1: } M\text{–}O_L + H_2O \rightarrow M\text{–}O_LOH + H^+ + e^- \quad (10)$$

$$\text{Step 2: } M\text{–}O_LOH \rightarrow M\text{–}O_LO + H^+ + e^- \quad (11)$$

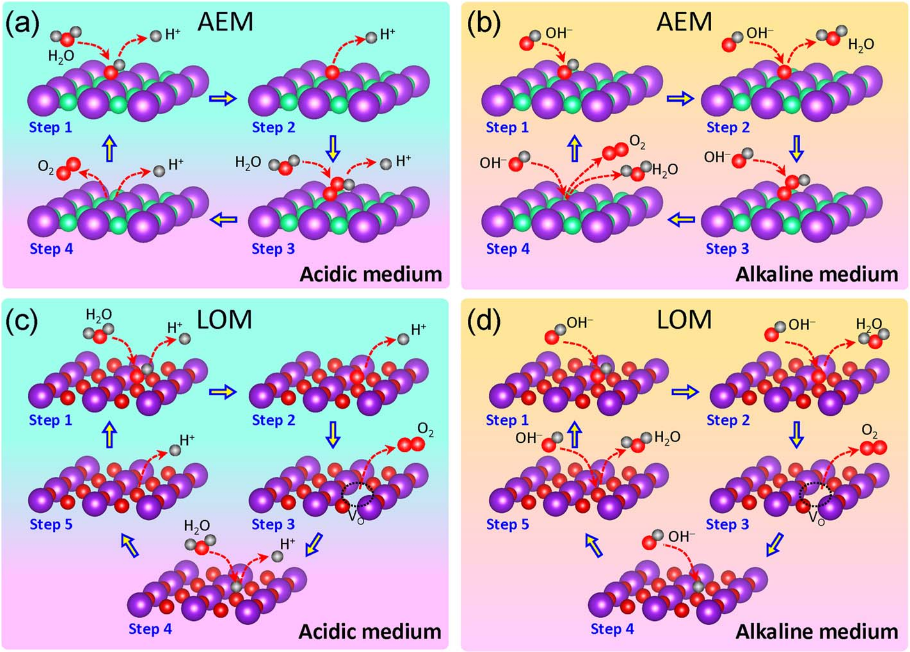

Fig. 1 AEM in acidic (a) and alkaline media (b), and LOM in acidic (c) and alkaline media (d). Arrows pointing toward the active catalyst surface indicate reactants, while arrows pointing away from the catalyst surface represent products. Each atomic configuration shown in the figure corresponds to the post-reaction state at each step. Electrons are not depicted in the figure.

$$\text{Step 3: M–O}_L\text{O} \rightarrow \text{M–V}_O + \text{O}_2\text{ (g)} \quad (12)$$

$$\text{Step 4: M–V}_O + \text{H}_2\text{O} \rightarrow \text{M–O}_L\text{H} + \text{H}^+ + \text{e}^- \quad (13)$$

$$\text{Step 5: M–O}_L\text{H} \rightarrow \text{M–O}_L + \text{H}^+ + \text{e}^- \quad (14)$$

where M represents the catalyst matrix, O_L is lattice oxygen, and V_O is an oxygen vacancy.

In the alkaline medium, as illustrated in Fig. 1d, the LOM reactions are as follow:[28,29]

$$\text{Step 1: M–O}_L + \text{OH}^- \rightarrow \text{M–O}_L\text{OH} + \text{e}^- \quad (15)$$

$$\text{Step 2: M–O}_L\text{OH} + \text{OH}^- \rightarrow \text{M–O}_L\text{O} + \text{H}_2\text{O} + \text{e}^- \quad (16)$$

$$\text{Step 3: M–O}_L\text{O} \rightarrow \text{M–V}_O + \text{O}_2\text{ (g)} \quad (17)$$

$$\text{Step 4: M–V}_O + \text{OH}^- \rightarrow \text{M–O}_L\text{H} + \text{e}^- \quad (18)$$

$$\text{Step 5: M–O}_L\text{H} + \text{OH}^- \rightarrow \text{M–O}_L + \text{H}_2\text{O} + \text{e}^- \quad (19)$$

Alternative LOM pathways have also been reported in the literature.[29,30]

It should be noted that the AEM does not require lattice oxygen within the catalyst structure, making it broadly applicable across various catalyst materials, including those without inherent oxygen content, such as pure fluorides, pure or fluorinated carbides, nitrides, phosphides, sulfides, and carbons. In contrast, the LOM specifically involves the active participation of lattice oxygen in the reaction, limiting its applicability to catalysts with accessible lattice oxygen, such as oxyfluorides, fluorinated oxides, (oxy)hydroxides, and carbonate hydroxides. Further discussions of the AEM and LOM are provided in the following sections.

2.2 Impacts of fluorination

Due to fluorine's unique property of having the highest electronegativity, fluorinating catalysts can have several evident impacts on OER performance as follows:

(1) Highly ionic metal–fluorine bonds favorable for the OER. Fluorine has the highest electronegativity, which forms high ionic metal–fluorine bonds.[13] Tong *et al.* found that the weak metal–F bond is easy to break, forming active species of oxides or hydroxides and thus improving OER performance.[31] Prakash *et al.* found that the highly polarized M–F (M = Co, Ni) bonds favor the dissociation of the M–F bonds to form a metal hydroxide phase $M(OH)_2$, which can be oxidized into a higher valence oxyhydroxide MOOH, promoting the OER activity.[17]

(2) Improved electrical conductivity. Fluorination has been found to enhance electrical conductivity in various catalyst materials, which is favorable for OER activities. Wang *et al.* observed that F-doping in Fe_2O_3 remarkably increases the charge carrier concentration and conductivity, facilitating rapid charge transfer.[32] Xu *et al.* demonstrated that F-doped F–Ni_3S_2 exhibits intrinsic conductivity superior to Ni_3S_2, as shown through the cyclic voltammetry (CV) test.[33] Similarly, F-containing $PrBaFe_2O_{5+\delta}F_{0.1}$ (PBFOF) has higher conductivity than $PrBaFe_2O_{5+\delta}$ (PBF).[34] Density functional theory (DFT) calculations also suggest that F-doping increases the state density of the Ni 3d orbital around the Fermi level, enhancing the conductivity of NiFeOOH.[35]

(3) Improved water wettability on the catalyst surface. A hydrophilic surface favors contact between reactants and active sites, facilitating the release of O_2 gas bubbles and electron

transfers during the OER process. Chen *et al.* measured the water contact angle of nonfluorinated CoOOH at 62.9°, whereas fluorinated CoOOH showed a reduced angle of 44.6°, indicating enhanced hydrophilicity.[13] Both samples have a nanosheet morphology, while the fluorinated nanosheets are more hydrophilic for water absorption, boosting O-related intermediate adsorption. Li *et al.* synthesized surface-smooth Ni_3S_2 nanoarrays that, after fluorination, became rough due to surface reconstruction.[33] The water contact angle changed from 73° for the nonfluorinated sample to 0° for the fluorinated one, significantly improving wettability, as shown in Fig. 2a. The improved wettability contributes to the augmented OER.

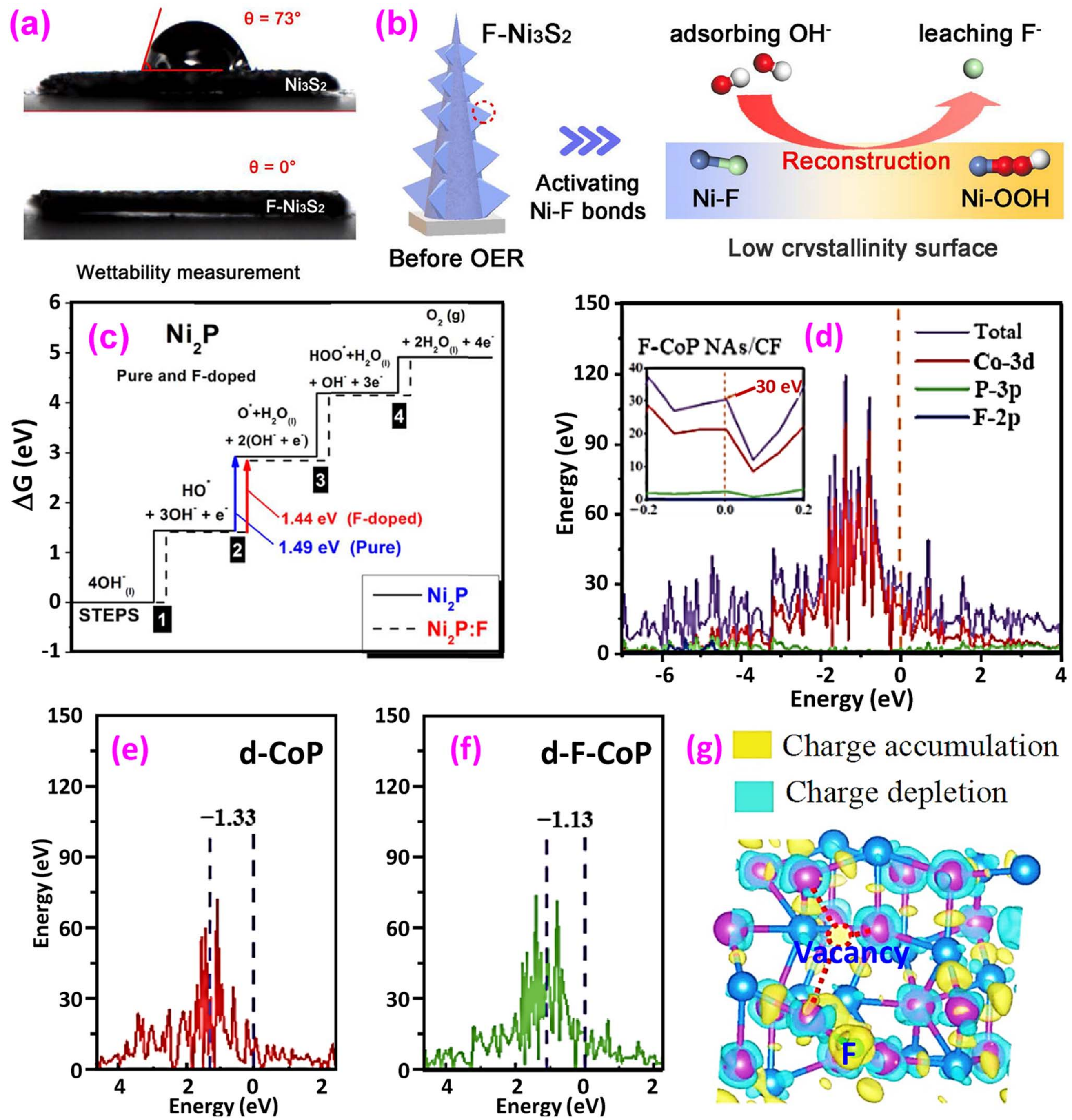

Fig. 2 Impacts of fluorination. (a) The fluorinated sample exhibits a hydrophilic nature with good wettability (bottom), while the nonfluorinated sample displays a hydrophobic nature, with a droplet remaining on the surface and (b) F-induced surface reconstruction during the OER. Reproduced from ref. 33 with permission from Elsevier, copyright 2021. (c) Calculated Gibbs free energy of the intermediate reactions for pure and F-doped Ni_2P. Reproduced from ref. 36 with permission from IOP Publishing, copyright 2021. (d) DOS of fluorinated CoP; (e and f) projected DOS for the d-bands of pristine and fluorinated CoP, respectively and (g) charge density difference distribution. Reproduced from ref. 37 with permission from Springer Nature, copyright 2022.

(4) Promoted surface reconstruction. Surface reconstruction plays a crucial role in the OER process.[38,39] Since the high electronegativity of F causes weakened metal–F bonding in the electrolyte, SR is a notable feature of fluorinated catalysts. Hu *et al.* incorporated F^- into NiFe hydroxide (NiF–OH–F) nanosheet arrays for the OER.[15] Following the OER testing, they noted SR triggered by fluorine leaching under OER conditions, and a highly mesoporous and amorphous NiFe oxide structure with a hierarchical arrangement is formed after the surface reconstruction. Notably, the surface reconstructed product NiFe–OH–F-SR showed enhanced OER activity with a reduced overpotential of 181 mV at 10 mA cm^{-2}, compared to the 243 mV of NiFe–OH–F. Li *et al.* also identified SR in fluorinated Ni_3S_2 (Fig. 2b).[33] It was found that Ni–F bonds are easily activated with F loss under OER conditions, producing highly active Ni–OOH species to accelerate the rate-determining step (RDS, *O → *OOH in Fig. 1). SR has also been reported in other systems.[15,37,40–47]

(5) Reduced energy barriers to the OER. The reactions described in eqn (2)–(19) require external overpotential to proceed. Fluorination has been shown to reduce these energy barriers, as demonstrated using DFT calculations. For example, Kumta *et al.* calculated the Gibbs free energies of pure and F-doped Ni_2P, as shown in Fig. 2c.[36] For both materials, the RDS is Step 2, the largest of the other elementary steps contributing to the OER. However, F-doping reduced this energy from 1.49 eV to 1.44 eV, thus reducing the overpotential and improving the electrocatalytic activity. Other examples are reported in the literature, and some are discussed in the following sections.

(6) Optimized band structure. DFT calculations have revealed optimized electronic band structures of fluorinated materials. The density of states (DOS) of fluorinated CoP is shown in Fig. 2d.[37] DOS density at the Fermi level is intimately connected with the material's electrical conductivity. It is found that the DOS of F-CoP (30 eV) is significantly higher than that of CoP (16 eV) at the Fermi level, indicating a rapid charge-transfer process for accelerated electrocatalytic reactions. Furthermore, the d-band center of the 3d Co element is calculated using

$$\varepsilon_d = \int_{-\infty}^{\infty} x\rho(x)\mathrm{d}x \bigg/ \int_{-\infty}^{\infty} \rho(x)\mathrm{d}x \tag{20}$$

It is found that $\varepsilon_d = -1.33$ eV for CoP (Fig. 2e), while it is upshifted to $\varepsilon_d = -1.13$ eV for F-CoP (Fig. 2f). The d-band center is used to predict the adsorption of small molecules, and the upshift induces less electron filling in the antibonding states for strengthened OH^- adsorption and improved OER performance. Kumta *et al.* revealed by calculation that the d-band center of pure Ni_2P is −1.84 eV, while for F-doped $Ni_2P_{0.67}F_{0.33}$, its d-band center upshifts to −1.45 eV.[36] Zhao *et al.* calculated the d-band center of NiOOH/NiF_2 ($\varepsilon_d = -2.341$ eV), $Ni_{0.5}Co_{0.5}OOH/(NiCo)F_2$ ($\varepsilon_d = -2.177$ eV), and CoOOH/CoF_2 ($\varepsilon_d = -1.717$ eV), respectively.[46] Although the last material has the highest ε_d, the optimum OER is found for the second material containing Ni and Co. The hypothesis suggests that a highly elevated d-band center, which results in powerful adsorption, actually hinders the subsequent evolution reaction by increasing the energy barrier of the RDS. The bimetallic fluoride has the balanced d-band center for the OER, consistent with the free energy calculation that the bimetallic fluoride has the lowest energy (1.49 eV) for forming *O, the RDS in the OER. F atoms are observed as electron traders, facilitating electron transfer from CoF_2 to Ru sites and inducing charge accumulation at the interface.[48]

(7) Favorable charge redistribution. DFT calculations have revealed charge redistribution by fluorination, which benefits the OER. The charge density difference of F-doped CoP is shown in Fig. 2g.[37] Charge accumulation is found on the F site and near the P vacancy, which favors H capture electrons, improving the HER. Nevertheless, the Co site experiences a reduction in charge, which increases the likelihood of OH losing electrons, thereby promoting the OER. In the NiCo bimetallic fluoride, the Co site exhibits more significant charge deficiency than individual Ni or Co fluorides, suggesting the presence of higher valence metal sites that enhance surface reconstruction and OER kinetics.[46]

It should be noted that these impacts, as mentioned earlier, of fluorination are indeed frequently interconnected with the electronic properties induced by the fluorination process.

2.3 Enhancement of OER activities by fluorination

F-containing catalysts have exhibited high OER performance; some surpass the benchmark catalysts, IrO_2 or RuO_2. Composed of earth-abundant elements, these catalysts are promising candidates for future applications. In particular, the F-doping has been demonstrated to be an effective strategy for boosting the OER of catalysts. With F-doping, both the overpotential and Tafel slopes can be significantly reduced, as shown in Fig. 3 for different types of catalysts, according to the literature results summarized in this review. From the available literature data, the overpotential is reduced by an average of 21.6%, and the Tafel slope is reduced by 29.6%.

In the following sections, we specifically demonstrate the enhancement of the OER by fluorination in various types of catalysts, including transition-metal fluorides (Section 3); fluoride-oxides (Section 4); (oxy)hydroxides, carbonate hydroxides, and their derived fluorides (Section 5); carbides, nitrides, phosphides, and sulfides (Section 6); and carbon-based catalysts (Section 7). The role of F in these catalysts will be highlighted.

3. Transition-metal fluorides

Although noble-metal-based electrocatalysts have been considered the most potent for the OER, their high costs and limited structural stability in both acidic and alkaline electrolytes restrict their practical applications.[49] Transition metal-based catalysts, composed of earth-abundant elements, offer lower costs than noble-metal-based catalysts and can achieve higher structural stability. These TM-based catalysts provide diverse structures with various coordination environments and oxidation states, allowing for tunable OER activities through doping.[5]

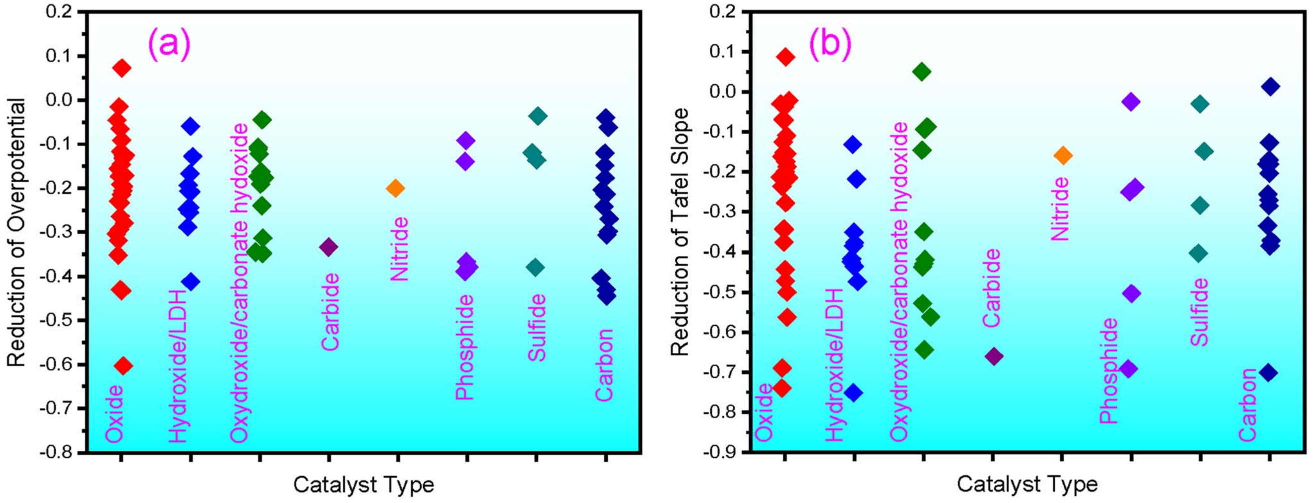

Fig. 3 Reduction of overpotential (a) and the Tafel slope (b) by F doping, as summarized from literature results.

Table 1 Summary of representative OER performance of transition-metal fluorides[a]

Catalyst	Overpotential at specific current density	Tafel slope (mV dec^{-1})	Tested durability	Electrolyte	Source
Binary fluorides					
Ni-Co-F-1,1	300 mV@10 mA cm^{-2}	77	10 h@15 mA cm^{-2*}	1 M KOH	50
CoF_2	285 mV@10 mA cm^{-2}	58	12 h@10 mA cm^{-2}	1 M KOH	9
Fe-doped CoF_2	230 mV@10 mA cm^{-2}	59	96 h@84 mA cm^{-2}	1 M KOH	18
CoF_2	300 mV@10 mA cm^{-2}	82	—	1 M KOH	
Ni-doped FeF_2	275 mV@10 mA cm^{-2}	47	25 h@10 mA cm^{-2*}	1 M KOH	51
Ni-doped Fe MOF	350 mV@10 mA cm^{-2*}	81	—	1 M KOH	
ZIF-FeCo-F-300	250 mV@10 mA cm^{-2}	51.2	20 h@10 mA cm^{-2*}	1 M KOH	52
ZIF-FeCo-MOF	360 mV@10 mA cm^{-2}	96.5	—	1 M KOH	
CoNi ZIF/CoFe-PBA-F-300	250 mV@10 mA cm^{-2}	47.4	14 h@12 mA cm^{-2*}	1 M KOH	53
CoNi ZIF/CoFe-PBA	320 mV@10 mA cm^{-2}	65.9	—	1 M KOH	
CoF_2/FeF_3	252 mV@10 mA cm^{-2}	52.1	10 h@10 mA cm^{-2*}	1 M KOH	54
Fe-CoF_2/NF	210 mV@10 mA cm^{-2}	32.2	53 h@10 mA cm^{-2*}	1 M KOH	55
Fe-Ni-F-350	277 mV@10 mA cm^{-2}	45	24 h@10 mA cm^{-2}	1 M KOH	56
Fe-Co-F-400	250 mV@10 mA cm^{-2}	38.3	10 h@10 mA cm^{-2*}	1 M KOH	57
$Co_{0.66}Fe_{0.33}F_2$	260 mV@10 mA cm^{-2}	54	50 h@10 and 50 mA cm^{-2}	1 M KOH	58
$Co_{0.67}Fe_{0.33}F_2$	270 mV@10 mA cm^{-2}	63.5	12 h@270 mV	1 M KOH	59
NiF5% ($NiF_2 \cdot 4H_2O$)	188 mV@10 mA cm^{-2}	44	100 h@46 mA cm^{-2}	1 M KOH	60
Ternary fluorides					
KNCF82 ($KNi_{0.8}Co_{0.2}F_3$)	310 mV@10 mA cm^{-2}	49	20 h@10 mA cm^{-2}	1 M KOH	17
KNFF2@NF ($KNi_{0.8}Fe_{0.2}F_3$)	258 mV@100 mA cm^{-2}	43.7	100 h@100 mA cm^{-2}	1 M KOH	16
$KCo_{0.80}Fe_{0.20}F_3$	254 mV@10 mA cm^{-2}	37.5	40 h@10 mA cm^{-2}	1 M KOH	19
ZIF-67@CoFe-PBA-F-250	243 mV@10 mA cm^{-2}	34	12 h@10 mA cm^{-2}	1 M KOH	61
$KCo_{0.5}Fe_{0.5}F_3$@NF	118 mV@10 mA cm^{-2}	19.63	130 h@10 mA cm^{-2}	1 M KOH	62
NFCF ($(NH_4)_3Fe_xCo_{1-x}F_6$)	243 mV@10 mA cm^{-2}	65.4	100 h@100 mA cm^{-2}	1 M KOH	63
$NaCo_{0.4}Fe_{0.3}Ni_{0.3}F_3$	265 mV@10 mA cm^{-2}	49	100 h@10 mA cm^{-2}	1 M KOH	64
High-entropy fluorides					
$K(MgMnFeCoNi)F_3$	369 mV@10 mA cm^{-2}	61	10 h@10 mA cm^{-2}	1 M KOH	65
$K_{0.8}Na_{0.2}(MgMnFeCoNi)F_3$	314 mV@10 mA cm^{-2}	55	10 h@10 mA cm^{-2}	1 M KOH	
$(CuNiFeCoZnMnMg)F_2$	292 mV@10 mA cm^{-2}	39	6 h@10 and 50 mA cm^{-2}	1 M KOH	66
$Al_{86}Ni_6Co_2Y_5Cu_{0.5}Fe_{0.5}$ HEF	261 mV@10 mA cm^{-2}	50	25 h@33 mA cm^{-2*}	1 M KOH	67
$Al_{86}Ni_6Co_2Y_5Cu_{0.5}Fe_{0.5}$ HEO	293 mV@10 mA cm^{-2}	88	—	1 M KOH	
$K(CoMnFeNiCr)F_3$	242 mV@10 mA cm^{-2}	114.57	24 h@10 mA cm^{-2}	1 M KOH	68

[a] (*) Estimated in this study.

Notably, some TM-based catalysts have even outperformed noble-metal-based catalysts.

TM fluoride catalysts have also been developed, and their performances are listed in Table 1 (data estimated in this study are indicated with an asterisk). These catalysts include binary, ternary, and high-entropy fluorides (HEFs) containing multiple elements.

3.1 Binary MF_2 and MF_3 fluorides

The binary fluorides discussed here are of MF_2 and MF_3 types, corresponding to divalent M^{2+} and trivalent M^{3+}, respectively. Here, M may represent one or more transition metals.

Binary fluorides such as CoF_2, FeF_2, MnF_2, NiF_2, and ZnF_2 possess a rutile structure.[69] The structure of CoF_2, shown in Fig. 4a, is a tetragonal structure with a space group of $P4_2/mnm$ and lattice constants of $a = 0.469$ nm and $c = 0.318$ nm. In the structure, highly distorted CoF_6 octahedra share edges along the c-axis. The trifluorides MF_3 (M = Fe, Co, Ru, Rh, Pd, and Ir) possess a rhombohedral structure with a space group of $R\bar{3}c$.[70] The binary fluorides have been reported in the following forms.

(a) Nanorods and nanowires. Nanorods or nanowires offer direct electron pathways along their lengths, which improves electron conductivity and reduces resistance. Their one-dimensional structure helps create more accessible active sites and enhances interaction with electrolytes. Transition-metal binary fluorides were first used for OER catalysts by the Feng group in 2018.[50] A simple one-step microwave method was used to synthesize materials with Ni/Co ratios of 1 : 1, 1 : 2, and 2 : 1, denoted as Ni-Co-F-1,1, Ni-Co-F-1,2, and Ni-Co-F-2,1, respectively. The synthesized one-dimensional (1D) nanorods are shown in the transmission electron microscope (TEM) images in Fig. 4b. The X-ray diffraction (XRD) patterns confirm the rutile-type single phase (Fig. 4c). In performance[71–74] it was found that the Ni-Co-F-1,1 catalyst with Co/Fe = 1/1 has the highest current density, even exceeding that of the benchmark catalyst IrO_2, as shown in the linear scan voltammetry (LSV) curve in Fig. 4d.[50] The overpotential of the Ni-Co-F-1,1 sample is 300 mV at a current density of 10 mA cm^{-2}, which is lower than that of all other samples, including IrO_2 (340 mV). The high catalytic activity may be due to the highest Co^{2+}/Co^{3+} ratio and the lowest Ni^{2+}/Ni^{3+} ratio. The Tafel plots are shown in Fig. 4e, where the Ni-Co-F-1,1 catalyst exhibits the lowest Tafel slope (77 mV dec^{-1}), consistent with the higher catalytic current density. This Ni-Co-F-1,1 catalyst outperforms the benchmark catalyst IrO_2.

Other 1D fluorides were also prepared. Feng and coworkers synthesized nanorod-shaped cobalt carbonate hydroxide hydrate as a precursor (Fig. 4f) on Ti foil through a hydrothermal route.[9] This precursor was converted to quasi-single-crystalline CoF_2 nanorods through fluorination by placing NH_4F in front of the precursor at 350 °C for 2 h under a nitrogen stream. Dong and colleagues synthesized Fe-doped $Co(OH)_2$ nanowires on nickel foam (NF), which were subsequently converted to Fe-doped CoF_2 by fluorination (Fig. 4g).[18] To reach 10 mA cm^{-2} current density, the overpotential of Fe-doped CoF_2 is only 230 mV, significantly lower than that of pristine CoF_2, which requires 300 mV (Fig. 4h). The Fe-doped CoF_2 shows a Tafel slope of 59 mV dec^{-1}, compared to 82 mV dec^{-1} of CoF_2. Fe-doping is thought to create defects and provide more active sites, improving the OER activity of CoF_2.

Ni-doped FeF_2 nanorods were synthesized by forming a Fe metal–organic framework (MOF), followed by fluorination using NH_4F (Fig. 4i).[51] The Ni doping reduced the overpotential of FeF_2 by approximately 63 mV (estimated in this study). It decreased the Tafel slope from 78 to 47 mV dec^{-1}.

(b) Irregular nanoparticles. Nanoparticles have high surface-to-volume ratios, providing abundant active sites for the OER. Fluorides with irregular shapes are also reported in the literature. Starting from preparing an FeCo-based zeolitic imidazolate framework (ZIF) by a simple coprecipitation method, the products were subsequently carbonized and fluorinated to obtain CoF_2 and FeF_2 nanoparticles (Fig. 4j).[52] The hybrid catalyst only needed 250 mV overpotential, compared to 360 mV of pristine ZIF-FeCo MOF, to reach 10 mA cm^{-2}. This clearly shows that fluorination significantly improves the OER.

(c) Nanoflakes and nanosheets. Nanoflakes and nanosheets maximize the exposure of active sites, offering a high density of accessible catalytic sites on broad and flat surfaces, facilitating ion transport along their planes. Two-dimensional (2D) porous Co–Fe nanoflakes were synthesized by a hydrothermal reaction, followed by low-temperature fluorination at 320 °C for 2 h.[54] The nanoflakes contain mixed CoF_2 and FeF_3, requiring only 252 mV overpotential at 10 mA cm^{-2}, with a low Tafel slope of 52.1 mV dec^{-1}. Recently, Fe–Ni–F nanosheets containing mixed NiF_2 and FeF_2 were synthesized by directly annealing metal acetate precursors with NH_4F in a tube furnace at 300–400 °C for 2 h (Fig. 4k).[56] The prepared Co–Fe–F nanosheets surpass the single-metal fluorides FeF_2 and NiF_2 and the benchmark RuO_2.

(d) Nanocubes and microcubes. Nanocubes and microcubes can expose specific crystal facets for the OER, with large surface areas and good structural stability. Porous Fe–Co–F nanocubes were prepared from a Fe–Co Prussian blue analogue (PBA).[57] First, Fe-Co-PBA nanocubes were formed by coprecipitation at room temperature (Fig. 4l, upper) and subsequently, the PBA nanocubes were fluorinated using NH_4F to form porous fluoride nanocubes (Fig. 4l, bottom). The synthesized materials contain a mixture of FeF_2, CoF_2, and ternary perovskite $K(CoFe)F_3$ (K is from a reactant $K_3FeC_6N_6$ used for coprecipitation). The overpotential is 250 mV at a current density of 10 mA cm^{-2}, with a low Tafel slope of 38.3 mV dec^{-1} and excellent catalytic stability for 10 h in long-term water electrolysis. With such a porous nanostructure, the electrochemical surface area is enhanced, resulting in increased exposure of the active sites and the construction of metal oxide layers over the catalyst surface. Another way to synthesize cubes is to use an MOF as a template, resulting in a larger size of about 3 μm.[58] Among a series of $Co_xFe_{1-x}F_2$, $Co_{0.66}Fe_{0.33}F_2$ shows the best performance (260 mV overpotential at 10 mA cm^{-2} and a 54 mV dec^{-1} Tafel slope) due to its large number of reactive sites and low charge transfer resistance.

(e) Nanospheres. Nanospheres maximize surface area relative to their volume, providing uniform active sites for the OER with good structural stability and resistance to aggregation.

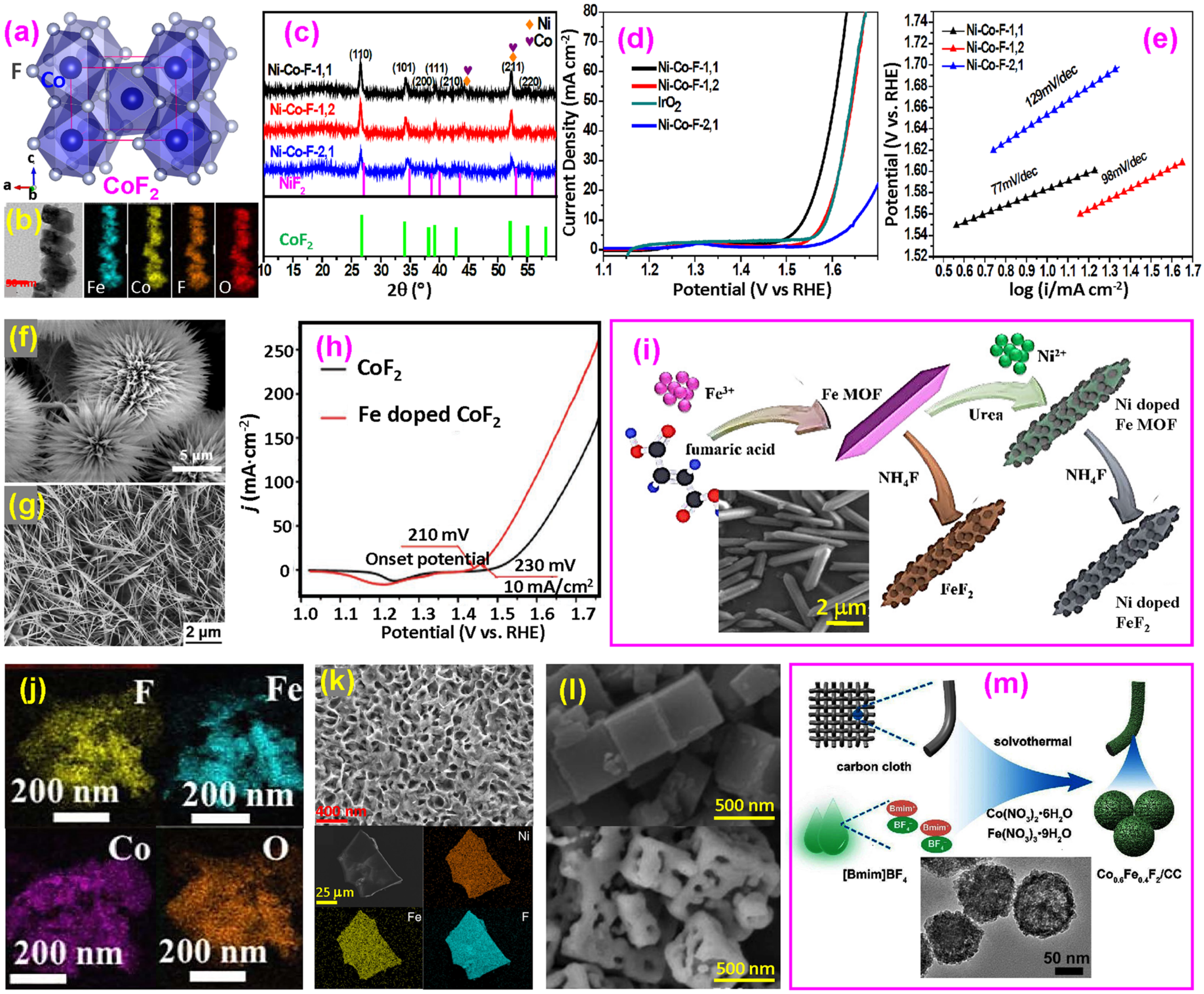

Fig. 4 Binary fluoride OER catalysts. (a) Structure of CoF_2; (b and c) TEM and XRD of Ni–Co–F; (d and e) LSV and Tafel plots of Ni–Co–F. Reproduced from ref. 50 with permission from the Royal Society of Chemistry, copyright 2018; (f) SEM image of cobalt carbonate hydroxide hydrate for producing CoF_2 nanorods. Reproduced from ref. 9 with permission from Elsevier, copyright 2020. (g) SEM image of Fe-doped CoF_2 nanowires and (h) LSV curves for CoF_2 and Fe-doped CoF_2. Reproduced from ref. 18 with open access. (i) Synthesis of Ni-doped FeF_2 nanorods, with an inset of the SEM image of Fe MOF. Reproduced from ref. 51 with permission from the Royal Society of Chemistry, copyright 2020. (j) TEM elemental maps of CoF_2 and FeF_2 irregular nanoparticles. Reproduced from ref. 52 with permission from Elsevier, copyright 2022. (k) SEM (upper) and TEM (bottom) images of Fe–Ni–F nanosheets. Reproduced from ref. 56 with permission from Elsevier, 2024. (l) SEM images of Fe-Co-PBA (upper) and Fe–Co–F (bottom) nanocubes. Reproduced from ref. 57 with permission from Elsevier, copyright 2019. (m) Synthesis of Co–Fe–F nanospheres with an inset of the TEM image. Reproduced from ref. 59 with permission from Elsevier, copyright 2022.

Using an ionic liquid-assisted solvothermal route, Co–Fe–F nanospheres were synthesized on the surface of carbon cloth (CC) fibers (Fig. 4m).[59] Among samples with varied Co/Fe ratios, $Co_{0.67}Fe_{0.33}F_2$ shows the best performance compared to $Co_{0.8}Fe_{0.2}F_2$ or CoF_2 due to F^- leaching and increased surface areas. This conclusion is consistent with that of the Co–Fe–F microcubes.[58]

3.2 Ternary and ternary-substituted fluorides

A large number of ternary and quaternary transition-metal fluorides have been reported, including common types such as $A_xB_yF_3$, $A_xB_yF_4$, $A_xB_yF_5$, $A_xB_yF_6$, $A_xB_yC_zF_6$, $A_xB_yC_zF_7$, and $A_xB_yC_zF_9$, where A represents NH_4, an alkali or an alkaline earth metal and B and C represent transition metals.[75–80] However, only a limited number of ternary fluorides, particularly those in the perovskite category, have been explored for OER applications.

Perovskites exhibit diverse structures, such as ABO_3-type single perovskite oxides, $AA'BB'O_6$-type double perovskite oxides, and $A_{n+1}B_nO_{3n+1}$-type layered perovskite oxides.[81–83] Perovskite-related TM-based catalysts have attracted significant interest from the scientific community for the OER due to their low cost, earth abundance, and excellent tunable electrochemical properties.[84–88] The following fluoride perovskites have been reported for the OER.

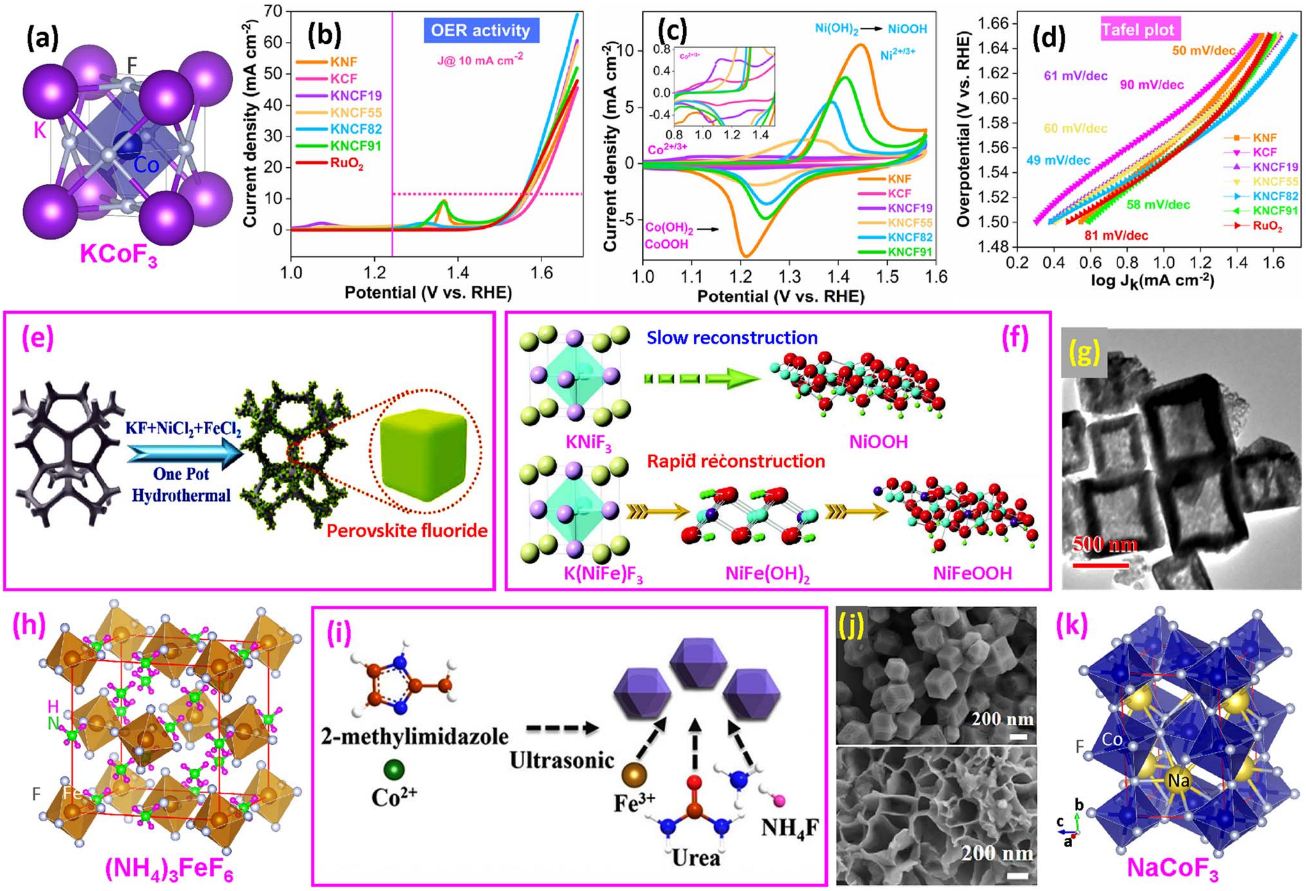

Fig. 5 Ternary fluoride OER catalysts. (a) Structure of ternary $KCoF_3$ perovskite; (b) LSV curves; (c) preoxidation peak ($Co^{2+/3+}$ and $Ni^{2+/3+}$); and (d) Tafel plots. Reproduced from ref. 17 with permission from American Chemical Society, copyright 2021. (e and f) Synthesis of $KNi_{1-x}Fe_xF_3$ on nickel foam and surface reconstruction during the OER. Reproduced from ref. 16 with open access; (g) TEM image of ZIF-67@CoFe-PBA nanoboxes. Reproduced from ref. 61 with permission from Elsevier, copyright 2021. (h) Structure of $(NH_4)_3FeF_6$. (i) Synthesis of $(NH_4)_3Fe_xCo_{1-x}F_6$ and (j) SEM images of ZIF-67 (upper) and NFCF (bottom). Reproduced from ref. 63 with permission from American Chemical Society, copyright 2022. (k) Structure of $NaCoF_3$.

(a) Simple perovskites. The representative ternary perovskite fluoride is ABF_3,[89,90] as shown in the structural model of $KCoF_3$ in Fig. 5a. Prakash *et al.* prepared this fluoride in nanoparticle form with varied Ni/Co ratios *via* a solvothermal method.[17] They found that when Ni/Co = 8/2, the $KNi_{0.8}Co_{0.2}F_3$ (KNCF82) catalyst shows an overpotential of 310 mV at 10 mA cm^{-2}, with a low Tafel slope of 49 mV dec^{-1}, outperforming the benchmark precious RuO_2 catalyst (Fig. 5b–d). Another study reports $K(CoFe)F_3$ nanoparticles synthesized by a hydrothermal method with varied Co/Fe ratios.[19] It was found that when Co/Fe = 0.8/0.2, the $KCo_{0.80}Fe_{0.20}F_3$ catalyst has the lowest overpotential of 254 mV@10 mA cm^{-2} and a Tafel slope value of 37.5 mV dec^{-1}. It is speculated that Co and the appropriate amount of Fe may produce a synergistic effect to enhance the OER performance.

Zhao and coworkers synthesized $KNi_{1-x}Fe_xF_3$ nanocubes with varying Ni/Fe ratios on nickel foam (NF) (Fig. 5e).[16] They found that Fe significantly promoted self-reconstruction and efficiently reduced the energy barriers of the OER. The $KNi_{0.8}Fe_{0.2}F_3$@NF electrocatalyst delivered an overpotential of 258 mV to afford 100 mA cm^{-2}, with excellent durability for 100 h. The Tafel slope was as low as 43.7 mV dec^{-1}. *In situ* Raman spectroscopy identified γ-NiOOH formation from $KNiF_3$@NF when the potential reaches 1.43 V, while for $K(NiFe)F_3$@NF, $Ni(OH)_2$ formed at 1.13 V and then γ-NiOOH at 1.43 V. The reconstruction mechanism is shown in Fig. 5f. The DFT calculations confirm that Fe incorporation alters the OER mechanism and reduces the energy barrier. It is believed that Fe doping below 25% is the optimum level.

Using ZIF-67 as a template, CoFe-PBA nanoboxes were obtained (Fig. 5g).[61] Subsequent fluorination etching produced $KCoF_3$ and $KFeF_3$ nanoparticles on the walls of the nanobox. Among the samples fluorinated between 150–350 °C for 2 h, the catalyst processed at 250 °C showed the best OER performance, with an overpotential of 243 mV to reach 10 mA cm^{-2}. Recently, $KCo_{1-x}Fe_xF_3$ nanoparticles on NF were synthesized by a hydrothermal method.[62] It was reported that $KCo_{0.5}Fe_{0.5}F_3$@NF requires only an overpotential of 118 mV to reach 10 mA cm^{-2}, with the Tafel slope as low as 19.63 mV dec^{-1}.

(b) Double perovskites and others. A study related to ternary perovskites involved $(NH_4)_3Fe_xCo_{1-x}F_6$ (NFCF),[63] which possesses a double-perovskite cubic structure (Fig. 5h). First, ZIF-67 was synthesized (Fig. 5i), and then $(NH_4)_3Fe_xCo_{1-x}F_6$ was synthesized by a solvothermal route (Fig. 5j).[63] It was found that the NFCF electrocatalyst required an overpotential of only 243 mV@10 mA cm^{-2}, which is approximately 27 mV lower than that of the commercial RuO_2. The Tafel slope value is 65.40 mV dec^{-1}, indicating rapid electrocatalytic kinetics with a high transfer coefficient. DFT calculations reveal that the Fe-doped NFCF electrocatalyst has a lower energy barrier from OOH* to O_2 than the non-doped fluoride, and the co-existence of Co and Fe in NFCF is beneficial for weakening the OH* adsorption energy during OER catalysis.

A recent study examined the B-site substitution of $NaCo_{1-2x}Fe_xNi_xF_3$ with three elements.[64] They optimized the Co/Fe/Ni ratio to be 4/3/3, which exhibited a low overpotential of 265 mV cm^{-2} at a current density of 10 mA and outstanding electrochemical stability after 100 h of continuous electrocatalysis. The dual substitution of Fe and Ni atoms was observed to produce higher-valence Co^{3+} ions and generate more active Fe^{3+} species. It should be noted that $NaCoF_3$ does not have a simple cubic structure like $KCoF_3$. Its structure is orthorhombic with a *Pnma* (no. 62) space group and lattice parameters of $a = 0.5603$ nm, $b = 0.7793$ nm, and $c = 0.5420$ nm (Fig. 5k).[91]

3.3 High-entropy fluorides

In some of the previously mentioned fluoride examples, a metal cation site is occupied by two elements. More elements can be added to form high-entropy (HE) materials, which are synthesized by mixing five or more elements in equal or nearly equal atomic ratios. HE materials are usually characterized by distinguished effects, including sluggish diffusion and cocktail effects to conventional materials.[92] HE materials have received significant attention in OER research;[92–94] however, studies on HE fluorides for the OER are still limited compared to other HE materials (Table 1).

In 2020, the Dai group proposed ABF_3-type high-entropy perovskite fluorides (HEPFs) as a new platform for the OER.[65] The synthesis process is shown in Fig. 6a. K and Na are selected to replace the A site, while seven metal ions (Mg^{2+}, Mn^{2+}, Fe^{2+}, Co^{2+}, Ni^{2+}, Cu^{2+}, and Zn^{2+}) are chosen to replace the B site in ABF_3. To achieve thorough mixing, the metal sulfates and acetates underwent ball milling to achieve full mixing of the metal source. Subsequently, the mixture was introduced into a boiling KF solution to produce rapid precipitation of HEPFs. It was found that when both A and B sites were replaced with $K_{0.8}Na_{0.2}(MgMnFeCoNi)F_3$, the catalyst showed the lowest overpotential and Tafel slope, which were lower than those of only the B site replaced by $K(MgMnFeCoNi)F_3$ (Fig. 6b).

Breitung and colleagues subsequently synthesized rutile-type HEFs with an AF_2 structure by a mechanochemical route.[66] Commercially available difluorides MnF_2, FeF_2, CoF_2, NiF_2, CuF_2, ZnF_2, and MgF_2 were mixed through a dry, long-term high-energy milling process conducted at 500 rpm for 48 h in a WC jar, and the samples were prepared in an Ar atmosphere. The configurational entropy values are expressed as

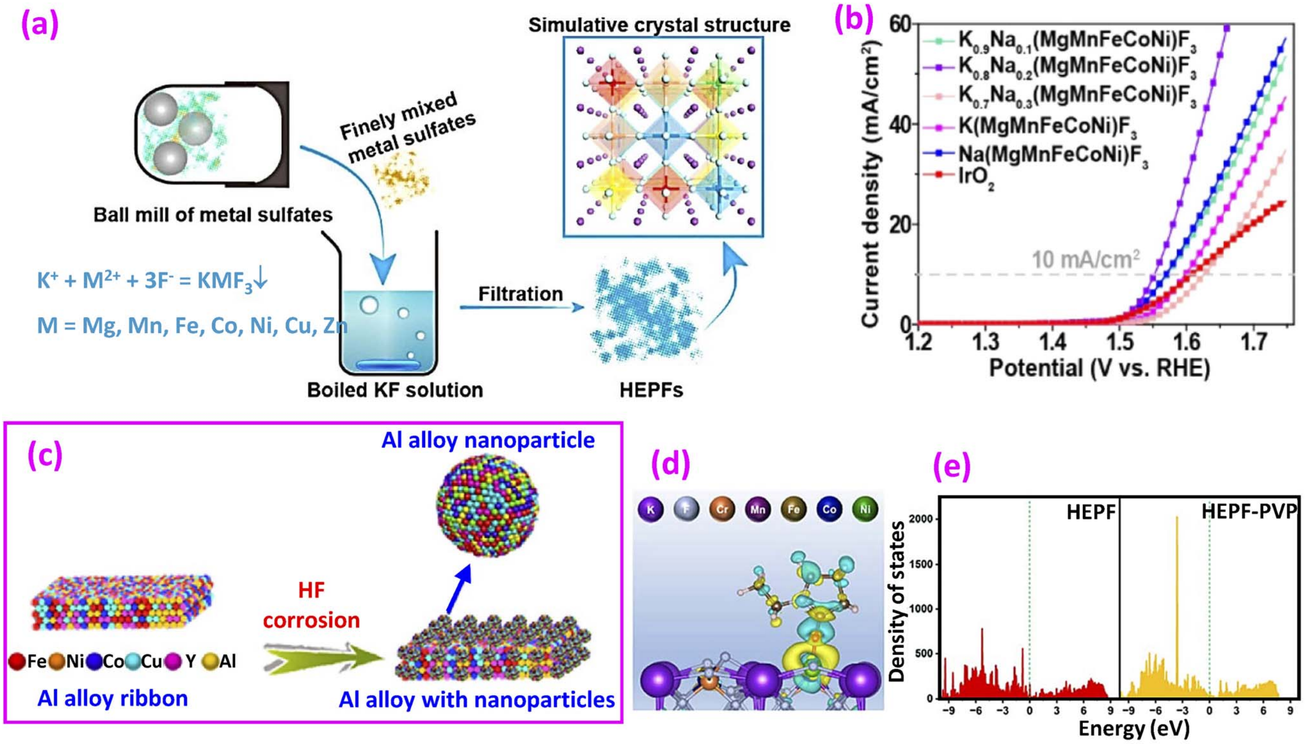

Fig. 6 (a) Synthesis of high-entropy ABF_3-type perovskite fluorides and (b) LSV curves. Reproduced from ref. 65 with permission from American Chemical Society, copyright 2020. (c) Synthesis of HE alloys from Al alloy ribbons. Reproduced from ref. 67 with permission Elsevier, copyright 2024. (d) Differential charge density of HEPF-PVP, where yellow and blue contours represent electron accumulation and depletion, respectively, and (e) DOS of HEPF and HEPF-PVP. Reproduced from ref. 68 with permission from the Royal Society of Chemistry, copyright 2023.

$$S_{\text{config}} = -R\left[\left(\sum_{i=1}^{N} x_i \ln x_i\right)_{\text{cation}} + \left(\sum_{j=1}^{M} x_j \ln x_j\right)_{\text{anion}}\right] \quad (21)$$

where x_i and x_j are the mole fraction of the elements i and j in cationic and anionic sites; R, the universal gas constant; N and M, the number of cationic and anionic species, respectively. The S_{config} values of compounds with 4, 5, 6, and 7 elements on the A site are calculated to be 1.39R, 1.61R, 1.79R and 1.95R, respectively. A compound with 7 elements (HEF7) on the A site shows superior activity with an overpotential of 292 mV at 10 mA cm^{-2}. The HEF enhances OER kinetics through the combined effects of well-distributed active sites, numerous fluorine locations, and channels facilitating diffusion. This improvement leads to reduced charge transfer resistance, lower polarization resistance values, and decreased Tafel slopes.[66]

Another approach to preparing HEF involves using HF corrosion of melt-spun HE Al alloy ribbons, as proposed recently (Fig. 6e).[67] First, a cast ingot of $Al_{86}Ni_6Co_2Y_5Cu_{0.5}Fe_{0.5}$ was prepared by arc melting of pure metals, followed by melt spinning to obtain rapidly cooled ribbons. After HF corrosion of the ribbons, surface oxidation yields HE oxide (HEO), while surface fluorination produces HEF. A comparative study showed that HEF has a reduced overpotential compared to HEO by 32 mV and a reduced Tafel slope by 38 mV dec^{-1}.

Although HEPFs possess entropy-dominated structural stability,[65] they are considered to have difficulties in restructuring because of their robust electron structure and the high bonding strength of the metal–fluorine bond.[68] Hao *et al.* proposed a strategy to enhance dynamic reconstruction by ligand modification using polyethylene pyrrolidone (PVP).[68] Several metal chlorides, nitrate, fluoride and PVP were mixed by a conventional solvothermal treatment at 180 °C for 6 h to produce HEPF. DFT calculations reveal that a PVP molecule enhances the charge concentration at the F site (Fig. 6c), which aids in lowering the bond energy required for reconstruction. The DOS shown in Fig. 6d demonstrates an electron-rich condition that promotes electron transfer. Among similar materials, PVP achieved a record-low overpotential of 242 mV at 10 mA cm^{-2}. However, its Tafel slope of 114.57 mV dec^{-1} remains higher compared to other catalysts.

4. Fluoride-oxide catalysts

It is known that pure fluorides exhibit poor electroconductibility due to the high ionicity of metal–F bonds, which hinders their catalytic activity. However, the intrinsically low conductivity of metal fluorides can be improved by introducing metal–O bonds.[95] Metal fluoride-oxide phases demonstrate higher electroconductivity and electrochemical robustness due to the coexistence of metal–O and metal–F bonds.[20,96,97] This fluoride-oxide system has garnered significant attention as a potential class of OER catalysts. It may be categorized as oxyfluoride, various fluorinated oxides, and fluoride/oxide heterocatalysts. The term "oxyfluoride", also referred to as "fluoride oxide" or "oxide fluoride" in the literature, denotes a compound containing both O and F, with either defined or undefined stoichiometry. "Fluorinated oxide," on the other hand, refers to an oxide that has undergone fluorination. The term "fluoroxide" is seldom used in the OER research community. Although these terms may overlap in definition, we follow the classification from relevant literature sources.

4.1 Oxyfluorides

Oxyfluoride compounds contain both O and F atoms, as shown in Table 2. Yang and colleagues fabricated a NiFe oxyfluoride (NiFeOF) holey film, as depicted in Fig. 7a, by electrochemical deposition of a 2 μm NiFe thin film onto a stainless-steel substrate.[98] This was followed by substrate removal and

Table 2 Summary of representative OER performance of oxyfluorides[a]

Catalyst	Overpotential at specific current density	Tafel slope (mV dec^{-1})	Tested durability	Electrolyte	Source
$Ni_{0.85}Fe_{0.15}OF$	295 mV@10 mA cm^{-2}	38	2.78 h@10 mA cm^{-2}	1 M KOH	98
$TaO_2F/^gC$	360 mV@10 mA cm^{-2}	75	120 h@10 mA cm^{-2}	1 M KOH	99
Ta_2O_5/CC	530 mV@10 mA cm^{-2}	112	—	1 M KOH	
NiCoFO	350 mV@10 mA cm^{-2}	23	10 h@1.58 V	1 M KOH	95
Ni-11.8 at% Fe	260 mV@10 mA cm^{-2}	53	24 h@50 mA cm^{-2}	1 M KOH	100
$NiFe_2F_{4.4}O_{1.8}$	270 mV@10 mA cm^{-2}	46	270 h@10 mA cm^{-2}	1 M KOH	10
$MnFeF_5(H_2O)_2$	492 mV@10 mA cm^{-2}	156	>5 h@10 mA cm^{-2}	0.5 M H_2SO_4	101
$MnFe_2F_8(H_2O)_2$	480 mV@10 mA cm^{-2}	153	13 h@10 mA cm^{-2}	0.5 M H_2SO_4	
$MnFeF_{4.6}O_{0.2}$	500 mV@10 mA cm^{-2}	195	11 h@10 mA cm^{-2}	0.5 M H_2SO_4	
$MnFe_2F_{5.8}O_{1.1}$	515 mV@10 mA cm^{-2}	175	20 h@10 mA cm^{-2}	0.5 M H_2SO_4	
$Co_{0.5}Fe_{0.5}O_{0.5}F_{1.5}$	220 mV@10 mA cm^{-2}	27	648 h@10–1000 mA cm^{-2}	1 M KOH	102
$Pb_3Fe_2O_5F_2$	640 mV@1 mA cm^{-2*}	—	3 h@1.7 V	0.1 M K_3PO_4	103
FeVNbTiZrOF-CC-40	348 mV@10 mA cm^{-2}	110.3	48 h@10 mA cm^{-2}	1 M KOH	104
CoFeOF/NF	236 mV@10 mA cm^{-2}	46.35	24 h@10 mA cm^{-2}	1 M KOH	105
CoOF/NF	320 mV@10 mA cm^{-2}	64.21	24 h@10 mA cm^{-2}	1 M KOH	
FeOF/NF	290 mV@10 mA cm^{-2}	58.72	24 h@10 mA cm^{-2}	1 M KOH	
NCoFO/CC-60	230 mV@10 mA cm^{-2}	62	150 h@10 mA cm^{-2}	1 M KOH	106
FeFFIVE-1-Ni	286 mV@10 mA cm^{-2}	86	30 h@1.6 V (71% retention)	1 M KOH	107
$Co_{0.25}Ni_{0.25}Fe_{0.5}O_{0.5}F_{1.5}$	290 mV@10 mA cm^{-2}	—	—	1 M KOH	108

[a] (*) Estimated in this study.

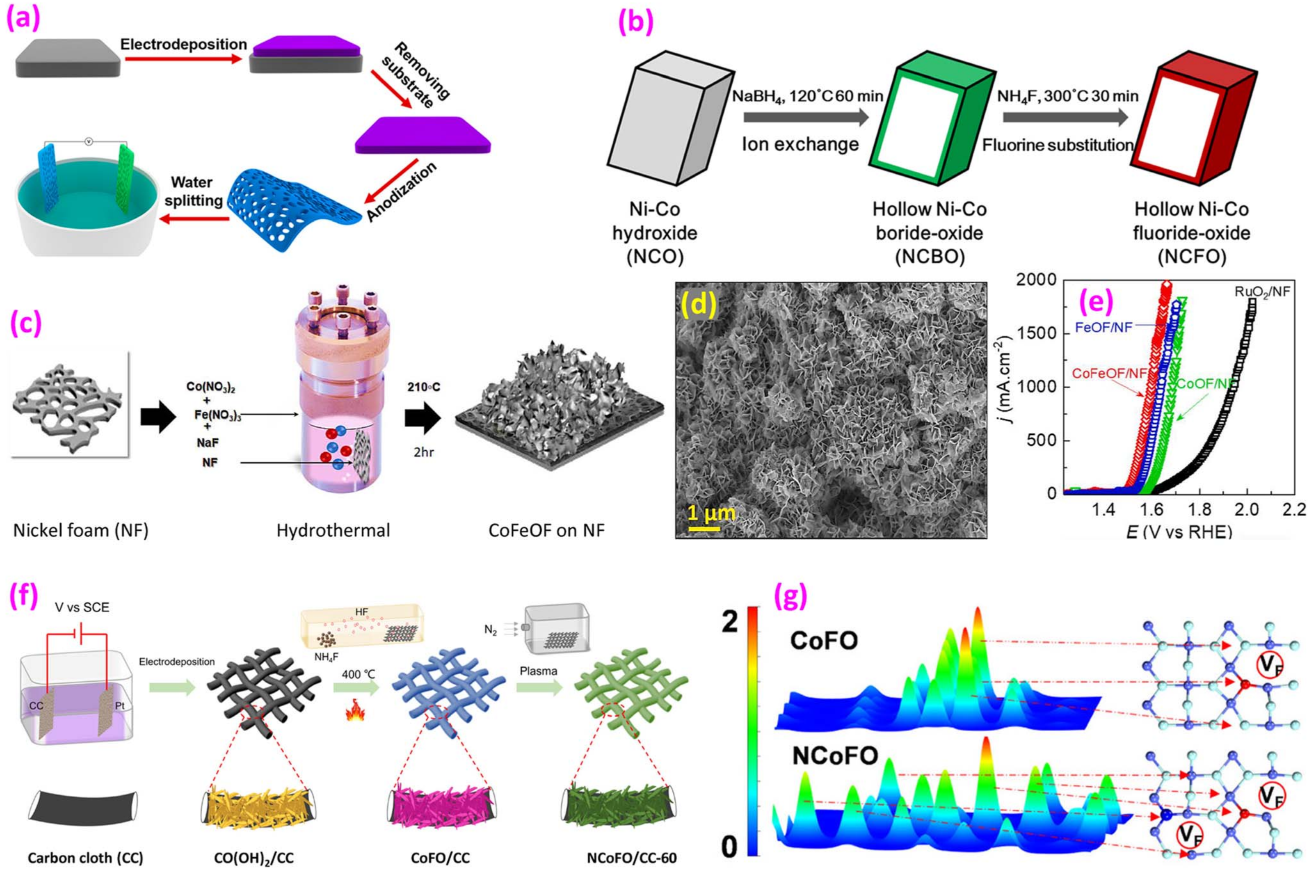

Fig. 7 Oxyfluoride catalysts. (a) Fabrication of a NiTiOF holy film. Reproduced from ref. 98 with permission from American Chemical Society, copyright 2017. (b) Synthesis process from NCO through NCBO to NCFO. Reproduced from ref. 95 with permission from American Chemical Society, copyright 2019. (c) Synthesis of a CoFeOF film; (d) SEM image of CoFeOF nanosheets and (e) LSV polarization curves. Reproduced from ref. 105 with permission from Elsevier, copyright 2024. (f) Synthesis of NiCoFO@CC and (g) electron density difference calculated using DFT. Reproduced from ref. 106 with open access.

anodization of the free-standing thin film to obtain a porous amorphous NiFeOF structure with an interconnected crystalline NiFe alloy framework. The Ni-15 at% Fe catalyst requires only 295 mV overpotential to reach 10 mA cm^{-2}. DFT analysis verified that the nickel atom situated on the oxide surface functions as the primary site for the OER. Among the materials studied, NiFeOF demonstrated the most favorable energetics for facilitating the OER process. Yamada *et al.* electrodeposited both Ni and Fe onto a piece of pure Ni plate, followed by anodization to form a nanoporous fluoride-rich Fe-doped Ni oxyfluoride layer, which was then converted into an amorphous or poorly crystalline Fe-doped Ni hydroxide film.[100]

Kornienko and coworkers synthesized hydrated NiFe fluorides, $NiFe_2F_8(H_2O)_2$ and $CoFe_2F_8(H_2O)_2$, *via* a simple microwave-assisted solvothermal synthesis.[10] Subsequent calcination produced amorphous oxyfluorides $NiFe_2F_{4.4}O_{1.8}$ and $CoFe_2F_{6.6}O_{0.7}$, respectively, with the former catalyst showing superior performance. The same group also prepared Mn–Fe-based fluorinated materials that converted to oxyfluorides after heating in the air.[101] The amorphous oxyfluorides were evaluated in H_2SO_4 acidic media, demonstrating high performance. A stable compound, TaO_2F, supported on graphitized carbon (^gC), was synthesized using a simple ion-adsorbed method.[99] This catalyst exhibited an overpotential of 170 mV lower than that of an unfluorinated Ta_2O_5/CC catalyst at 10 mA cm^{-2}. A recent study by the same group on the $Co_{0.5}Fe_{0.5}O_{0.5}F_{1.5}$ oxyfluoride catalyst demonstrated superior performance compared to most known Co-based catalysts.[102]

Han *et al.* synthesized a nickel–cobalt fluoride oxide (NCFO) hollow nanoprism through three steps: Ni–Co hydroxide formation, followed by ion exchange, and finally fluorination (Fig. 7b).[95] The synthesized catalyst exhibited 350 mV overpotential at 10 mA cm^{-2} with an exceptionally low Tafel slope of 23 mV dec^{-1}.

Pan *et al.* dealloyed a melt-spun Zr-based amorphous ribbons in HF and H_2O_2 corrosive media.[104] After *in situ* chronopotentiometric surface reconstruction, a core–shell structure was obtained. The catalyst showed only 4.6% loss after the 48-h test, compared to RuO_2, which had a 43.2% loss. The unique core–shell configuration facilitates improved ion movement and material transport while increasing the number of active sites at the interface between the electrolyte and electrode, thereby enhancing OER performance. DFT calculations suggest that the presence of F contributes to a higher concentration of surface-active sites characterized by an unsaturated electronic configuration. Maeda *et al.* synthesized 2D perovskite oxyfluoride $Pb_3Fe_2O_5F_2$, which features two layers of perovskite blocks

Table 3 Summary of representative OER performance of fluorinated oxides[a]

Catalyst	Overpotential at specific current density	Tafel slope (mV dec^{-1})	Tested durability	Electrolyte	Source
Fluorinated MO					
F–CoO/CC	237.7 mV@10 mA cm^{-2}	68	60 h@10 mA cm^{-2}	1 M KOH	113
CoO/CC	349 mV@10 mA cm^{-2}	89	—	1 M KOH	
Fe, F–NiO	215 mV@10 mA cm^{-2}	67.5	100 h@10 mA cm^{-2}	1 M KOH	114
Fe–NiO	230 mV@10 mA cm^{-2}	79.5	—	1 M KOH	
F–NiO	266 mV@10 mA cm^{-2}	136.3	—	1 M KOH	
NiO	270 mV@10 mA cm^{-2}	146.4	—	1 M KOH	
Fluorinated MO$_2$					
$(Ir_{0.30}Sn_{0.35}Nb_{0.35})O_2$:10F	290 mV@10 mA cm^{-2*}	77	22.2 h@1.65 V	1 N H_2SO_4	115
$(Ir_{0.30}Sn_{0.35}Nb_{0.35})O_2$	350 mV@10 mA cm^{-2*}	98	22.2 h@1.65 V	1 N H_2SO_4	
$(Mn_{0.7}Ir_{0.3})O_2$:10F	210 mV@10 mA cm^{-2*}	65	24 h@1.45 V	1 N H_2SO_4	116
$(Mn_{0.7}Ir_{0.3})O_2$	220 mV@10 mA cm^{-2*}	67	—		
$(Mn_{0.8}Ir_{0.2})O_2$:10F	200 mV@10 mA cm^{-2}	38	24 h@1.45 V	1 N H_2SO_4	117
$(Mn_{0.8}Ir_{0.2})O_2$	240 mV@10 mA cm^{-2}	46	24 h@1.45 V		
$(Mn_{0.8}Nb_{0.2})O_2$:10F	680 mV@10 mA cm^{-2}	371.17	24 h@1.9 V	1 N H_2SO_4	118
$(Mn_{0.8}Nb_{0.2})O_2$	770 mV@10 mA cm^{-2}	385.36	24 h@1.9 V		
IrO_x/F–TiO_2	272 mV@10 mA cm^{-2}	53.1	10 h@1.55 V	0.5 M H_2SO_4	119
IrO_x/TiO_2	322 mV@10 mA cm^{-2}	63.3	10 h@1.55 V	0.5 M H_2SO_4	
RuO_x/F–TiO_2	252 mV@10 mA cm^{-2}	50.3	10 h@10 mA cm^{-2}	0.5 M H_2SO_4	120
RuO_x/TiO_2	295 mV@10 mA cm^{-2}	62.8	10 h@10 mA cm^{-2}		
PbO_2–F–Fe–Co	307 mV@10 mA cm^{-2}	188	156 h@2.5 mA cm^{-2*}	0.5 M/1 M H_2SO_4	121
F-TMO	330 mV@50 mA cm^{-2}	30	336 h@500 mA cm^{-2}	1 M KOH	122
TMO	380 mV@50 mA cm^{-2}	60	—		
Fluorinated ABO$_4$					
F–$NiMoO_4$	188 mV@50 mA cm^{-2}	33.8	85 h@50 mA cm^{-2}	1 M KOH	41
$NiMoO_4$	290 mV@50 mA cm^{-2}	130.0			
F–$CoMoO_{4-x}$-2@GF	256 mV@10 mA cm^{-2}	64.4	20 h@1.54 V	Alkaline solution	123
$CoMoO_{4-x}$@GF	368 mV@10 mA cm^{-2}	81.8			
Fluorinated A$_2$B$_2$O$_7$					
YRuO-PVDF2	235 mV@10 mA cm^{-2}	41	10 h@10 mA cm^{-2}	0.5 M H_2SO_4	124
YRuO	296 mV@10 mA cm^{-2}	46	10 h@10 mA cm^{-2}		
Fluorinated spinel oxides					
F–Co_3O_4/NF	370 mV@50 mA cm^{-2}	70	—	1 M KOH	13
Co_3O_4/NF	460 mV@50 mA cm^{-2}	160	—		
$Co_3O_{3.87}F_{0.13}$	430 mV@10 mA cm^{-2}	56	—	0.1 M KOH	125
$Co_3O_{3.87}\square_{0.13}$	440 mV@10 mA cm^{-2}	56	—		
Co_3O_4	520 mV@2.6 mA cm^{-2}	64	—		
$F_{0.2}$-V-Co_3O_4-350	323 mV@10 mA cm^{-2}	75.9	—	1 M KOH	126
$ZnCo_2O_{4-x}F_x$/CNTs	440 mV@50 mA cm^{-2}	59.2	13 h@10 mA cm^{-2}	1 M KOH	127
$ZnCo_2O_{4-x}$/CNTs	560 mV@50 mA cm^{-2*}	106.3	2 h@10 mA cm^{-2*}		
$ZnCo_2O_4$-F	472 mV@10 mA cm^{-2}	65.1	30 h@1.65 V	1 M KOH	128
$ZnCo_2O_4$	440 mV@10 mA cm^{-2}	59.9	30 h@1.65 V		
F–Co/$CoFe_2O_4$@NC	280 mV@10 mA cm^{-2}	49.7	50 h@1.51 V	1 M KOH	129
Co/$CoFe_2O_4$@NC	320 mV@10 mA cm^{-2}	58.0	—		
F–$MnCo_2O_4$	210 mV@10 mA cm^{-2}	69.5	100 h@10 mA cm^{-2}	0.1 M $HClO_4$	130
$MnCo_2O_4$	370 mV@10 mA cm^{-2}	131.6			
Fluorinated perovskite oxides					
$SrCoO_{2.85-d}F_{0.15}$	380 mV@10 mA cm^{-2}	60	20 h@1.60 V	1 M KOH	14
$SrCoO_{3-d}$	434 mV@10 mA cm^{-2}	71	—		
F-$Ba_{0.5}Sr_{0.5}Co_{0.8}Fe_{0.2}O_{3-\delta}$	280 mV@10 mA cm^{-2}	102.65	100 h@15 mA cm^{-2*}	1 M KOH	131
$Ba_{0.5}Sr_{0.5}Co_{0.8}Fe_{0.2}O_{3-\delta}$	342 mV@10 mA cm^{-2}	119.73	<20 h@5 mA cm^{-2*}		
$(Ba_{0.5}Sr_{0.5}Co_{0.8}Fe_{0.2}O_{3-d})_{3/4}[KM(\text{II})F_3]_{1/4}$	345 mV@10 mA cm^{-2}	—	20 h@10 mA cm^{-2}	1 M KOH	132
$Ba_{0.5}Sr_{0.5}Co_{0.8}Fe_{0.2}O_{3-d}$	450 mV@10 mA cm^{-2}	—	20 h@10 mA cm^{-2}		
$F_{0.2}$–$LaCoO_3$	390 mV@10 mA cm^{-2}	114.1	120 h@2 mA cm^{-2} (ZAB)	1 M KOH	133
$LaCoO_3$	530 mV@10 mA cm^{-2}	182.8	70 h@2 mA cm^{-2} (ZAB)		
$BaFe_{0.8}Co_{0.2}O_2F$	400 mV@10 mA cm^{-2}	52.8	—	1 M KOH	134
$BaFe_{0.8}Co_{0.2}O_3$	440 mV@10 mA cm^{-2}	80.3	—		

Table 3 (*Contd.*)

Catalyst	Overpotential at specific current density	Tafel slope (mV dec^{-1})	Tested durability	Electrolyte	Source
F–$NiTiO_3$/C	270 mV@10 mA cm^{-2}	81.2	18 h@28 mA cm^{-2}	1 M KOH	21
$NiTiO_3$/C	680 mV@10 mA cm^{-2}	112.4	18 h@18 mA cm^{-2}		
F-$La_{0.6}Sr_{0.4}Co_{0.2}Fe_{0.8}O_{3-d}$	350 mV@10 mA cm^{-2*}	100	—	0.1 M KOH	135
$La_{0.6}Sr_{0.4}Co_{0.2}Fe_{0.8}O_{3-d}$	400 mV@10 mA cm^{-2*}	123*	—		
LSNF-OF	308.1 mV@10 mA cm^{-2}	61.13	5 h@10 mA cm^{-2}	1 M KOH	136
LSNF	381.2 mV@10 mA cm^{-2}	62.47	—		
LSNF-MF	486.4 mV@10 mA cm^{-2}	67.99	5 h@10 mA cm^{-2}		
Fluorinated mixed oxides					
FeCo-OF	285 mV@10 mA cm^{-2}	95.7	12 h@10 mA cm^{-2}	1 M KOH	44
FeCo–O	370 mV@10 mA cm^{-2}	145.9	12 h@10 mA cm^{-2}	1 M KOH	
Fe–OF	570 mV@10 mA cm^{-2}	174.6	—	1 M KOH	
Fe–O	1000 mV@10 mA cm^{-2}	562.5	—	1 M KOH	
Co–OF	330 mV@10 mA cm^{-2}	156.8	—	1 M KOH	
Co–O	467 mV@10 mA cm^{-2}	168.6	—	1 M KOH	

[a] (*)Estimated in this study.

interleaved with a PbF block layer.[103] This 2D catalyst exhibits nearly eight times the activity of its three-dimensional (3D) bulk counterpart, $PbFeO_2F$, in the oxygen evolution reaction. A recent study evaluated the ABX_2Y type oxynitride, oxyfluoride, and nitrofluoride perovskites for solar water splitting.[109] Four catalysts ($BaInO_2F$, $InSnO_2N$, $CsPbO_2F$, and $LaNbN_2O$) were identified as potential photocatalysts, with $BaInO_2F$ oxyfluoride showing the lowest calculated overpotential.

Recently, CoFeOF nanosheets on NF were prepared using metal nitrates and NaF (as an F source) through a hydrothermal route, followed by calcination at 210 °C for 2 h (Fig. 7c).[105] Nanosheets, 8–10 nm thick, were grown vertically on NF (Fig. 7d). CoFeOF/NF demonstrated superior functionality compared to FeOOF/NF or CoOF/NF (Fig. 7e), performing effectively even in seawater. Another approach involved electrodepositing $Co(OH)_2$ on CC, followed by fluorination at 400 °C using NH_4F as the F source and subsequent N_2 plasma treatment (Fig. 7f).[106] Among the tested materials, N-doped CoFO/CC demonstrated superior performance in both the OER and HER compared to CoFO/CC and Co_3O_4/CC. Computational studies using DFT revealed that the CoF bond in N-doped CoFO is elongated relative to pure CoF_2 and CoFO, attributed to the lower electronegativity of N in comparison to F. In the case of CoFO, electron localization occurs on F atoms adjacent to O, whereas in N-doped CoFO, electrons from F tend to shift towards N and Co atoms (Fig. 7g). N-doping also created more F vacancies, significantly optimizing the electronic structure. FeOF with NiF_2 nanosheets was also reported *via* a solvothermal reaction using pyrazine, followed by calcination in air. This calcination introduces O into the catalyst lattice. DFT simulations revealed that O incorporation led to an increased concentration of electronic states near the Fermi level, suggesting improved electron conductivity. Additionally, the energy barrier for the rate-limiting step in *OOH formation decreased from 2.26 eV to 2.02 eV, resulting in enhanced OER performance.

4.2 Fluorinated oxides

Metal oxides, including both precious metal oxides and non-precious metal oxides (primarily transition-metal oxides), have been widely used as catalysts for the OER.[5,49,110–112] Among these, earth-abundant transition-metal oxides have garnered significant attention for the OER due to their high activity, enhanced stability, and low cost.[49] The fluorination of these metal oxides has been reported and is summarized in Table 3. The following fluorinated oxides have been studied for the OER.

(1) Fluorinated MO. In the MO oxide, the metal M is divalent. Pure cobalt monoxide (CoO) exhibits HER activity due to its low electron conductivity ($\sim 1 \times 10^{12}$ Ω·m).[113] However, after doping CoO nanowires with aliovalent F^- anions, superior HER and OER activities are observed. The F ions increase the charge on the Co site, weakening H* adsorption and also narrowing the band gap, improving electron conductivity. As illustrated in Fig. 8a, Fe-doped Fe–$Ni(OH)_2$ hollow flower-spheres are synthesized *via* a solvothermal method, which is then converted to a Fe-doped NiO cubic structure through calcination and finally to Fe and F-codoped NiO by fluorination.[114] Comparison of the OER activities of different catalysts shows that F doping significantly reduces overpotentials (Fig. 8b) and Tafel slopes (Table 3). DFT calculations reveal that the RDS energy barrier is reduced from 2.23 eV (NiO) to 1.92 eV (Fe–NiO) and 1.87 eV (Fe, F–NiO), while the band gap decreases from 2.27 eV (NiO) to 2.09 eV (Fe, F–NiO).

(2) Fluorinated MO_2. F has been used to dope MO_2 compounds such as (Ir, Sn, Nb)O_2,[115] TiO_2,[119,120,137] (Mn, Ir) O_2,[116,117] (Mn, Nb)O_2,[118] and PbO_2.[121] Given the reputation of IrO_2 as a highly effective catalyst, researchers have explored alloying Ir with alternative metals to decrease the overall cost of the catalyst.[115] With the additions of Sn and Nb, although $Ir_{0.25}Sn_{0.375}Nb_{0.375}O_2$ shows reduced activities, F doping at a level of 10 wt% significantly improves its performance, even surpassing that of IrO_2. With the addition of Mn, either $Mn_{0.7}Ir_{0.3}O_2$ or

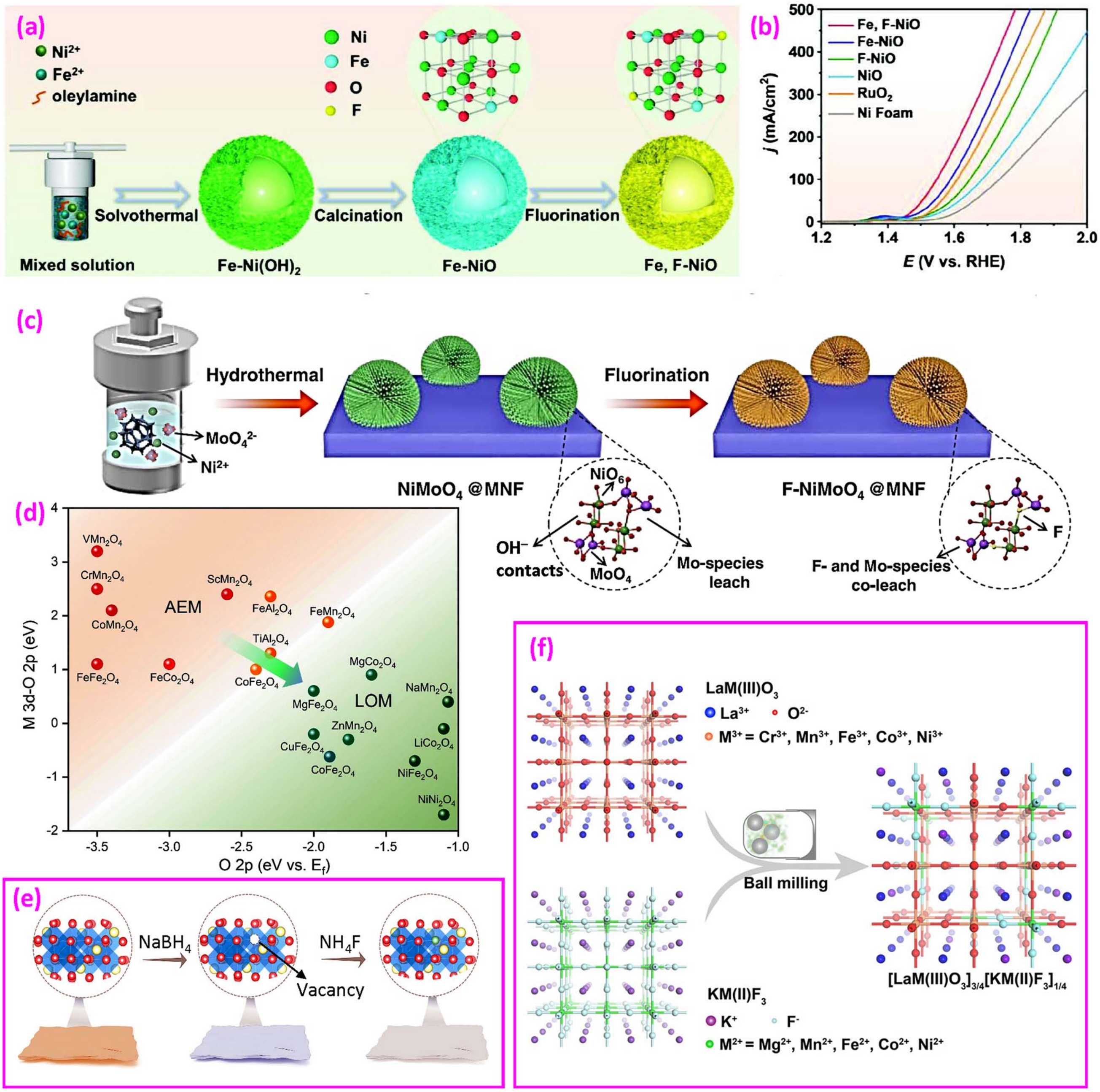

Fig. 8 Fluorinated oxides for the OER. (a) Synthesis of Fe and F co-doped NiO hollow flower-spheres and (b) LSV polarization curves. Reproduced from ref. 114 with permission from John Wiley and Sons, copyright 2023. (c) Synthesis of F-doped $NiMoO_4$ on MoNi foam. Reproduced from ref. 41 with permission from American Chemical Society, copyright 2021. (d) Relationship between AEM/LOM and relative band centers and (e) synthesis of $ZnCo_2O_{4-x}$ and $ZnCo_2O_{4-x}F_x$. Reproduced from ref. 127 with permission from John Wiley and Sons, copyright 2023. (f) Synthesis of a perovskite oxide-fluoride solid solution. Reproduced from ref. 132 with permission from John Wiley and Sons, copyright 2021.

$Mn_{0.8}Ir_{0.2}O_2$ outperforms IrO_2, while F doping further enhances their OER performance.[116,117] DFT calculations show that the d-band center of the F-doped material is close to that of pure IrO_2, suggesting an improvement in overall catalytic activity.[116]

To stabilize the MnO_2 surface for the OER in acidic environments, transition metals are added. The Kumta group demonstrated that adding 20% Nb reduces the overpotential (at 10 mA cm^{-2}) in H_2SO_4 acid from 900 to 770 mV, and further incorporation of F reduces it to 680 mV.[118]

Fluorinated TiO_2 has been used to enhance the development of OER catalysts. IrO_x on F–TiO_2 exhibits significantly improved OER activities over IrO_x on undoped TiO_2 in an acidic solution, likely due to the higher electron conductivity of fluorinated TiO_2, improved dispersion, and suppression of Ir dissolution.[119] The same group also developed RuO_x on a F–TiO_2 support, which outperforms RuO_x on undoped TiO_2.[120] DFT calculations suggest that F ions facilitate proton transfer, accelerating the O–O coupling steps.[138]

(3) Fluorinated ABO_4. Chai *et al.* synthesized $NiMoO_4$ nanorods on nanospheres on MoNi foam (MNF) using a hydrothermal method, followed by fluorination, as shown in Fig. 8c.[41] The F-doped materials showed superior OER performance, as detailed in Table 3. F–$NiMoO_4$ is amorphous, and the strong ionicity of the metal–F bonds suggests that F species in the amorphous layer can migrate and leach into the alkaline electrolyte, facilitating the adsorption of reaction intermediates.

F has also been doped into layered oxides. $CoMoO_4$ nanosheets were synthesized on graphite felt (GF) and fluorinated using NH_4F at 400 °C.[123] F-doped $CoMoO_4$ demonstrated a 112 mV lower overpotential and 17.4 mV dec^{-1} lower Tafel slope compared to its non-fluorinated counterpart. The F-doped $CoMoO_4$ outperforms RuO_2@GF, whose overpotential is 284 mV@10 mA cm^{-2} and Tafel slope is 76.6 mV dec^{-1}. The F-doped material is enriched in O vacancies and has an optimized electronic configuration of active sites for the OER.

(4) Fluorinated $A_2B_2O_7$. The pyrochlore oxide $A_2B_2O_7$ exhibits high chemical and structural stability during the OER.[139] A sol–gel method was used to synthesize $Y_2Ru_2O_{7-d}$ nanoparticles, followed by calcination with polyvinylidene fluoride (PVDF) powders.[124] OER testing in 0.5 M H_2SO_4 showed that both the overpotential and Tafel slope were reduced by fluorination (Table 3). F doping introduces O vacancies, promoting OER kinetics. DFT calculations support the LOM of the OER.

(5) Fluorinated spinel oxides. Liu *et al.* analyzed the electronic structure of several spinel oxides and proposed their possible AEM or LOM for the OER, as shown in Fig. 8d.[127] They synthesized F-doped $ZnCo_2O_{4-x}F_x$ nanosheets *via* a two-step route, as illustrated in Fig. 8e. First, oxygen vacancies (V_O) in $ZnCo_2O_4$ (denoted as $ZnCo_2O_{4-x}$) are created by $NaBH_4$ reduction, followed by fluorination using NH_4F to form $ZnCo_2O_{4-x}F_x$. The fluorinated catalyst reduces the overpotential at 50 mA cm^{-2} from 570 mV (estimated in this study) to 440 mV (a 22.8% reduction) and the Tafel slope from 106.3 to 59.2 mV dec^{-1} (a 44.3% reduction). This approach fills lattice O vacancies on the surface with F ions, strengthening the hybridization of Co 3d and O 2p for the LOM. However, a study showing opposite results was also reported, where F doping had a slight negative impact, raising the overpotential from 440 to 472 mV at 10 mA cm^{-2} (a 7% increase) and the Tafel slope from 59.9 to 65.1 mV dec^{-1} (an 8.7% increase).[128]

The oxide Co_3O_4 also possesses a spinel structure. DFT calculations indicate that the F-doped Co_3O_4 (100) surface is active for the OER.[140] Mesoporous $Co_3O_{3.87}\square_{0.13}$ ($\square$ represents V_O) reduces the overpotential of Co_3O_4 from 520 mV to 440 mV at 10 mA cm^{-2}, while F-doped $Co_3O_{3.87}F_{0.13}$ further reduces it to 430 mV.[125]

(6) Fluorinated perovskite oxides. Perovskite oxides have been widely studied as catalysts for the OER, and fluorination of these oxides has drawn significant attention.[14,21,131–136,141] The perovskite oxide $Ba_{0.5}Sr_{0.5}Co_{0.8}Fe_{0.2}O_{3-\delta}$ (BSCF) is considered one of the most effective OER catalysts.[142–145] Xiong *et al.* synthesized F-doped F-BSCF for the OER.[131] As O^{2-} is partially replaced by F^-, this doping reduces the Co(III) and Fe(III) species to lower oxidation states, activating surface O to highly oxidative O^{2-}/O^- for the OER. F-BSCF reduces the overpotential of BSCF from 342 to 280 mV at 10 mA cm^{-2} and the Tafel slope from 119.73 to 102.65 mV dec^{-1}. The fluorinated oxide demonstrated prolonged stability for over 100 h without significant changes in composition.

In 2021, the Dai group proposed a perovskite oxide-halide solid solution concept, experimentally merging perovskite oxide and perovskite halide into a single lattice phase through high-energy ball milling (Fig. 8f).[132] They optimized a combination of $\frac{3}{4}$ of BSCF with $\frac{1}{4}$ of KM(II)F_3 to achieve an overpotential of 345 mV at 10 mA cm^{-2}, significantly lower than the 450 mV overpotential of BSCF without F.

Besides the fluorination of simple cubic perovskites, it was shown that fluorination of a hexagonal $Sr_2Co_2O_5$ phase produces a cubic $SrCoO_{2.85-d}F_{0.15}$ perovskite, with improved OER activities (Table 3).[14] According to DFT calculations, F doping and the resulting structural transition improve electronic conductivity and increase the number of reactive O species of $O_2^{\ 2-}$ and O^- for the OER.

Fluorination of Ruddlesden–Popper (R–P) perovskite oxides with their layered structure has also been reported.[136,146] $La_{1.2}Sr_{0.8}Ni_{0.6}Fe_{0.4}O_{4+\delta}$ (LSNF) was synthesized *via* a sol–gel method and subsequently fluorinated by calcination at 370 °C with PVDF to obtain microfluorinated LSNF (LSNF-MF).[136] Finally, LSNF-MF was calcined at a high temperature of 900 °C, resulting in fully fluorinated perovskite oxyfluoride $La_{1.2}Sr_{0.8}Ni_{0.6}Fe_{0.4}O_{4+\delta}\ F_y$ (LSNF-OF). LSNF-MF reduced the overpotential at 10 mA cm^{-2} from 484 mV to 377 mV (estimated in this study), while LSNF-OF further reduced it to 308.1 mV. LSNF-OF is considered a triple-conductive oxide (conductive for H^+, O^{2-} and electrons).

(7) Fluorinated mixed oxides. The fluorination of mixed oxides has also been reported in the literature. Recently, FeCo–O bimetallic oxide was synthesized by calcinating Fe and Co nitrates at a relatively low temperature of 400 °C, resulting in mixed Co_3O_4 and $CoFe_2O_4$ phases, both of which belong to the spinel oxide type.[44] For comparison, Fe–O and Co–O oxides are also prepared. Fluorination significantly reduced the overpotentials and Tafel slopes of all FeCo, Fe–O, and Co–O materials (as shown in Table 3), with a more pronounced effect on the bimetallic oxide. The authors believe that the synergistic effect of Fe and Co bimetals enhances electron transport, and the fluorine dopant reduces charge density in Fe and Co phases, facilitating OH^- adsorption.

4.3 Fluoride/oxide heterocatalysts

It is known that metal oxides have demonstrated high performances in the OER,[5,49,110,111] and so have metal fluorides, though these fluorides contain multiple metal elements, as mentioned in Section 3. In Sections 4.1 and 4.2, we demonstrated that the addition of oxygen to fluorides, either in the form of oxyfluorides or fluorinated oxides, can further improve OER performance compared to pristine materials. But what about a heterocatalyst combining both fluoride and oxides? Such fluoride/oxide heterocatalysts have been reported, as summarized in Table 4.

A heterocatalyst consisting of Fe_2O_3 and FeF_2, referred to as an iron fluoride-oxide nanoporous film (IFONF), was prepared

Table 4 Summary of representative OER performance of fluoride/oxide heterocatalysts

Catalyst	Overpotential at specific current density	Tafel slope (mV dec^{-1})	Tested durability	Electrolyte	Source
IFONFs-45	260 mV@10 mA cm^{-2}	45	8.33 h@40 mA cm^{-2}	1 M KOH	20
$NiCo_2O_4/NiO/CoF_2@mC_{700}$	240 mV@10 mA cm^{-2}	78	40 h@10 mA cm^{-2}	0.1 M KOH	147
CFO-RH400	230 mV@10 mA cm^{-2}	68.7	45 h@10 mA cm^{-2}	1 M KOH	148
$Co/Co_3O_4/CoF_2$@NSC-CC	310 mV@10 mA cm^{-2}	88	1000 h@10 mA cm^{-2} (ZAB)	0.1 M KOH	149
Co/Co_3O_4@NC	430 mV@10 mA cm^{-2}	134	—		
Co_3O_4–CoF_2	169 mV@10 mA cm^{-2}	63.5	72 h@10–100 mA cm^{-2}	1 M KOH	150
CoF_2	295 mV@10 mA cm^{-2}	83.9	–		
Co_3O_4	301 mV@10 mA cm^{-2}	84.1	–		

by anodization followed by fluorination using a piece of Fe foil, as depicted in Fig. 9a.[20] After the anodization of the Fe foil, a porous Fe-oxide thin film (PTF) is formed. Subsequent fluorination results in the formation of IFONFs. Both XRD and TEM observations (Fig. 9b) confirm the formation of mixed Fe_2O_3 oxide and FeF_2 fluoride phases. The IFONFs-45 catalyst, with 45 min of fluorination, showed an overpotential of 260 mV at a current density of 10 mA cm^{-2}, which is higher than that of RuO_2 (170 mV) but lower than that of Fe-oxide (480 mV). Its Tafel slope was 45 mV dec^{-1}, which is lower than that of Fe-oxide (207 mV dec^{-1}) and RuO_2 (125 mV dec^{-1}), implying different RDSs for the given pathway. The enhanced OER activities could be attributed to the increased active sites and reduced charge-transfer resistance in the heterocatalyst.

Since spinel $NiCo_2O_4$ has demonstrated effective electrochemical activity toward the OER,[151] a heterocatalyst consisting of $NiCo_2O_4$, NiO and CoF_2 was prepared.[147] Starting from a bimetallic NiCo-MOF with an equal molar ratio of Ni and Co,

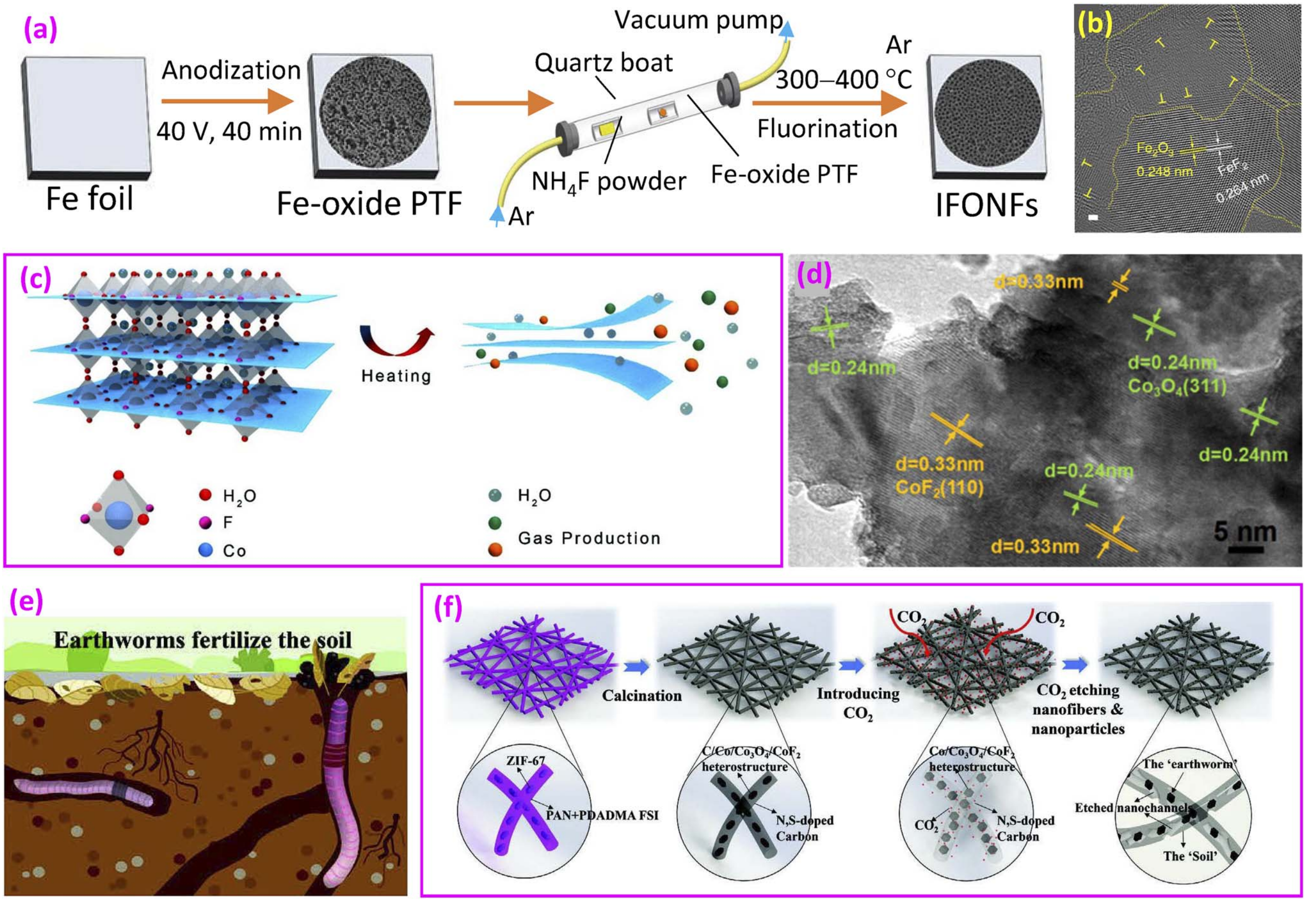

Fig. 9 Fluoride/oxide heterocatalysts. (a) Synthesis of an iron fluoride-oxide nanoporous film (IFONF); (b) TEM image of the IFONF. Reproduced from ref. 20 with open access; (c) schematic illustration of the exfoliation of cobalt fluoride hydrate to ultrathin 2D CFO-RH400 nanosheets, driven by the rapid thermally generated and released water or other gaseous products; and (d) TEM image of CFO-RH400 nanosheets. Reproduced from ref. 148 with permission from American Chemical Society, copyright 2020. (e) Earthworms fertilizing the soil and (f) synthesis route of $Co/Co_3O_4/CoF_2$@NSC-CC. Reproduced from ref. 149 with permission from John Wiley and Sons, copyright 2024.

fluorination using NH_4F followed by high-temperature calcination produced a mixture of $NiCo_2O_4/NiO/CoF_2$. The hybrid material delivers an overpotential of 240 mV at 10 mA cm^{-2} and a Tafel slope of 78 mV dec^{-1}. The F doping in this hybrid material is thought to enhance charge transfer, improving both OER and HER activities.

Considering the unique structural features of 2D catalysts, such as large exposed surface areas with active sites,[152,153] 2D cobalt-fluoride-oxide (CFO) nanosheets were prepared. A method to obtain 2D Co fluoride-oxide was demonstrated through exfoliation by a rapid thermal annealing process (Fig. 9c).[148] The material structure includes CoF_2 fluoride and spinel Co_3O_4 oxide (Fig. 9d). The catalyst displayed a Tafel slope of 68.7 mV dec^{-1}, lower than that of IrO_2 (73.8 mV dec^{-1}), indicating good OER kinetics and better catalytic activity. Nyquist electrochemical impedance spectroscopy revealed the smallest high-frequency interfacial charge-transfer resistance (R_{ct1}), suggesting that the coexistence of M–O bonds and M–F bonds facilitates the charge transfer process and enhances the reaction kinetics.

Drawing inspiration from earthworms' soil fertilization process (Fig. 9e), researchers developed nanofibers consisting of $Co/Co_3O_4/CoF_2$@N and sulfur-enriched carbon with restricted channels (NSC-CC).[149] The fabrication method involved placing ZIF-67 nanoparticles on freshly spun nanofibers, followed by a calcination step. This process resulted in the formation of $Co/Co_3O_4/CoF_2$ heterojunction particles embedded within the carbon framework (Fig. 9f). Carbon dioxide was subsequently introduced to create micro- and mesopores on the nanofiber surface. The N and S co-doped carbon matrix serves as "nano-soil", while the $Co/Co_3O_4/CoF_2$ heterostructure particles function as "nano-earthworms". This heterogeneous catalyst demonstrated an overpotential of 310 mV at 10 mA cm^{-2}, which is considerably lower than the overpotential of 430 mV observed in the catalyst lacking CoF_2 and confined channels.

In a recent report, a cobalt oxide-fluoride heterojunction catalyst was synthesized on carbon cloth using a hydrothermal method.[150] Subsequent heat treatment at 400 °C for 1 h in different atmospheres yielded varying results: an Ar environment produced a blend of Co_3O_4 and CoF_2, air calcination led to Co_3O_4 formation, and an atmosphere with added NH_4F resulted in CoF_2. The research indicated that the heterocatalyst comprising mixed oxide and fluoride phases showed enhanced performance compared to individual oxide or fluoride components (Table 4). The interface between Co_3O_4 and CoF_2 likely modifies the surface electronic configuration, leading to improved OER kinetics.

5. Fluorinated (oxy)hydroxides, carbonate hydroxides and their derived fluorides

A simple metal hydroxide is expressed as $M^{n+}(OH)_n$, where metal M has a valence of n+. A meal oxyhydroxide is expressed as MO_xH, where $x = (n + 1)/2$ for the metal M^{n+}.[154] These compounds share a structural commonality in that they contain hydrogen in their structure. Transition-metal hydroxide and oxyhydroxide materials have been widely used for OER research due to several advantages, such as their distinct layered structure with large surface areas that favor the OER, excellent catalytic activity, high stability, and ease of preparation.[155–160] Through fluorination, these materials have been reported to exhibit improved OER performance.

5.1 Fluorinated hydroxides

(1) Fluorinated divalent $M(OH)_2$ hydroxides. There are two important divalent $M(OH)_2$ hydroxides, namely, β-$Ni(OH)_2$ and α-$Ni(OH)_2 \cdot xH_2O$. β-$Ni(OH)_2$ exists naturally as the mineral theophrastite, with a trigonal structure and a space group of $P\bar{3}1m$, containing edge-sharing hexagonally packed $Ni(OH)_6$ octahedral layers (Fig. 10a).[165,166] The spacing between the layers is 0.256 nm, which includes the hydrogen atoms on the distorted tetrahedral sites directed toward the adjacent layer. It is isostructural with other compounds when M = Mg (brucite), Ca (portlandite), Cd, and Co. α-$Ni(OH)_2 \cdot xH_2O$ also has a trigonal structure with the same space group and similar $Ni(OH)_6$ octahedral layers, as proposed by Bode *et al.*[167] However, between the (001) planes, there are disordered H_2O layers, resulting in an increase in the c-axis constant to $c = 0.8$ nm (Fig. 10b).[168,169] The degree of hydration varies within the range $x = 0.41–0.7$, and the space between the octahedral layers reaches 0.596 nm.[169] However, the trivalent structure of $Fe(OH)_3$ is a 3D perovskite structure.[170]

The OER activities of fluorinated divalent hydroxides are listed in Table 5.

Several approaches have been proposed for synthesizing fluorinated hydroxides. Hussain *et al.* synthesized ultrathin mesoporous $Ni(OH)_2$ nanosheets by a hydrothermal method.[161] Fig. 10c demonstrates that α-$Ni(OH)_2$ exhibits higher activity compared to β-$Ni(OH)_2$, attributed to their structural variations. The introduction of F doping results in a significant decrease in the Tafel slope, from 128.34 mV dec^{-1} for α-$Ni(OH)_2$ to a mere 31.89 mV dec^{-1}, representing a 75.2% reduction. Additionally, the overpotential decreases from 430 mV for α-$Ni(OH)_2$ to 325 mV at 10 mA cm^{-2}. Computational studies using DFT indicate that the F-doped sample possesses lower adsorption energy, facilitating more rapid charge transfer. Fluorinated NiFe binary hydroxide nanosheets were also synthesized using the hydrothermal method with the addition of NH_4F.[15,175]

As illustrated in Fig. 10d, F-doped α-$Ni(OH)_2$ flakes were formed on a flat Ni foam surface through a hydrothermal reaction using Ni nitrate and urea precursors.[162] Subsequently, a secondary reaction occurred where manganese nitrate was introduced to the precursor, resulting in the formation of Mn^{2+} and F^- co-doped $Ni(OH)_2$ flakes. These flakes were grown perpendicular to the Ni foam surface (Fig. 10e). The F doping could reduce the band gap and improve the conductivity and introduce oxygen vacancies to facilitate the OER. Patil *et al.* synthesized ultrathin 2D $Ni(OH)_2$ nanosheets on 3D Ni foam through a hydrothermal route, where the Ni foam served as the Ni source and added NH_4F was the F source.[172] The F-doped

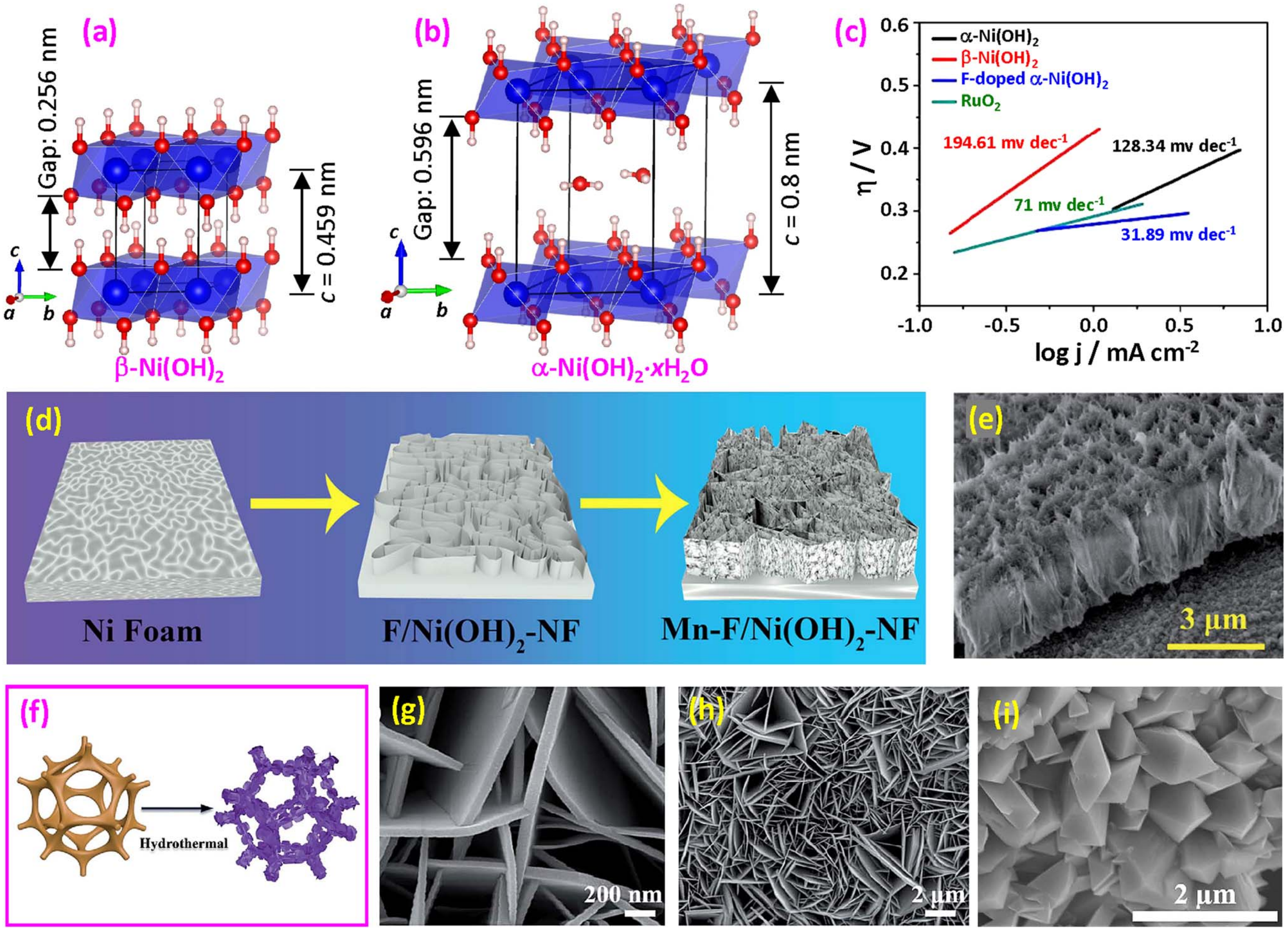

Fig. 10 (a) Structural model of β-$Ni(OH)_2$; (b) structural model of α-$Ni(OH)_2$. (c) Tafel slope of OER catalysts. Reproduced from ref. 161 with permission from the Royal Society of Chemistry, copyright 2019. (d) Synthesis of Mn and F doped $Ni(OH)_2$ on NF and (e) SEM side view of Mn-F/$Ni(OH)_2$-NF. Reproduced from ref. 162 with open access. (f) Synthesis of $Co_xFe_y(OH)F$ *via* a one-step hydrothermal procedure; (g and h) SEM images. Reproduced from ref. 163 with permission from the Royal Society of Chemistry, copyright 2022. (i) SEM image of Co(OH)F. Reproduced from ref. 164 with permission from Elsevier, copyright 2022.

$Ni(OH)_2$ sample exhibited a well-defined nanosheet structure. The study revealed that F–$Ni(OH)_2$ necessitates only 280 mV to achieve 50 mA cm^{-2}, whereas unmodified $Ni(OH)_2$ requires 320 mV. Additionally, the F-doped specimen exhibited a reduced Tafel slope of 97.81 mV dec^{-1}, in contrast to the 126.64 mV dec^{-1} observed for the unmodified sample.

Table 5 Summary of representative OER performance of fluorinated divalent $M(OH)_2$ hydroxides[a]

Catalyst	Overpotential at specific current density	Tafel slope (mV dec^{-1})	Tested durability	Electrolyte	Source
NiFe-OH-F-SR	181 mV@10 mA cm^{-2}	22.6	165 h@50 mA cm^{-2}	1 M KOH	15
NiFe–OH–F	243 mV@10 mA cm^{-2}	42.9	—		
F-doped α-$Ni(OH)_2$	325 mV@10 mA cm^{-2}	31.89	30 h@25 mA cm^{-2*}	1 M KOH	161
α-$Ni(OH)_2$	430 mV@10 mA cm^{-2}	128.34	—		
β-$Ni(OH)_2$	—	194.61	—		
(Mn-F/$Ni(OH)_2$-NF	233 mV@20 mA cm^{-2}	56.9	10 h@20 mA cm^{-2}	1 M KOH	162
2CoNiFe	224 mV@10 mA cm^{-2}	42	22 h@10 mA cm^{-2}	1 M KOH	171
F-$Ni(OH)_2$-16 h	200 mV@10 mA cm^{-2}	97.81	24 h@12 mA cm^{-2*}	1 M KOH	172
$Ni(OH)_2$-16 h	340 mV@10 mA cm^{-2}	159.03	—		
Co(OH)F	273 mV@10 mA cm^{-2}	45	20 h@10 mA cm^{-2}	1 M KOH	164
$Co_{0.21}Fe_{0.28}(OH)F$	195 mV@10 mA cm^{-2}	89.9	120 h@20 mA cm^{-2}	1 M KOH	163
V–$Co(OH)_2$	136 mV@10 mA cm^{-2}	51.6	72 h@10 mA cm^{-2}	1 M KOH	173
Fluorinated Ni/Fe hydroxide	240 mV@10 mA cm^{-2}	47	8.33 h@1.58 mA cm^{-2}	0.1 M KOH	174

[a] (*) Estimated in this study.

According to DFT calculations, the introduction of fluorine doping resulted in a reduction of the bandgap from 2.19 eV to 1.25 eV. It was found that the Ni atoms located near the F dopants contribute to the improved electrical conductivity, while the F itself does not directly contribute. Instead of using flat NF, another study by Li *et al.* demonstrates the growth of CoFeOHF nanosheets on 3D NF *via* a one-step hydrothermal process, as shown in Fig. 10f.[163] Regular nanosheets were formed on the NF, as imaged in Fig. 10g and h.

Rajesh *et al.* reported the synthesis of cobalt fluoride hydroxide, Co(OH)F, using nickel nitrate and NH_4F as precursors in a hydrothermal reaction.[164] The synthesized material displayed different crystallite shapes, ranging from 0.3 to 0.5 µm in size (Fig. 10i). Co(OH)F has an orthorhombic structure, which differs from that of $Co(OH)_2$ and exhibits active OER performance (as shown in Table 5). Recently, a liquid phase deposition method was used to synthesize F-doped α-$Ni(OH)_2$.[176]

(2) Fluorinated layered double hydroxides with mixed valence. In the structure of divalent α-$Ni(OH)_2\cdot xH_2O$, the $Ni(OH)_6$ octahedral layer is neutral and the interlamellar layer contains only neutral water molecules (Fig. 10b). In the structure of layered double hydroxides (LDHs), a portion of the M^{2+} divalent metal cations undergo isomorphous substitution with M^{3+} trivalent metal cations. This structural arrangement can be represented by a general formula $[M_{1-x}{}^{2+}M_x{}^{3+}(OH)_2{}^{-}]\cdot[A_{x/n}{}^{n-}\cdot mH_2O]$. The expression contains two components: the initial bracket denotes the octahedral layer resembling brucite, which carries a positive charge of x^+. The subsequent bracket signifies the intercalated layer, bearing a negative charge of x^- to balance the positive charge from the octahedral layer. The value of x is the molar ratio of $M^{2+}/(M^{2+} + M^{3+})$, typically ranging from 0.2 to 0.33.[177] An example of CoFe LDHs is shown in Fig. 11a, expressed as $[Co_{18}{}^{2+}Fe_6{}^{3+}(OH)_{48}{}^{-}]$ $[3(CO_3)^{2-}$ $12H_2O]$ in a unit cell, where negatively charged $(CO_3)^{2-}$ and neutral water molecules fill the space between the positively charged octahedral layers.[181]

The OER activities of fluorinated LDHs are listed in Table 6.

Fig. 11b demonstrates the application of a CHF_3-plasma etching method to incorporate F into ultrathin Co_3Fe LDHs.[178] The F-doped F-Co_3Fe LDHs exhibit an overpotential of 287 mV to afford 10 mA cm^{-2}, while the pristine Co_3Fe LDHs exhibit a higher overpotential of 329 mV. Compared to the pristine sample with a Tafel slope of 62.87 mV dec^{-1}, the fluorine-doped specimen exhibits a reduced Tafel slope of 39.17 mV dec^{-1}. The layers along the *c*-axis exhibit nearly hexagonal shapes (Fig. 11c). It is believed that F ions filled oxygen vacancies to form metal–fluorine bonds, which can strongly modulate the electronic structure, facilitating the adsorption of OER intermediates and decreasing the reaction barriers. Tong *et al.* synthesized NiAl LDHs on NF and then fluorinated NiAl LDHs for comparison.[31] The F-doped NiAl LDHs exhibited more active OER properties than the non-fluorinated ones. During the OER process, with the leaching of F, the metal–F bonds converted to

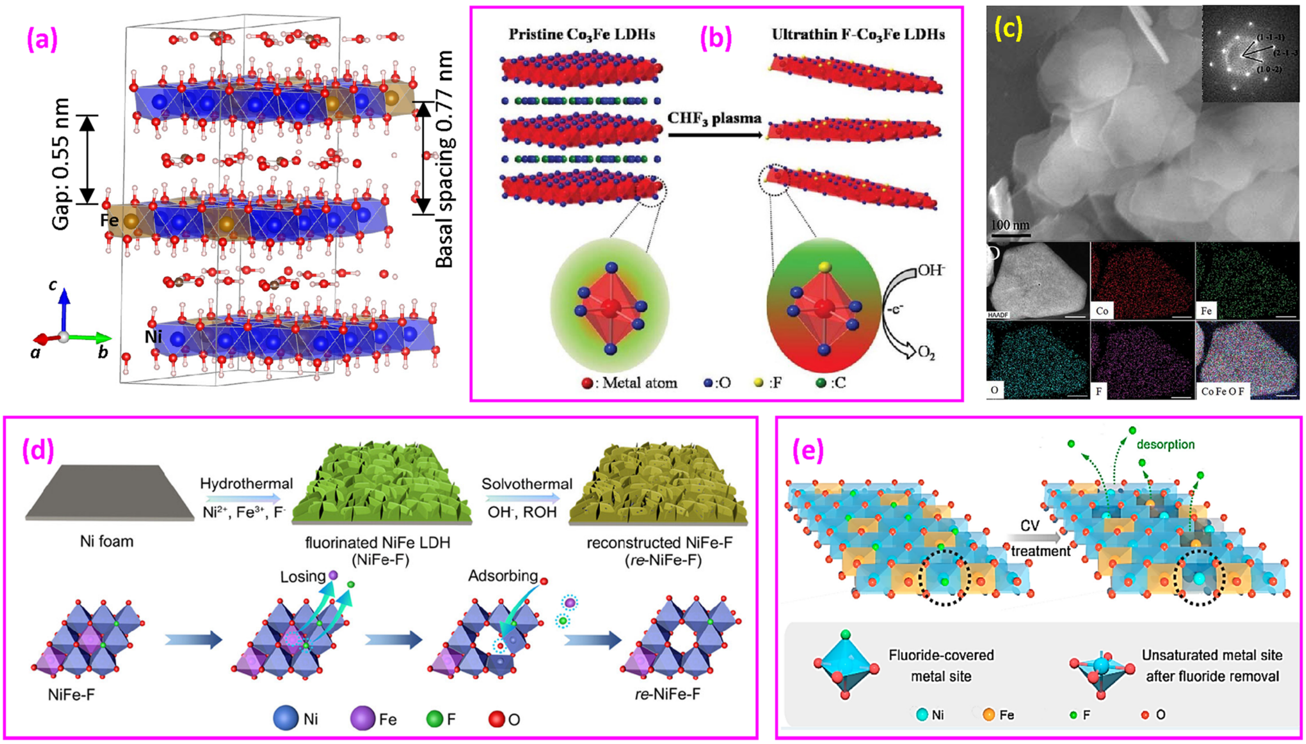

Fig. 11 (a) Structural model of NiFe LDH. (b) Synthesis of F-doped Co_3Fe LDHs and (c) TEM image (upper) and EDS maps (bottom) of Co_3Fe LDHs. Reproduced from ref. 178 with permission from the Royal Society of Chemistry, copyright 2019. (d) Structural reconfiguration process to obtain reconstructed NiFe–F (re-NiFe–F). Reproduced from ref. 179 with permission from American Chemical Society, copyright 2023. (e) Fluorine pre-covered surface strategy, where F ions are removed by CV scans to improve the OER. Reproduced from ref. 180 with permission from American Chemical Society, copyright 2020.

Table 6 Summary of representative OER performance of LDHs with mixed valence[a]

Catalyst	Overpotential at specific current density	Tafel slope (mV dec$^{-1\cdot}$)	Tested durability	Electrolyte	Source
F-Co_3Fe LDH	287 mV@10 mA cm^{-2}	39.17	—	1 M KOH	178
Co_3Fe LDH	329 mV@10 mA cm^{-2}	62.87	—	1 M KOH	
Fe-Ni-F-250	225 mV@10 mA cm^{-2}	79	10 h@10 mA cm^{-2}	1 M KOH	182
FeNi-LDH	316 mV@10 mA cm^{-2}	101	—	1 M KOH	
F-NiAl LDH-NF	250 mV@10 mA cm^{-2}	77	12 h@28.6 mA cm^{-2*}	1 M KOH	31
NiAl LDH-NF	300 mV@10 mA cm^{-2}	132	—	1 M KOH	
NiFe LDH-0.20 M	243 mV@10 mA cm^{-2}	50	10 h@1.580 V	1 M KOH	180
NiFe LDH-0 M	323 mV@10 mA cm^{-2}	77*	—	1 M KOH	
Fe-CoF_2-300	230 mV@10 mA cm^{-2}	41.9	10 h@10 mA cm^{-2}	1 M KOH	183
CoFe LDH	290 mV@10 mA cm^{-2}	72.7	—	1 M KOH	
F-FeCoNi-O_v LDH/NF	243.9 mV@50 mA cm^{-2}	57.8	50 h@1.5 V	1 M KOH	184
F-FeCoNi LDH/NF	257.1 mV@50 mA cm^{-2}	109.6	—	1 M KOH	
FeCoNi LDH/NF	273.3 mV@50 mA cm^{-2}	126.2	—	1 M KOH	
re-NiFe-F-CV	152 mV@10 mA cm^{-2}	92.1	100 h@10 mA cm^{-2}	1 M KOH	179
NiFe-F-CV	194 mV@10 mA cm^{-2}	106.3	—	1 M KOH	
NiFe-F	277 mV@10 mA cm^{-2}	112.0	—	1 M KOH	
FeCoNi LDH/NF-3.0 mM	196 mV@10 mA cm^{-2}	22	120 h@100 mA cm^{-2}	1 M KOH	185
FeCoNi LDH/NF-pristine	243 mV@10 mA cm^{-2*}	39	—	1 M KOH	
10F-NiCo	240 mV@10 mA cm^{-2}	—	—	1 M KOH	186
0F-NiCo	303 mV@10 mA cm^{-2}	—	—	1 M KOH	

[a] (*) Estimated in this study.

form highly active Ni–OOH species, which enhances the efficiency of the oxygen evolution reaction (OER).[31]

As illustrated in Fig. 11d, a hydrothermal method was employed to cultivate F–NiFe LDHs on a nickel foam substrate.[179] Subsequently, the precursor underwent a solvothermal process, resulting in the formation of reconstructed NiFe LDHs. The role of F was to facilitate surface reconstruction during the solvothermal processing, which involved the extraction of some metal ions (primarily Fe^{3+}) and fluoride anions. This process generated voids and unsaturated coordination sites, facilitating the OER. The reconstructed product was then electrochemically activated by 30 CV scans at room temperature (denoted as re-NiFe LDH-F-CV). The reconstruction and CV activation significantly enhanced OER performance (Table 6). The formation of cavities following reconstruction enhances the adsorption process during the OER.

When NiFe LDHs were synthesized hydrothermally without the addition of NH_4F, the resulting product exhibited a nearly spherical morphology and low degree of crystallinity,[180] while with the addition of NH_4F, $[FeF_n]^{(n-3)-}$ complex ions are formed, resulting in a product with an enhanced layered structure and increased crystallinity. In the case of fluorinated LDHs, F ions initially occupied the surface. To create highly active OER sites, an electrochemical process involving 2000 CV scans was employed to eliminate the surface F ions, exposing unsaturated metal sites (Fig. 11e). The sample synthesized with 0.2 M NH_4F and treated by CV scans exhibits an overpotential of 243 mV@10 mA cm^{-2} and a Tafel slope of 50 mV dec^{-1}, significantly lower than those of the sample without F, which had an overpotential of 323 mV and a Tafel slope of 77 mV dec^{-1}. CV scan appears to be an effective way to boost the OER.

Yang *et al.* prepared LDHs with three metal cations Co^{2+}, Ni^{2+} and Fe^{3+}, with a Co/Ni/Fe ratio of about 1 : 1 : 2, and added different concentrations of NH_4F in a solvothermal reaction.[185] The research revealed that at a NH_4F concentration of 3.0 mM, the catalyst demonstrated remarkable performance. It achieved a current density of 10 mA cm^{-2} with an exceptionally low overpotential of 196 mV, while exhibiting a Tafel slope as minimal as 22 mV dec^{-1}. It was experimentally found that the F^- ions leached gradually during the OER, promoting the formation of high-valent intermediates at the Co active site to enhance the catalyst activity. A recent DFT study reveals the interaction between the doped F in NiCo LDH and molecular orbitals.[186] The fluorine atoms alter the active site by influencing the oxidation state of the metallic elements. A series of fluorinated NiCo LDHs were synthesized, and the lowest overpotential was recorded at 240 mV at 10 mA cm^{-2}.

5.2 Fluorinated oxyhydroxides

Metal hydroxides and oxyhydroxides can transform under certain conditions. In the nickel metal system, there are various phases such as α-$Ni(OH)_2$, β-$Ni(OH)_2$, β-NiOOH, and γ-NiOOH.[187] The Bode diagram[167] of this system is shown in Fig. 12a, which outlines these phase transformations under different conditions.[187,188] The OER activities of oxyhydroxides and carbonate hydroxides are listed in Table 7.

Fluorinated oxyhydroxide has been reported to be synthesized *via* anodic electrooxidation. As shown in Fig. 12b, in the first step, $Ni(OH)_2$ nanostructures on NF are synthesized through a hydrothermal route.[189] Following this, the surface of $Ni(OH)_2$ undergoes anodic electrooxidation in an alkaline solution containing fluorine. This process results in the formation of an F-doped Ni oxyhydroxide layer. As illustrated in the TEM image in Fig. 12c, this layer is typically amorphous and semicontinuous and has a thickness of less than 3 nm. Compared to the undoped

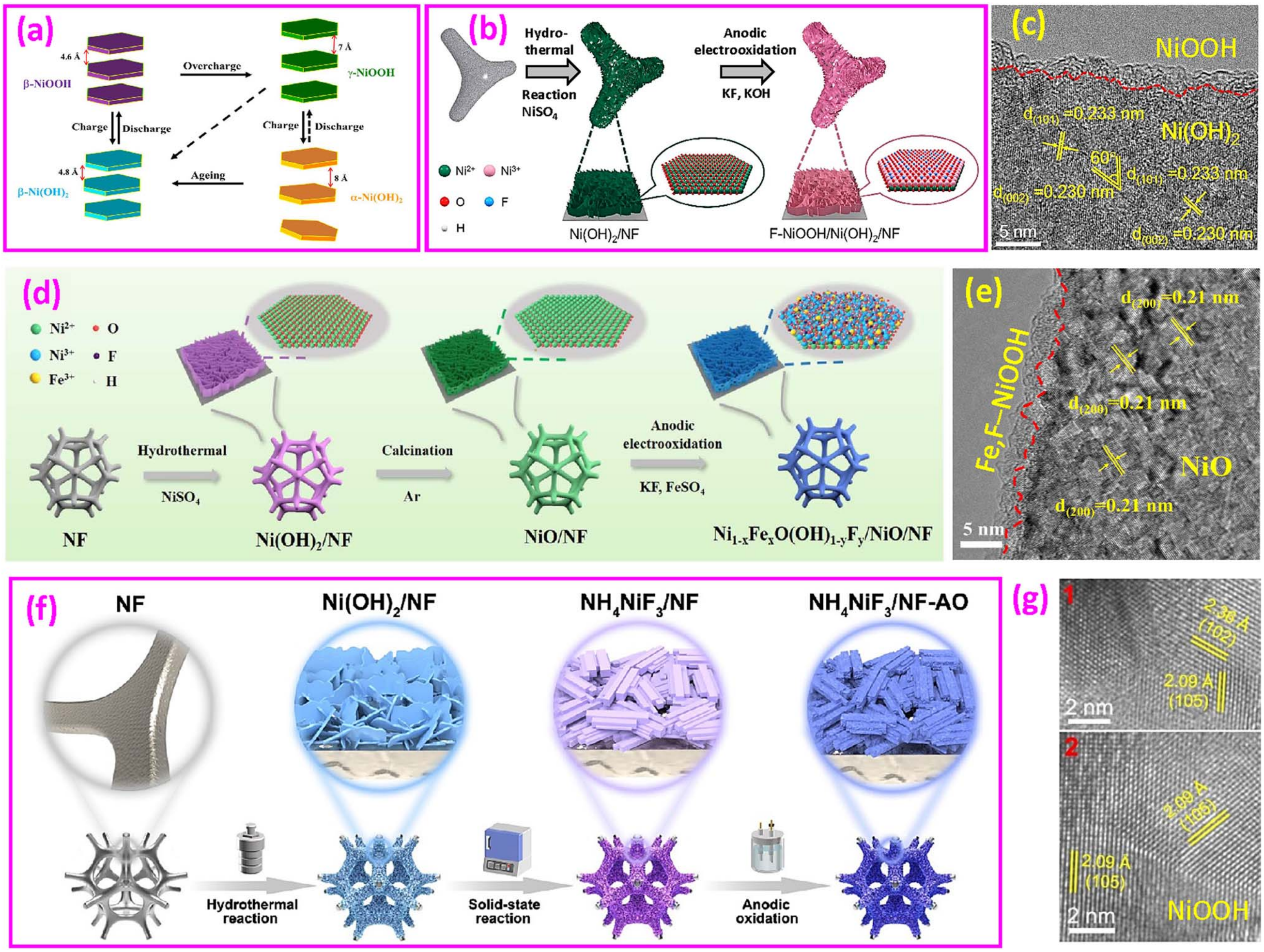

Fig. 12 (a) Bode diagram representing the transformation of various nickel (oxy)hydroxides. Reproduced from ref. 188 with open access. (b) Synthesis of F-doped NiOOH/$Ni(OH)_2$/NF and (c) TEM image showing NiOOH on the surface. Reproduced from ref. 189 with permission from Elsevier, copyright 2023. (d) Synthetic process of $Ni_{1-x}Fe_xO(OH)_{1-y}F_y$/NiO/NF and (e) TEM image showing Fe, F–NiOOH. Reproduced from ref. 190 with permission from the Royal Society of Chemistry, copyright 2023. (f) Progressive reconstruction strategy to synthesize F-doped NiOOH and (g) TEM iamges showing NiOOH. Reproduced from ref. 191 with permission from the Royal Society of Chemistry, copyright 2024.

sample, F-NiOOH/$Ni(OH)_2$/NF showed a reduction in overpotential by 32 mV, a Tafel slope reduction by 50 mV dec^{-1}, and significantly improved stability over 100 h. According to DFT calculations, F doping enhances the transfer of electrons from nickel to neighboring fluorine atoms. This leads to stronger OH adsorption and improves the rate-limiting step of deprotonation.

In another comparative study, F-doped Ni hydroxide was synthesized through an NH_4F-mediated hydrothermal route, resulting in crystalline $Ni_3O_2(OH)_4$.[193] This sample requires only 230 mV to maintain 10 mA cm^{-2}, with a Tafel slope of 107 mV dec^{-1}, while the F-free sample, $Ni_3(OH)_4(NO_3)_2$, required 340 mV to maintain 10 mA cm^{-2}, with a Tafel slope of 118 mV dec^{-1}. The incorporation of F anions increased the Ni^{3+} content, hydrophilicity, and structural stabilities for the OER. F doping also improved the OER activity of NiO_xH_y.[196]

Starting from a Co-based precursor, $Co(CO_3)_xOH_y$ on NF, Chen *et al.* synthesized F-doped and undoped Co_3O_4 nanoparticles and F-doped crystalline CoOOH nanosheets for comparative studies.[13] Materials doped with F demonstrated enhanced catalytic performance (Table 7), which was attributed to the distribution of F anions on the catalyst's surface and the resulting increase in hydrophilicity. DFT calculations reveal that F-doped crystals possess increased DOS at the conduction band edge compared to unmodified crystals, indicating that more carriers can be effectively transferred to the conduction band. An alternative synthesis method was reported using an anodized commercial FeNiCo alloy.[194] The anodized layer containing $(FeNiCo)F_2$ readily converts into a highly active porous oxyhydroxide (FeNiCo)OOH during anodic polarization in KOH. After only five CV cycles, the composition largely changed to F-doped oxyhydroxide.

An approach to co-dope Fe and F into nickel oxyhydroxide is illustrated in Fig. 12d.[190] First, $Ni(OH)_2$ is formed on NF. After calcination, NiO is formed on NF. Finally, anodic electrooxidation is conducted to produce $Ni_{1-x}Fe_xO(OH)_{1-y}F_y$, *i.e.*, Fe and F doped NiOOH, in the form of an amorphous layer with 2 nm thickness on the surface, as shown in the TEM image in Fig. 12e. The optimized catalyst, $Ni_{1-x}Fe_xO(OH)_{1-y}F_y$/NiO/NF, exhibited excellent OER performance with a low overpotential

Table 7 Summary of representative OER performance of oxyhydroxides and carbonate hydroxides[a]

Catalyst	Overpotential at specific current density	Tafel slope (mV dec^{-1})	Tested durability	Electrolyte	Source
Oxyhydroxides					
F modified β-FeOOH	360 mV@10 mA cm^{-2}	74.4	6 h@10–30 mA cm^{-2}	1 M KOH	192
β-FeOOH	410 mV@10 mA cm^{-2}	81.5	6 h@10–30 mA cm^{-2}	1 M KOH	
$Fe_{1.9}F_{4.75}\cdot 0.95H_2O$	320 mV@10 mA cm^{-2}	44.6	6 h@10–30 mA cm^{-2}	1 M KOH	
F-CoOOH/NF	310 mV@50 mA cm^{-2}	54	10 h@1.55 V	1 M KOH	13
CoOOH/NF	370 mV@50 mA cm^{-2}	83	—		
F-NHO	280 mV@10 mA cm^{-2}	107	24 h@20 mA cm^{-2} (91.3% retention)	1 M KOH	193
NHN	340 mV@10 mA cm^{-2}	118	24 h@20 mA cm^{-2} (59.3% retention)	1 M KOH	
NiFe-PBAs-F	190 mV@10 mA cm^{-2}	57	50 h@200 mA cm^{-2}	1 M KOH	35
NiFe-PBAs-Ar	290 mV@10 mA cm^{-2}	66.7	—	1 M KOH	
FeNiCo anodized 250 s	260 mV@10 mA cm^{-2}	42	200 h@100 mA cm^{-2}	1 M KOH	194
As received	342 mV@10 mA cm^{-2}	40	81 h@100 mA cm^{-2*}	1 M KOH	
Ni_yFe_xOOH-20F	259 mV@100 mA cm^{-2}	60.3	24 h@50–200 mA cm^{-2}	1 M KOH	195
Ni_yFe_xOOH-0F	320 mV@100 mA cm^{-2}	105.6	—	1 M KOH	
$Ni_{1-x}Fe_xO(OH)_{1-y}F_y$/NiO/NF	186 mV@10 mA cm^{-2}	32	100 h@500 mA cm^{-2}	1 M KOH	190
$Ni_{1-x}Fe_xOOH$/NiO/NF	225 mV@10 mA cm^{-2}	55	—		
R′-NiF_2 (NiOOH)	228 mV@10 mA cm^{-2}	54.3	15 days@10–100 mA cm^{-2}	1 M KOH	43
$Ni(OH)_2\cdot 0.75H_2O$	332 mV@10 mA cm^{-2}	96.4	—	1 M KOH	
Fe–F–NiO_xH_y	322 mV@10 mA cm^{-2}	—	—	1 M KOH	196
Fe–NiO_xH_y	337 mV@10 mA cm^{-2}	—	—	1 M KOH	
F-NiOOH/$Ni(OH)_2$/NF	268 mV@10 mA cm^{-2}	39	100 h@100 mA cm^{-2}	1 M KOH	189
NiOOH/$Ni(OH)_2$/NF	300 mV@10 mA cm^{-2}	89	—		
NH_4NiF_3/NF-AO	240 mV@10 mA cm^{-2}	59.5	400 h@20–200 mA cm^{-2}	1 M KOH	191
$Ni(OH)_2$/NF	368 mV@10 mA cm^{-2}	126.1	—	1 M KOH	
Carbonate hydroxides					
F-$(MnCo)(CO_3)_{0.5}(OH)_{0.11}\cdot H_2O$	240 mV@10 mA cm^{-2}	78	24 h@10 mA cm^{-2}	1 M KOH	197
$(MnCo)(CO_3)_{0.5}(OH)_{0.11}\cdot H_2O$	270 mV@10 mA cm^{-2}	219	—	1 M KOH	

[a] (*) Estimated in this study.

of 186 mV to reach 10 mA cm^{-2}, and a long stability over 100 h at 500 mA cm^{-2}.

Recently, a progressive reconstruction method was proposed to synthesize F-doped NiOOH.[191] Fig. 12f illustrates the process of growing $Ni(OH)_2$ nanosheets on NF through hydrothermal synthesis. Subsequently, $Ni(OH)_2$/NF underwent heating at 300 °C for 30 min in molten ammonium fluoride, resulting in NH_4NiF_3/NF formation. The final step involved *in situ* activation *via* anodic oxidation, yielding the desired F-doped NiOOH/NF. TEM images in Fig. 12g confirm that the end product is crystalline γ-NiOOH. This fabricated catalyst showed favorable OER performance with a low overpotential of 240 mV to afford 10 mA cm^{-2} and maintained stability at 20–200 mA cm^{-2} for over 300 h.

Interestingly, phase transitions between hydroxides, fluorides, and oxyhydroxides were recently identified.[43] Using hydrothermal synthesis, flower-like $Ni(OH)_2\cdot 0.75H_2O$ was obtained. After fluorination at 450 °C for 1 h in the presence of NH_4, the sheet-like hydroxide converted into cubic NiF_2 nanoparticles. After CV testing the fresh NiF_2 under HER and OER conditions, NiF_2 transformed into $Ni(OH)_2$ and NiOOH, respectively.

5.3 Fluorinated carbonate hydroxide

Shamloofard and Shahrokhian synthesized MnCo carbonate hydroxide $(MnCo)(CO_3)_{0.5}(OH)_{0.11}\cdot H_2O$ on graphite paper, using NH_4F as the fluorine source to control the product's shape.[197] The unaltered MnCo carbonate hydroxide displayed spherical formations made up of needle-like structures. However, when NH_4F was introduced, the morphology transformed into cubic and pyramidal shapes. The F-doped material showed an overpotential of 240 mV to reach 10 mA cm^{-2} and a Tafel slope of 78 mV dec^{-1}, which represented improvements compared to the pristine materials, which had an overpotential of 270 mV and the same Tafel slope of 78 mV dec^{-1}. The sample's morphology, along with increased metal–F ionicity and chemical bond polarity, contributed to the improved the OER activities.[197]

6. Fluorinated carbides, nitrides, phosphides and sulfides

Fluorinated carbides, nitrides, phosphides and sulfides have been reported for the OER, and their representative OER activities are listed in Table 8.

6.1 F-doped carbides

Transition-metal carbides have demonstrated appealing properties, including high conductivity, chemical stability, thermal stability, and mechanical strength, making them potential

Table 8 Representative OER performance of F-doped nitride, phosphide, and sulfide catalysts[a]

Catalyst	Overpotential at specific current density	Tafel slope (mV dec^{-1})	Tested durability	Electrolyte	Source
F-doped carbides					
$TiTaF_xC_2$ NP/rGO	280 mV@10 mA cm^{-2}	36	40 h@1.6 V	1 M $HClO_4$	198
$TiTaC_2$ NP/rGO	420 mV@10 mA cm^{-2}	106	—	1 M $HClO_4$	
F-doped nitrides					
PF/$Ni_{1.5}Co_{1.5}N$	280 mV@10 mA cm^{-2}	66.1	20 h@10 mA cm^{-2*}	1 M KOH	199
$Ni_{1.5}Co_{1.5}N$	350 mV@10 mA cm^{-2}	78.6	—	1 M KOH	
F-doped phosphides					
F-CoP NAs/CF	231 mV@50 mA cm^{-2}	73.19	100 h@50 mA cm^{-2}	1 M KOH	37
CoP Nas/CF	378 mV@50 mA cm^{-2}	147.26	—		
Ni_2P:5F	230 mV@50 mA cm^{-2}	28.06	24 h@1.55 V (95% retention)	1 M KOH	36
Ni_2P	370 mV@50 mA cm^{-2}	37.43	24 h@1.55 V (50% retention)	1 M KOH	
F-Co_2P/NF	307 mV@50 mA cm^{-2}	120	50 h@500–1000 mA cm^{-2}	1 M KOH	200
Co_2P/NF	338 mV@50 mA cm^{-2}	123	—		
F-NC2AL@ZFAL/NF	177 mV@10 mA cm^{-2}	67	20 h@10 mA cm^{-2}	1 M KOH	201
Zn/F-NiCoP/NF	285 mV@50 mA cm^{-2}	78.33	40 h@10 mA cm^{-2}	1 M KOH	202
Zn-NiCoP/NF	331 mV@50 mA cm^{-2}	102.84	—	1 M KOH	
F-$FeCoP_V$@IF	370 mV@1000 mA cm^{-2}	118	20 h@100 mA cm^{-2}	1 M KOH + sea water	203
Ni_2P-F3	261 mV@50 mA cm^{-2}	52.1	24 h@50 mA cm^{-2}	1 M KOH	204
Ni_2P	412 mV@100 mA cm^{-2}	168.8			
F-doped sulfides					
$Ni(OH)_2$/F-Ni_3S_2/NF (FN-20)	360 mV@100 mA cm^{-2}	126	20 h@1.7 V (94.9% retention)	1 M KOH	205
Pristine Ni_3S_2	580 mV@100 mA cm^{-2}	211	20 h@1.7 V (20.9% retention)		
F-Ni_3S_2/NF	358 mV@10 mA cm^{-2}	—	30 h@1.6 V	1 M KOH	206
Fe–CoS_2–F	298 mV@10 mA cm^{-2}	46.0	100 h@1.53 V	1 M KOH	207
Fe–CoS_2	345 mV@10 mA cm^{-2}	64.2	—	1 M KOH	
CoS_2–F	350 mV@10 mA cm^{-2}	107.6	—	1 M KOH	
CoS_2	363 mV@10 mA cm^{-2}	110.9	—	1 M KOH	
F-NiP_x/Ni_3S_2-NF	370 mV@100 mA cm^{-2}	92	24 h@1.55 V	1 M KOH	208
NiP_x/Ni_3S_2-NF	420 mV@100 mA cm^{-2}	108	—	1 M KOH	

[a] (*) Estimated in this study.

candidates for catalyst applications.[209–213] However, their OER catalytic activities are generally considered low, even in alkaline media.[214–216]

Since monometallic carbides exhibit negligible OER activities in the acidic medium, Feng *et al.* reported bimetallic carbides ($TiTaC_2$) doped with F.[198] As illustrated in Fig. 13a, starting from precursors K_2TaF_7 and K_2TiF_6, a hydrothermal treatment yields fluoride K_2MF_x on reduced graphene oxide (rGO). Further annealing at an intermediate temperature of 1100 °C produces oxyfluorides TaO_2F and TiOF on rGO, whereas at a higher temperature of 1200 °C, F-doped carbide $TiTaF_xC_2$ is formed on rGO. The $TiTaF_xC_2$ nanoparticles range in size from 20 to 50 nm. The $TiTaF_xC_2$ NP/rGO catalyst exhibits an overpotential of 280 mV at 10 mA cm^{-2}, significantly lower than non-doped $TiTaC_2$ NP/rGO, which has an overpotential of 420 mV. The Tafel slope is also significantly reduced from 106 to 36 mV dec^{-1} (Table 8). DFT studies indicate that the F dopant lowers the activation energy in the RDS by functioning as an electron acceptor in $TiTaF_xC_2$. This process involves charge transfer from the metal and adjacent carbon atoms to fluorine (Fig. 13b). The resulting charge redistribution enhances Ti's adsorption properties, strengthening the bonding of crucial intermediates on $TiTaF_xC_2$ and promoting the oxygen evolution reaction (OER) under acidic conditions.

Additionally, tantalum carbide doped with F and partially oxidized to $TaC_xF_yO_z$ was prepared on graphitized carbon.[217] The synthesis process involving K_2TaF_7 as a precursor initially yielded TaO_2F, which subsequently transformed into $TaC_xF_yO_z$ following high-temperature treatment in a nitrogen atmosphere. This resulting material exhibited remarkable electrocatalytic properties for oxidizing methanol in an acidic environment.

6.2 F-doped nitrides

Compounds formed by combining transition metals with nitrogen, known as transition-metal nitrides (TMNs), are characterized by their remarkably high melting temperatures, superior mechanical attributes, exceptional electrical conduction properties, and robust structural integrity.[218] In fact, TMNs exhibit surface and adsorption properties similar to those of noble metals because nitrogen atoms can modulate their electronic and geometric structures.[219,220] TMNs have shown promising electrocatalytic activities in the OER.[221,222]

Bimetallic Ni–Co nitride is an effective OER catalyst.[223] Bai *et al.* codoped P and F into bimetallic nitride $Ni_{1.5}Co_{1.5}N$

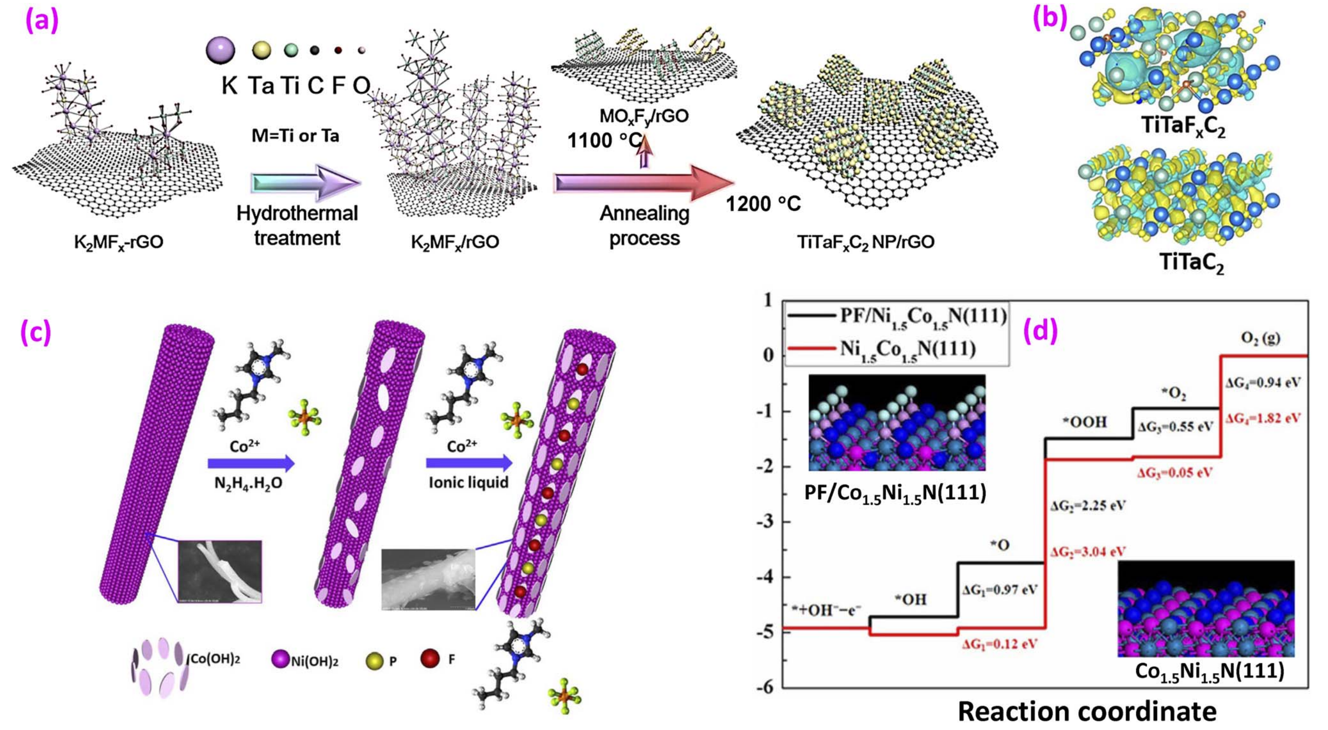

Fig. 13 (a) Synthesis of fluorinated metal carbide and (b) DFT-calculated charge density distribution. Reproduced from ref. 198 with permission from American Chemical Society, copyright 2022. (c) Synthesis of Co-based nitride catalysts and (d) DFT calculation of Gibbs free energy, with insets of P and F doped $Co_{1.5}Ni_{1.5}N$ (111) structural models. Reproduced from ref. 199 with permission from John Wiley and Sons, copyright 2017.

mesoporous nanorods by using an ionic liquid method (Fig. 13c).[199] The doped material exhibited better OER activity than the undoped version (Table 8). Gibbs free energy calculations using DFT, shown in Fig. 13d, reveal that the largest free energy difference occurs in the second step of the OER process, which has the highest ΔG_2 for both doped and undoped materials. However, the doped material, with $\Delta G_2 = 2.25$ eV, has a lower energy barrier compared to the undoped material, with $\Delta G_2 = 3.04$ eV, indicating that less overpotential is required for the doped materials.

Initially, it was believed that single-phase graphitic carbon nitride (g-C_3N_4) lacked the ability to perform photocatalytic overall water splitting, primarily due to its inadequate oxygen evolution reaction (OER) capabilities.[224] Nevertheless, *in situ* observation revealed that when using a fluorinated carbon nitride (F_x-CN) catalyst synthesized through hydrothermal treatment, the fluorination process inhibits the buildup of C=O by creating CF bonds on the surface.[225] In single-phased g-C_3N_4, the robust binding of intermediate C=O presents a significant challenge for overall water splitting. DFT calculations indicate an enhanced OER pathway on adjacent nitrogen atoms through C–F interactions, which reduce the energy barriers associated with the OER.

6.3 F-doped phosphides

Due to their distinctive electronic structure and high catalytic performance, transition-metal phosphides (TMPs) have emerged as promising catalysts for the OER.[226,227] However, the intrinsic activity and durability of pristine TMPs are limited. Research on F-doped phosphide CoP has demonstrated significantly improved OER performance, reducing the overpotential of undoped CoP from 378 to 285 mV at 10 mA cm^{-2} and lowering the Tafel slop from 147.26 to 73.19 mV dec^{-1}.[37] Fluorination creates phosphorus vacancies (P_V), leading to increased active sites and regulation of charge distribution, which enhances the OER. A molten salt and gas-phase phosphorization method was used to synthesize F-doped FeCoP nanosheets with P_V.[203] As shown in Fig. 14a, a piece of 3D iron foam (IF) is used as the substrate, and FeCoO@IF nanosheets are first grown *in situ* using a molten salt mixture of cobalt nitrate and NH_4F. Afterward, phosphorization is conducted in an inert atmosphere to obtain the final product, F-FeCoP$_V$@IF. A SEM image in Fig. 14b shows the layered structure of the material. The synthesized catalyst was used for seawater splitting (Fig. 14c), and the obtained H_2/O_2 volume ratio was 2 : 1, indicating a faradaic efficiency of 100% in the 1.0 M KOH with seawater solution (Fig. 14d).

A two-step synthesis of cross-linked NiCoP nanosheets has been reported, as depicted in Fig. 14e.[201] The process began with the production of F-NiCo$_2$Al-LDH/NF, which was subsequently phosphatized to yield NiCoAlP/NF. This was followed by an acid wash to eliminate Al species. As depicted in Fig. 14f and g, the resulting nanosheets grow perpendicular to the NF surface, creating an interconnected porous network structure. Such a structure favors charge/electron transfer for the OER. The overpotential reached as low as 177 mV for a current density of 10 mA cm^{-2}.

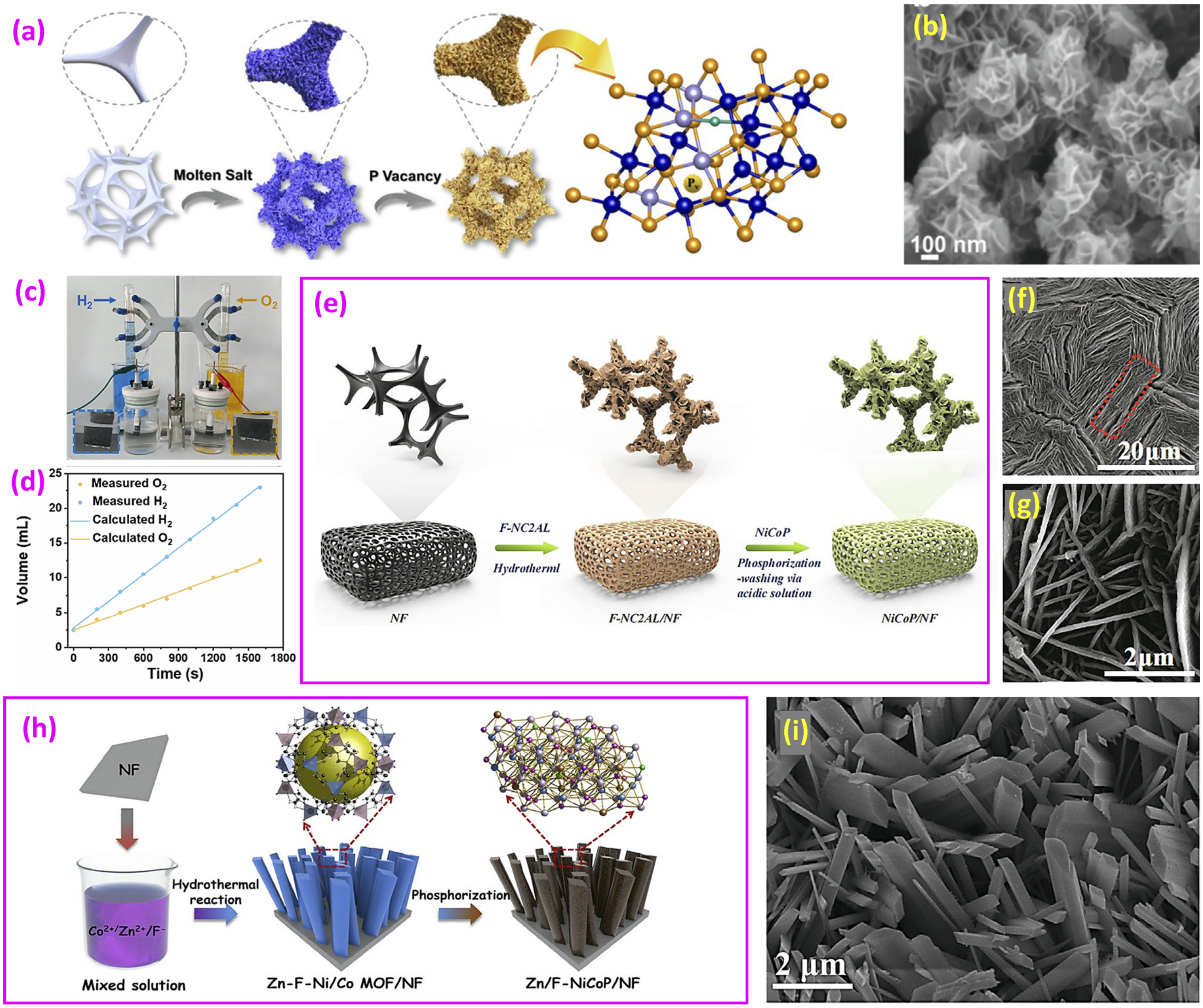

Fig. 14 (a) Synthesis procedure for F-FeCoP$_v$@IF; (b) SEM image of F-FeCoP$_v$@IF; (c) photographs of a homemade two-electrode cell; and (d) photographs of gases produced at the anode and cathode at different times. Reproduced from ref. 203 with permission from Elsevier, copyright 2023. (e) Synthesis route for NiCoP/NF and (f and g) SEM images of NiCoP. Reproduced from ref. 201 with permission from Elsevier, copyright 2022. (h) Synthesis of Zn/F-NiCoP/NF and (i) SEM of Zn/F-NiCoP/NF. Reproduced from ref. 202 with permission from Elsevier, copyright 2023.

Recently, Zn/F-doped NiCo-MOFs were synthesized on NF *via* a hydrothermal reaction, followed by phosphorization to obtain Zn/F-doped NiCoP (Fig. 14h).[202] The NiCo-MOF template appears as nanoprisms (Fig. 14i). The Zn/F co-doped NiCoP exhibited better activity than single-doped or RuO_2 on NF. DFT calculations reveal that Zn and F codoping optimizes the adsorption energy of active sites for reactants and intermediates, enhancing the catalytic performance. Similarly prepared F-doped CoP/Ni_2P nanowires were also studied for the HER.[228]

6.4 Fluorinated sulfides

Transition-metal sulfides (TMSs) have emerged as promising electrocatalysts for the OER, owing to their superior electrical conductivity and inherent catalytic activity.[229] F-doped TMSs have been reported for the OER. Using Ni foam, and Na_2S and NH_4F solutions in a hydrothermal reaction, structural evolution was observed in the synthesis of heteronanorods, as shown in Fig. 15a.[205] This process involved the formation of $Ni(OH)_2$ nanosheets after 1 h, the formation of F–Ni_3S_2 nanorods on $Ni(OH)_2$ nanosheets after 5 h, and finally the development of $Ni(OH)_2$ nanosheets/F–Ni_3S_2 heteronanorods on nickel foam. The catalyst required a low overpotential of 360 mV to reach 100 mA cm^{-2}. DFT calculations revealed that the incorporation of F modulated the electron density at the Fermi level of Ni_3S_2, contributing to elevated electrical conductivity and charge transfer efficiency.

A method to prepare Fe and F dual-doped CoS_2 nanospheres (Fe–CoS_2–F) was also reported.[207] Fig. 15b illustrates the process of creating Fe and F dual-doped hollow spheres. Initially, Co-glycerate nanospheres are synthesized. These solid spheres undergo a transformation into bimetallic CoFe-PBA hollow spheres through a room-temperature wet–chemical reaction lasting 24 h, utilizing $K_3[Fe(CN)_6]$ and sodium citrate.

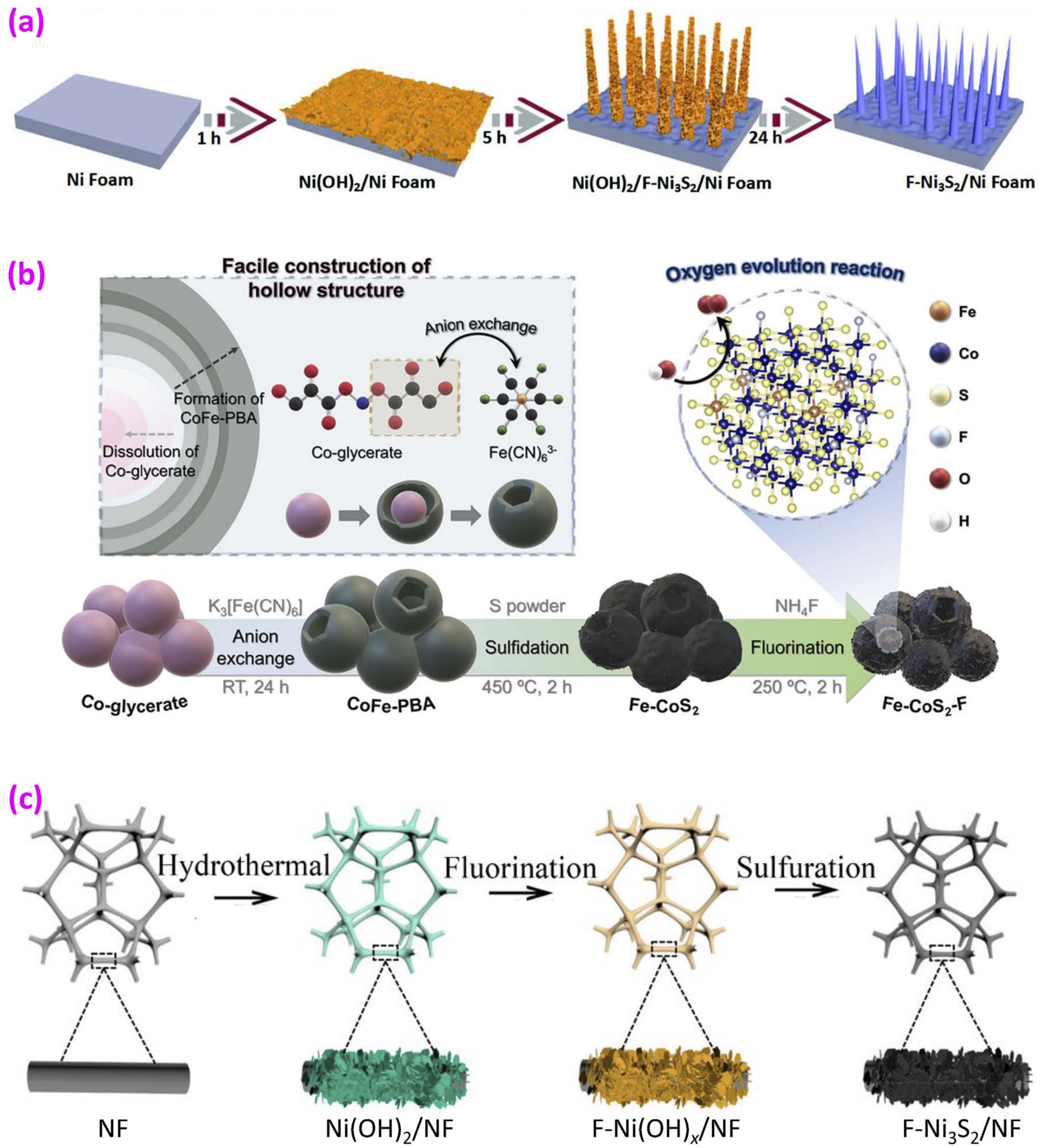

Fig. 15 (a) Synthesis of the fabrication process of $Ni(OH)_2$ nanosheets/F-doped Ni_3S_2 heteronanorods. Reproduced from ref. 205 with permission from the Royal Society of Chemistry, copyright 2018. (b) Synthesis of Fe and F dual-doped CoS_2 hollow spheres using self-sacrificial templates. Reproduced from ref. 207 with permission from Elsevier, copyright 2024. (c) Synthesis of F–Ni_3S_2/NF. Reproduced from ref. 206 with permission from American Chemical Society, copyright 2019.

Subsequently, CoFe-PBA is heat-treated with sulfur powder in an Ar environment, resulting in Fe-doped CoS_2 hollow spheres (Fe–CoS_2). The final step involves fluorination using NH_4F, yielding Fe and F dual-doped hollow spheres (Fe–CoS_2–F). The sample with dual doping demonstrated the most excellent hydrophilicity and surface wettability, as evidenced by the smallest contact angle (10.8°) of a water droplet, which is beneficial for the OER. Compared to single-doped or undoped samples, the dual-doped sample displayed the most favorable overpotential and Tafel values (Table 8). According to DFT calculations, the presence of dual dopants mitigates the excessively strong adsorption energy of reaction intermediates in the rate-determining steps, thereby improving OER performance.

In addition, F-doped Ni_3S_2 nanosheets have been reported, and the synthesis is depicted in Fig. 15c.[206] The synthesis of F–Ni_3S_2 nanosheets on NF involved a multi-step process. Initially, $Ni(OH)_2$ nanosheets were created on NF through hydrothermal synthesis. This was followed by a fluorination step to produce F–$Ni(OH)_x$. The final stage involved hydrothermal sulfuration, resulting in F–Ni_3S_2 nanosheets on NF. Although F–Ni_3S_2/NF demonstrated superior HER performance, its OER capabilities were found to be suboptimal.

7. F-doped carbon-based catalysts

Nanocarbon materials possess exceptional properties, including superior electrical conductance, enhanced surface area, adjustable structural organization, extremely thin graphite-like layers, and characteristics associated with low dimensionality.[230] These unique features make nanocarbons highly versatile for use in catalysts. However, carbon itself is generally inert for most electrochemical reactions, so surface or subsurface modifications are required to increase the binding energies of reactants and reaction intermediates on carbon.[231] Carbon-based catalysts have been used for the OER, including both carbon catalysts and carbon hybrid catalysts.[230–232]

7.1 F-doped carbon catalysts

The representative OER performances of F-doped carbon catalysts are listed in Table 9. Doped nanocarbon sheets have been used for the OER. Zhang and Dai doped graphene with N, P and F, as shown in Fig. 16a.[233] The process began with the polymerization of graphene oxide (GO) to create GO coated with polyaniline (PANi), resulting in GO-PANi. Subsequently, this compound underwent pyrolysis in the presence of NH_4FPF_6, yielding a tri-doped material known as GO-PANI-FP, which incorporated fluorine, phosphorus, and nitrogen. SEM observations display a highly porous layered structure, as shown in Fig. 16b. This catalyst outperforms the RuO_2 catalyst. Kim *et al.* found that F-doped carbon catalysts could enhance OER activity.[235,237] Sim *et al.* synthesized N and F codoped graphene quantum dots (GQDs) (Fig. 16c and d), which showed an overpotential of 408 mV@10 mA cm^{-2}, while a single N-doped GQD sample exhibited 425 mV and an undoped GQD sample showed 447 mV overpotentials.[238] The F–C bonding enhances the OER performance of the GQDs. In another study, N and F codoped porous graphene nanosheets (NFPGNSs) demonstrated improved OER compared to N single-doped nano-graphene (NNG),[234] as listed in Table 9.

Another form of carbon, graphdiyne (GDY), a new carbon allotrope containing both sp- and sp^2-hybridized carbon atoms, has been fluorinated for the OER.[236] Its uneven surface charge distribution results in various active sites. The synthesis of 3D hierarchical porous fluorographdiyne networks on carbon cloth (p-FGDY/CC) was accomplished (Fig. 16e). The catalyst demonstrated exceptional performance in catalyzing the OER, the HER, and overall water splitting (OWS) reactions, showing remarkable durability across a broad spectrum of pH conditions, ranging from acidic to basic environments.

Carbon nanotubes (CNTs) can be functionalized with several dopants,[244] and F doping has also been found to enhance the OER performance of CNTs.[239] F-doped CNTs required only 280 mV to maintain 10 mA cm^{-2} current, while pristine CNTs required 340 mV (Fig. 16f). The F-doped CNTs also showed a lower Tafel slope. Surface modification using the more electronegative fluorine atoms created semi-ionic C–F and covalent C–F active sites, which improved OER efficiency.

Recently, Muthurasu *et al.* synthesized N, B and F tri-doped chain-like porous carbon nanofibers (PCNFs) using an electrospinning method, followed by stabilization (280 °C) and carbonization (1200 °C) in a furnace, as shown in Fig. 16g.[242] The codoping enhanced the OER performance, surpassing that of the RuO_2 catalyst.

7.2 F-doped carbon hybrid catalysts

Integrating TMs or TM compounds with carbon as hybrid catalysts can significantly enhance OER performance.[245–247] The representative OER performance of F-doped TM/carbon hybrid catalysts are listed in Table 10. Fluorinated TM compounds combined with porous carbon forms, such as nanofibers,[248] carbon encapsulated layers,[249–251,255] graphene sheets,[252,254,257,259]

Table 9 Representative OER performance of F-doped carbon catalysts[a]

Catalyst	Overpotential at specific current density	Tafel slope (mV dec^{-1})	Tested durability	Electrolyte	Source
GO-PANi31-FP	460 mV@3 mA cm^{-2*}	136	10 h@10 mA cm^{-2}	0.1 M KOH	233
GO-PANi-950	630 mV@3 mA cm^{-2*}	221	—		
NFPGNS	340 mV@3 mA cm^{-2*}	78	—	1 M KOH	234
NNG	490 mV@3 mA cm^{-2*}	109	—	1 M KOH	
F-doped carbon black	150 mV@0.5 mA cm^{-2*}	—	—	0.1 M KOH	235
Carbon black	270 mV@0.5 mA cm^{-2*}	—	—	0.1 M KOH	
p-FGDY/CC	460 mV@10 mA cm^{-2}	128	9 h@10 mA cm^{-2}	1.0 M KOH	236
F-doped carbon	—	183	—	1 M KOH (pH = 14)	237
N,F-GQDs	408 mV@10 mA cm^{-2}	—	22 h@1.6 V	1 M KOH	238
N-DQDs	425 mV@10 mA cm^{-2*}	—	—	1 M KOH	
GQDs	447 mV@10 mA cm^{-2*}	—	—	1 M KOH	
F-doped CNTs	280 mV@10 mA cm^{-2}	76	10 h@15 mA cm^{-2}	1 M KOH	239
Pristine CNTs	340 mV@10 mA cm^{-2}	75	—	1 M KOH	
C-NBF-G	333 mV@10 mA cm^{-2}	114	—	0.1 M KOH	240
FCl-CQDs/VG	393 mV@10 mA cm^{-2}	296	10 h@1.5 V	1 M KOH	241
N, B, and F doped PCNFs	280 mV@10 mA cm^{-2}	83	50 h@10 mA cm^{-2}	1 M KOH	242
PCFN-800	280 mV@10 mA cm^{-2}	43	—	1 M KOH	243

[a] (*) Estimated in this study.

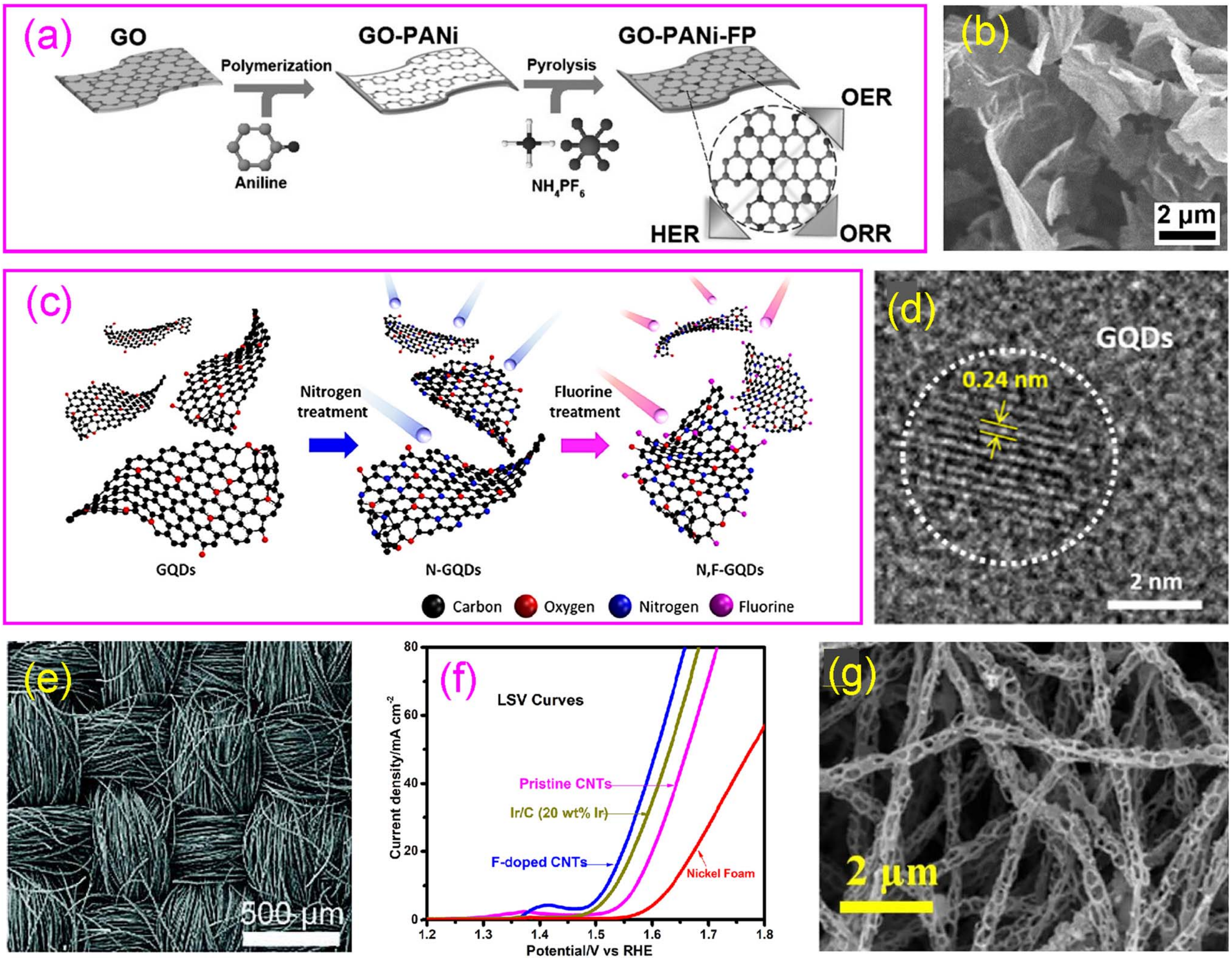

Fig. 16 F-doped carbon catalysts for the OER. (a) Preparation process of a GO-PANi-FP tri-functional catalyst and (b) SEM image of GO-PANi-FP. Reproduced from ref. 233 with permission from John Wiley and Sons, copyright 2016. (c) Synthesis of N and F codoped GQDs and (d) TEM image of a GQD. Reproduced from ref. 238 with permission from Elsevier, copyright 2020. (e) Photograph of porous fluorographdiyne networks on a carbon cloth p-FGDY/CC material. Reproduced from ref. 236 with permission from John Wiley and Sons, copyright 2019. (f) LSV plots of CNTs. Reproduced from ref. 239 with permission from Springer Nature, copyright 2021. (g) SEM of chain-like porous nanofibers. Reproduced from ref. 242 with permission from the Royal Society of Chemistry, copyright 2024.

graphene quantum dots,[256] carbon nanotubes,[253] and nanocellulose-cornstalk aerogels,[258] have been used for the OER.

Fluorination of N-doped porous nanofibers synthesized by electrospinning resulted in FeF_2, NiF_2, Ni_3Fe and possibly oxides encapsulated with nanocarbon layers.[248] Such hybrid catalysts exhibit high OER performances, due to the large surface area and roughness of the nanofibers. As illustrated in Fig. 17a, the selective fluorination of $FeNi_3$ alloy oxides (NiO and Fe_3O_4) within N-doped porous carbon nanofibers (NiFeO/NCF) resulted in the formation of fluorides (NiF_2 and FeF_2) embedded in N-doped porous carbon nanofibers (FeNiF/NCF).[248] The oxide catalyst exhibited an overpotential of 330 mV for 10 mA cm^{-2}, which was reduced to 260 mV after fluorination. The Tafel slope was also reduced from 90 to 67 mV dec^{-1}.

A catalyst of carbon-confined iron–nickel alloy/iron fluoride doped with oxygen (C/O–FeNi/FeF_2) is presented in Fig. 17b.[251] The nanoparticles are O-doped FeNi and FeF_2, embedded in carbon nanolayers, as revealed by elemental mapping on the right side of Fig. 17b. This catalyst exhibited a low overpotential of 253 mV to reach 10 mA cm^{-2} which is even lower than that of IrO_2. ZIF-67 was used as a template to develop an Fe, N and F co-doped porous carbon catalyst, as shown in Fig. 17c.[255] The catalyst was evaluated for both the ORR and OER, showing promise as a ZIF-derived bifunctional non-precious metal catalyst. N-doped CNTs were used to connect the CoFe binary alloy and fluoride nanoparticles, as shown in Fig. 17d.[253] This setup achieved a low overpotential of 231 mV to drive 10 mA cm^{-2}, while RuO_2 required an overpotential of 325 mV to reach the same current density.

In WO_3-decorated F-doped graphite sheets, F doping reduced the overpotential largely by 95 mV and Tafel slope by 39 mV dec^{-1}.[252] DFT calculations revealed that the determining step is the deprotonation of surface-adsorbed OH, and the F-GS sample required the lowest overpotential, as shown in Fig. 17e.

Table 10 Representative OER performance of F-doped carbon hybrid catalysts[a]

Catalyst	Overpotential at specific current density	Tafel slope (mV dec^{-1})	Tested durability	Electrolyte	Source
FeNiF/NCF	260 mV@10 mA cm^{-2}	67	10 h@10 mA cm^{-2}	1 M KOH	248
FeNiO/NCF	330 mV@10 mA cm^{-2}	90	—		
CoF_2/NC	294 mV@10 mA cm^{-2}	70.0	10 h@1.52 V	1 M KOH	249
FeNi@NC-1-8-F	242 mV@10 mA cm^{-2}	45.24	12 h@10–40 mA cm^{-2}	1 M KOH	250
FeNi@NC-1-8	275 mV@10 mA cm^{-2}	55.2	—		
C/O-FeNi/FeF_2	253 mV@10 mA cm^{-2}	52	16 h@10–20 mA cm^{-2}	1 M KOH	251
WO_3@$F_{0.1}$-GS	298 mV@10 mA cm^{-2}	77.6	24 h@10 mA cm^{-2}	1 M KOH	252
WO_3@GS	393 mV@10 mA cm^{-2}	116.6	Unstable	1 M KOH	
CoFe@NCNTs-700-F-300	231 mV@10 mA cm^{-2}	45.9	20 h@15 mA cm^{-2*}	1 M KOH	253
CoFe@NCNTs-700	290 mV@10 mA cm^{-2}	56.0	—		
N,F-$Co(OH)_2$/GO	228 mV@10 mA cm^{-2}	52.6	30 h@10 mA cm^{-2}	1 M KOH	254
$Co(OH)_2$/GO	325 mV@10 mA cm^{-2}	72.1	—	1 M KOH	
F-N/$FeCoNC_{900}$	273 mV@10 mA cm^{-2}	52.8	—	1.0 M KOH	255
GQD/F-NiF PBA	318 mV@50 mA cm^{-2}	34.7	30 h@100 mA cm^{-2}	1.0 M KOH	256
GQD/NiF PBA	339 mV@50 mA cm^{-2}	41.79	—		
CoFeF-rGO	245 mV@10 mA cm^{-2}	90	10 h@1.475 V	1 M KOH	257
CoFeO-rGO	430 mV@10 mA cm^{-2*}	113	—	1 M KOH	
N,B,F@Co-CNF	368 mV@10 mA cm^{-2}	94.88	—	1 M KOH	258
CoFeNiF-rGAs	238 mV@10 mA cm^{-2}	78.8	20 h@10 mA cm^{-2}	1 M KOH	259
Fe_2Ni@NC-C-F	247 mV@10 mA cm^{-2}	44.81	60 h@10 mA cm^{-2}	1 M KOH	260
Fe_2Ni@NC-C	314 mV@10 mA cm^{-2}	71.33	—	1 M KOH	
Fe_2Ni–C–F	287 mV@10 mA cm^{-2}	61.83	—	1 M KOH	
Fe_2Ni–C	337 mV@10 mA cm^{-2}	70.82	—	1 M KOH	
AlF_3@HPCNFs-3	310 mV@10 mA cm^{-2}	121	—	1 M KOH	45
PCNFs	520 mV@10 mA cm^{-2}	405	—		
(MnNiCuCoZn)F_2-PCNFs	310 mV@10 mA cm^{-2}	88.2	5.56 h with 94% retention	1 M KOH	261

[a] (*) Estimated in this study.

Functionalized fluorographene[262] could improve the OER performance of CoN_4.[263] F-doped graphene oxide was also used to enhance the OER.[254] N, F-doped $Co(OH)_2$/GO showed an overpotential of 228 mV for 10 mA cm^{-2} and a Tafel slope of 52.6 mV dec^{-1}, whereas the undoped version had an potential of 370 mV and a Tafel slope 75.9 mV dec^{-1}. The presence of highly electronegative fluorine in graphene oxide stabilized the Co^{2+} active site, enhancing the transfer of charge and adsorption processes. This resulted in improved performance of the oxygen evolution reaction (OER).[254]

Yu and coworkers added graphene oxide in a hydrothermal synthesis and obtained Co–Fe fluorides on graphene.[257] The fluorides, composed of FeF_2 and CoF_2, were in nanosheet shape. This catalyst exhibited an overpotential of 245 mV for 10 mA cm^{-2}. The same group also reported tri-metallic fluorides Co–Fe–Ni–F on reduced graphene architecture (rGA), as illustrated in Fig. 17f.[259] The fluorides were identified as CoF_2 and NiF_2 in nanosheet form, as shown in Fig. 17g. This catalyst showed an overpotential of 238 mV for 10 mA cm^{-2}. DFT analysis showed that the Co–Fe–Ni–F-rGA trimetallic compound exhibits enhanced electronic states close to the Fermi level, leading to superior conductivity and an elevated d-band center ε_d, which promotes better adsorption.

Recently, high-entropy fluoride (MnNiCuCoZn)F_2 nanoparticles were synthesized in porous carbon nanofibers (PCNFs), as shown in the TEM image in Fig. 17h.[261] The approach leveraged the active sites provided by the HEF and exploited the Zn component's ability to convert HEF nanoparticles from single-crystals to polycrystals, effectively enhancing electrocatalytically active sites. The (MnNiCuCoZn)F_2-PCNFs catalyst exhibited exceptional performance in both OER and ORR processes.

8. Summary and concluding remarks

In this review article, we summarize the synthesis, structure, and OER performance of state-of-the-art fluorinated catalysts for the OER, including (1) transition-metal fluorides with binary, ternary, quaternary, and high-entropy systems; (2) fluoride-oxide catalysts of oxyfluorides, fluorinated oxides, and fluoride/oxide heterocatalysts; (3) fluorinated hydroxides, oxyhydroxides and carbonate hydroxides and their derived fluorides; (4) fluorinated carbides, nitrides, phosphides and sulfides; and (5) fluorinated carbon and carbon hybrid catalysts. Fluorine's exceptional electronegativity, the highest among all elements, leads to metal–fluorine bonds that are highly ionic. This characteristic allows these bonds to be readily broken down in electrolyte solutions, providing an inherent advantage for catalysts containing fluorine in the OER.

This review details the OER performances of various fluorinated catalysts, emphasizing the unique role of fluorine in enhancing OER activity. The application of pure transition-metal fluorides in the OER is constrained by their poor electrical conductivity. However, incorporating heteroatomic

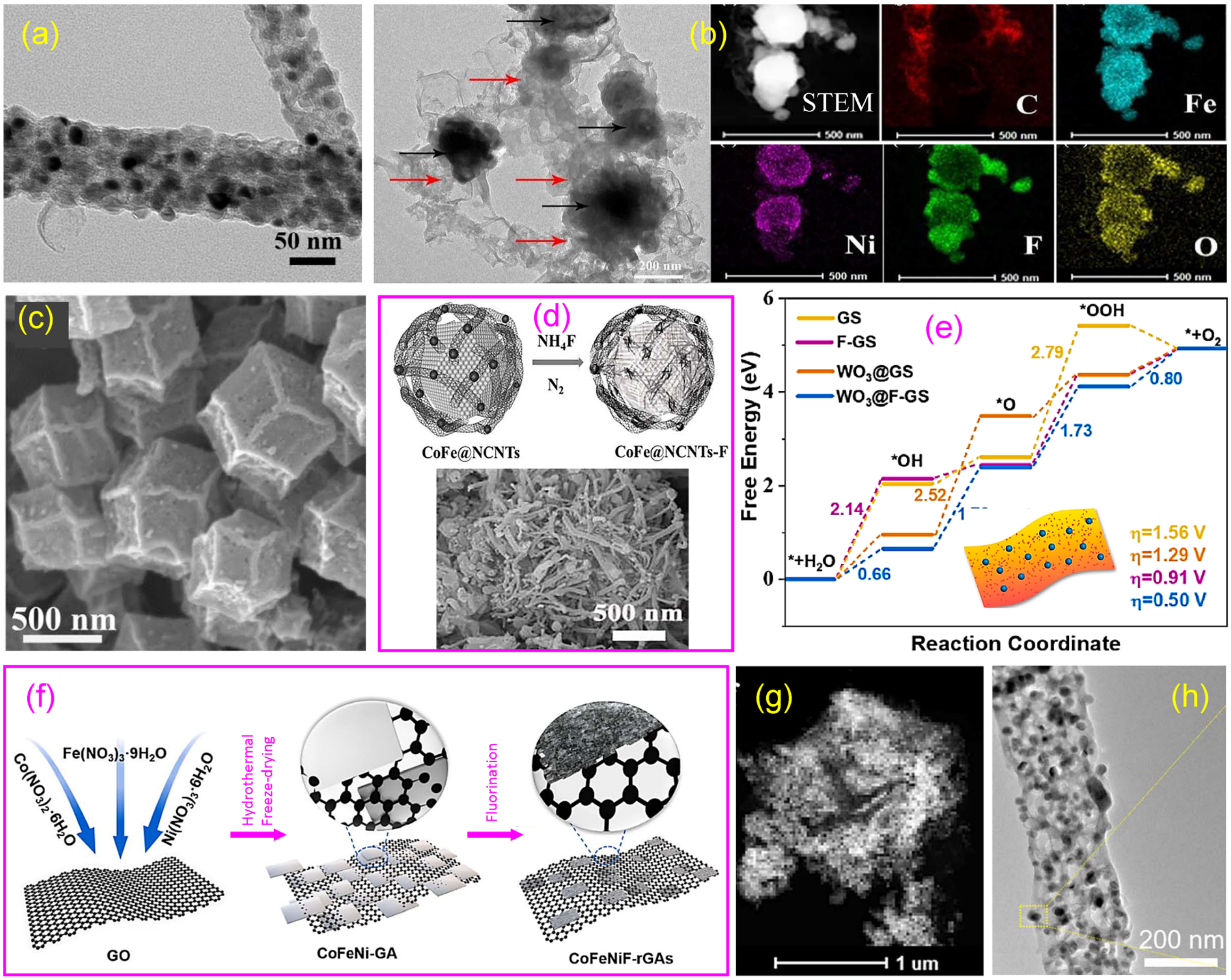

Fig. 17 F-doped carbon hybrid catalysts for the OER. (a) TEM image of FeNiF/NCF. Reproduced from ref. 248 with permission from Elsevier, copyright 2020. (b) TEM image (left) and elemental maps (right) of C/O–FeNi/FeF_2. Reproduced from ref. 251 with permission from Elsevier, copyright 2022. (c) SEM image of F-N/FeCoNC_{900} derived from ZIF-67. Reproduced from ref. 255 with permission from Elsevier, copyright 2023. (d) Synthesis of Co-Fe-F/CNT with an inset of the SEM image of CoFe@NCNT. Reproduced from ref. 253 with permission from Elsevier, copyright 2023. (e) Gibbs free energy calculation of WO_3 nanoparticles on F-doped graphite sheets. Reproduced from ref. 252 with permission from Elsevier, copyright 2023. (f) Synthesis of CoFeNiF-rGAs and (g) TEM image. Reproduced from ref. 259 with permission from Elsevier, copyright 2024. (h) TEM image of (MnNiCuCoZn)F_2 nanoparticles in porous carbon nanofibers. Reproduced from ref. 261 with permission from the Royal Society of Chemistry, copyright 2024.

dopants can enhance OER performance by improving electrical conductivity and structural stability. This doping approach has been successfully implemented in both binary and ternary systems. Furthermore, researchers have developed high-entropy fluoride catalysts that exhibit increased structural stability. Oxides, known for their prolonged stability, can benefit from fluorination, which may improve conductivity and lower energy barriers for electron transfer. Hydroxides and related catalysts exhibit superior OER performance due to their unique open surface structures, where fluorine can further facilitate surface reconstruction, enhancing OER activity. Additionally, fluorinated carbides, nitrides, phosphides, and sulfides have shown improved electrical conductivity, contributing to OER enhancement. Carbon-based catalysts hold high potential for OER applications owing to their large surface areas and efficient electron mobility, and their hybrid materials offer synergistic improvements in OER performance.

The fluorination of existing OER catalysts has been explored across a wide range of materials, with various fluorination methods introduced for each type of catalyst. In catalyst synthesis for the OER, creating highly porous nanostructures with accessible surface areas and active sites is essential. Fluorinated catalysts offer a notable advantage through their capacity for surface reconstruction, as evidenced by the examples in this study. As a result, fluorination emerges as a promising approach to enhance catalyst efficiency, and its potential for further improvements should be explored in OER catalyst development. Based on existing research data, fluorination has been shown to decrease the overpotential by an average of 21.6% and reduce the Tafel slope by 29.6% across various catalysts. Enhancing their OER performance through fluorination might be worth exploring for newly developed OER catalysts, provided this approach has not been previously attempted.

In contrast to the well-researched oxide-based catalysts for the OER, studies on fluorides or fluorinated catalysts are scarce and demand an extensive investigation. Creating materials with multiple elements doping to boost OER performance is complex, requiring optimization and theoretical evaluation. The review presents numerous instances demonstrating that developing heterocatalysts, rather than single catalysts, is an effective approach to enhancing the OER. Improving structural stability and durability is essential for fluorides to produce highly stable and corrosion-resistant fluorinated catalysts for OER applications. Although most reported materials have been synthesized using wet chemistry techniques, scaling up for practical applications necessitates industrial-grade precursors. Prototype development in laboratory research for these applications is crucial and requires collaboration across disciplines.

Data availability

This review article is based entirely on publicly available data sourced from published literature. All the data analyzed in this paper are derived from previously published studies and can be accessed through the original publications. No new experimental data were generated or analyzed for this review. All relevant sources and references are provided in the article's reference section, and the full-text articles can be accessed through the respective journals or databases. Readers interested in specific datasets or studies referenced in this review can access them directly through the provided citations.

Conflicts of interest

There are no conflicts to declare.

Acknowledgements

This work was supported by the U.S. NSF PREM project, DMR-1827731. Some of the research facilities at the author's laboratory were funded by NSF grants ECCS-1900837 and EES-2106181. The author expresses gratitude to previous team members, Drs Gibin George and Sivasankara Rao Ede, for their valuable input and engaging discussions, as well as their assistance with technical matters.

References

1 S. Y. Tee, K. Y. Win, W. S. Teo, L.-D. Koh, S. Liu, C. P. Teng and M.-Y. Han, *Adv. Sci.*, 2017, **4**, 1600337.
2 A. Hayat, M. Sohail, H. Ali, T. A. Taha, H. I. A. Qazi, N. Ur Rahman, Z. Ajmal, A. Kalam, A. G. Al-Sehemi, S. Wageh, M. A. Amin, A. Palamanit, W. I. Nawawi, E. F. Newair and Y. Orooji, *Chem. Rec.*, 2023, **23**, e202200149.
3 N. Mlilo, J. Brown and T. Ahfock, *Technol. Econ. Smart Grids Sustain. Energy*, 2021, **6**, 25.
4 B. M. Hunter, H. B. Gray and A. M. Müller, *Chem. Rev.*, 2016, **116**, 14120–14136.
5 S. R. Ede and Z. Luo, *J. Mater. Chem. A*, 2021, **9**, 20131–20163.
6 S. Anantharaj, S. Kundu and S. Noda, *Nano Energy*, 2021, **80**, 105514.
7 F. Zeng, C. Mebrahtu, L. Liao, A. K. Beine and R. Palkovits, *J. Energy Chem.*, 2022, **69**, 301–329.
8 G. Dong, L. Yan and Y. Bi, *J. Mater. Chem. A*, 2023, **11**, 3888–3903.
9 Z. Liu, H. Liu, X. Gu and L. Feng, *Chem. Eng. J.*, 2020, **397**, 125500.
10 K. Lemoine, J. Lhoste, A. Hémon-Ribaud, N. Heidary, V. Maisonneuve, A. Guiet and N. Kornienko, *Chem. Sci.*, 2019, **10**, 9209–9218.
11 M. Li, H. Liu and L. Feng, *Electrochem. Commun.*, 2021, **122**, 106901.
12 Z. Zhang, Y. Zhu, Y. Zhong, W. Zhou and Z. Shao, *Adv. Energy Mater.*, 2017, **7**, 1700242.
13 P. Chen, T. Zhou, S. Wang, N. Zhang, Y. Tong, H. Ju, W. Chu, C. Wu and Y. Xie, *Angew. Chem., Int. Ed.*, 2018, **57**, 15471–15475.
14 W. Wang, Y. Yang, D. Huan, L. Wang, N. Shi, Y. Xie, C. Xia, R. Peng and Y. Lu, *J. Mater. Chem. A*, 2019, **7**, 12538–12546.
15 B. Zhang, K. Jiang, H. Wang and S. Hu, *Nano Lett.*, 2019, **19**, 530–537.
16 J. Zhang, Y. Ye, Z. Wang, Y. Xu, L. Gui, B. He and L. Zhao, *Adv. Sci.*, 2022, **9**, 2201916.
17 S. Guddehalli Chandrappa, P. Moni, D. Chen, G. Karkera, K. R. Prakasha, R. A. Caruso and A. S. Prakash, *ACS Appl. Energy Mater.*, 2021, **4**, 13425–13430.
18 Q. Dong, T. Su, W. Ge, Y. Ren, Y. Liu, W. Wang, Q. Wang and X. Dong, *Adv. Mater. Interfaces*, 2020, **7**, 1901939.
19 W. Li, A. Murisana, Q. Zhang, S. Wang and G. De, *Electrochem. Commun.*, 2022, **141**, 107363.
20 X. Fan, Y. Liu, S. Chen, J. Shi, J. Wang, A. Fan, W. Zan, S. Li, W. A. Goddard and X.-M. Zhang, *Nat. Commun.*, 2018, **9**, 1809.
21 E. A. Dawi, M. Padervand, S. Ghasemi, S. Hajiahmadi, K. Kakaei, Z. Shahsavari, S. Karima, M. Baghernejad, M. Signoretto, Z. H. Ibupoto, A. Tahira and C. Wang, *J. Water Process Eng.*, 2023, **54**, 103979.
22 J. Rossmeisl, Z.-W. Qu, H. Zhu, G.-J. Kroes and J. K. Nørskov, *J. Electroanal. Chem.*, 2007, **607**, 83–89.
23 Y. Peng, H. Hajiyani and R. Pentcheva, *ACS Catal.*, 2021, **11**, 5601–5613.
24 Q. Liang, G. Brocks and A. Bieberle-Hütter, *J. Phys.: Energy*, 2021, **3**, 026001.
25 Q. Ma and S. Mu, *Interdiscipl. Mater.*, 2023, **2**, 53–90.
26 X. Liu, Z. He, M. Ajmal, C. Shi, R. Gao, L. Pan, Z.-F. Huang, X. Zhang and J.-J. Zou, *Trans. Tianjin Univ.*, 2023, **29**, 247–253.
27 J. Li, W. Tian, Q. Li and S. Zhao, *ChemSusChem*, 2024, **17**, e202400239.
28 X. Ren, Y. Zhai, N. Yang, B. Wang and S. Frank) Liu, *Adv. Funct. Mater.*, 2024, **34**, 2401610.

29 Z. Li, P. Wei and G. Wang, *Energy Fuels*, 2022, **36**, 11724–11744.

30 Y. Liu, X. Liang, H. Chen, R. Gao, L. Shi, L. Yang and X. Zou, *Chin. J. Catal.*, 2021, **42**, 1054–1077.

31 Y. Tong, H. Mao, P. Chen, Q. Sun, F. Yan and F. Xi, *Chem. Commun.*, 2020, **56**, 4196–4199.

32 C. Wang, S. Wei, F. Li, X. Long, T. Wang, P. Wang, S. Li, J. Ma and J. Jin, *Nanoscale*, 2020, **12**, 3259–3266.

33 Q. Xu, M. Chu, M. Liu, J. Zhang, H. Jiang and C. Li, *Chem. Eng. J.*, 2021, **411**, 128488.

34 G. Li, Y. Gou, R. Ren, C. Xu, J. Qiao, W. Sun, Z. Wang and K. Sun, *Energy Mater. Adv.*, 2023, **4**, 0029.

35 F. Ma, Q. Wu, M. Liu, L. Zheng, F. Tong, Z. Wang, P. Wang, Y. Liu, H. Cheng, Y. Dai, Z. Zheng, Y. Fan and B. Huang, *ACS Appl. Mater. Interfaces*, 2021, **13**, 5142–5152.

36 S. D. Ghadge, O. I. Velikokhatnyi, M. K. Datta, K. Damodaran, P. M. Shanthi and P. N. Kumta, *J. Electrochem. Soc.*, 2021, **168**, 064512.

37 Y. Sun, W. Sun, L. Chen, A. Meng, G. Li, L. Wang, J. Huang, A. Song, Z. Zhang and Z. Li, *Nano Res.*, 2023, **16**, 228–238.

38 L. Gao, X. Cui, C. D. Sewell, J. Li and Z. Lin, *Chem. Soc. Rev.*, 2021, **50**, 8428–8469.

39 Y. Zeng, M. Zhao, Z. Huang, W. Zhu, J. Zheng, Q. Jiang, Z. Wang and H. Liang, *Adv. Energy Mater.*, 2022, **12**, 2201713.

40 H. Chai, P. Wang, T. Wang, L. Gao, F. Li and J. Jin, *ACS Appl. Mater. Interfaces*, 2021, **13**, 47572–47580.

41 Y.-N. Zhou, M.-X. Li, S.-Y. Dou, H.-Y. Wang, B. Dong, H.-J. Liu, H.-Y. Zhao, F.-L. Wang, J.-F. Yu and Y.-M. Chai, *ACS Appl. Mater. Interfaces*, 2021, **13**, 34438–34446.

42 Q. Xu, H. Jiang, X. Duan, Z. Jiang, Y. Hu, S. W. Boettcher, W. Zhang, S. Guo and C. Li, *Nano Lett.*, 2021, **21**, 492–499.

43 P. Ji, D. Zheng, H. Jin, D. Chen, X. Luo, J. Yang, Z. Wang and S. Mu, *Small Struct.*, 2023, **4**, 2300013.

44 J. Qian, Q. Shu, B. He, Y. Hua, X. Ge, D. Sun, W. Liu, Q. Zhang and L. Zhou, *Int. J. Hydrogen Energy*, 2024, **68**, 777–787.

45 Q. Zeng, N. Deng, G. Wang, Y. Feng, W. Kang and B. Cheng, *J. Colloid Interface Sci.*, 2024, **654**, 1063–1079.

46 Z. Xu, W. Zuo, Y. Yu, J. Liu, G. Cheng and P. Zhao, *Adv. Sci.*, 2024, **11**, 2306758.

47 J. Xie, R. Ding, Y. Li, J. Guo, Y. Zhang, Q. Fang, M. Yan, Y. He, Z. Yan, Z. Chen, X. Guo, Q. Yang, J. Luo, Y. Zhang, X. Sun and E. Liu, *Nano Energy*, 2024, **126**, 109669.

48 W. Liu, Q. Chen, Y. Shang, F. Liu, R. He, J. Zhang, Q. Li, H. Chai, Y. Tan and S.-J. Bao, *Adv. Funct. Mater.*, 2024, 2410325.

49 K. Zhang and R. Zou, *Small*, 2021, **17**, 2100129.

50 Y. Xue, Y. Wang, H. Liu, X. Yu, H. Xue and L. Feng, *Chem. Commun.*, 2018, **54**, 6204–6207.

51 H. Liu, M. Zha, Z. Liu, J. Tian, G. Hu and L. Feng, *Chem. Commun.*, 2020, **56**, 7889–7892.

52 X. Gu, Y.-G. Ji, J. Tian, X. Wu and L. Feng, *Chem. Eng. J.*, 2022, **427**, 131576.

53 J. Xu, M. Li, B. Dong and L. Feng, *Chin. Chem. Lett.*, 2023, 108798.

54 X. Han, L. Lin, C. Pei and X. Yu, *Energy Fuels*, 2022, **36**, 2123–2129.

55 W. Du, Y. Li, L. Zhang, J. Jiang, T. Zhao, T. Xie, Y. Yao, P. Li, Y. Feng and G. Xu, *ACS Appl. Nano Mater.*, 2023, **6**, 12754–12763.

56 Y. Zhang, B. Wang, C. Hu, M. Humayun, Y. Huang, Y. Cao, M. Negem, Y. Ding and C. Wang, *Chin. J. Struct. Chem.*, 2024, **43**, 100243.

57 C. Pei, H. Chen, B. Dong, X. Yu and L. Feng, *J. Power Sources*, 2019, **424**, 131–137.

58 Y. Li, G. Xu, J. Yang, J. Jiang, C. Wang and L. Zhang, *Appl. Surf. Sci.*, 2021, **566**, 150696.

59 R. Gao, B. Hu, Z. Fang, M. Deng, Y. Wu, Q. Yan, W. Yuan, D. Chen, W. Han and Z. Chen, *Catal. Commun.*, 2022, **169**, 106482.

60 S. E. Balaghi, S. Heidari, M. Benamara, H. Beyzavi and G. R. Patzke, *Int. J. Hydrogen Energy*, 2022, **47**, 1613–1623.

61 X. Gu, Z. Liu, H. Liu, C. Pei and L. Feng, *Chem. Eng. J.*, 2021, **403**, 126371.

62 Y. Du, G. Hao, T. Zhao, D. Li, G. Liu, D. Zhong, J. Li and Q. Zhao, *Chem. Commun.*, 2024, **60**, 4182–4185.

63 Y. Li, J. Li, X. Zhai, Y. Liu, G. Wang, X. Yang and G. Ge, *ACS Appl. Energy Mater.*, 2022, **5**, 13981–13989.

64 H. Yao, Y. Zheng, S. Yue, S. Hu, W. Yuan and X. Guo, *Inorg. Chem. Front.*, 2023, **10**, 804–814.

65 T. Wang, H. Chen, Z. Yang, J. Liang and S. Dai, *J. Am. Chem. Soc.*, 2020, **142**, 4550–4554.

66 P. A. Sukkurji, Y. Cui, S. Lee, K. Wang, R. Azmi, A. Sarkar, S. Indris, S. S. Bhattacharya, R. Kruk, H. Hahn, Q. Wang, M. Botros and B. Breitung, *J. Mater. Chem. A*, 2021, **9**, 8998–9009.

67 P. Yang, Y. An, C. Feng, Y. Liu, S. Liu, L. Gao, Y. Zhou, X. Li, P. Li and F. Zeng, *Int. J. Hydrogen Energy*, 2024, **51**, 1218–1228.

68 Z. Hao, Z. Du, T. Deng, D. Wang, Y. Zeng, S. Yu, Z. Meng, X. Hu, X. Hao and H. Tian, *J. Mater. Chem. A*, 2023, **11**, 22884–22890.

69 W. H. Baur and A. A. Khan, *Acta Crystallogr. B*, 1971, **27**, 2133–2139.

70 M. A. Hepworth, K. H. Jack, R. D. Peacock and G. J. Westland, *Acta Crystallogr.*, 1957, **10**, 63–69.

71 S. Thundiyil, S. Kurungot and R. N. Devi, *ACS Omega*, 2019, **4**, 31–38.

72 D. Kowalski, H. Kiuchi, T. Motohashi, Y. Aoki and H. Habazaki, *ACS Appl. Mater. Interfaces*, 2019, **11**, 28823–28829.

73 I. Yamada, M. Kinoshita, S. Oda, H. Tsukasaki, S. Kawaguchi, K. Oka, S. Mori, H. Ikeno and S. Yagi, *Chem. Mater.*, 2020, **32**, 3893–3903.

74 S. R. Ede, C. N. Collins, C. D. Posada, G. George, H. Wu, W. D. Ratcliff, Y. Lin, J. Wen, S. Han and Z. Luo, *ACS Catal.*, 2021, **11**, 4327–4337.

75 M. Leblanc, G. Ferey and R. de Pape, *Mater. Res. Bull.*, 1984, **19**, 1581–1590.

76 E. V. Peresypkina and V. A. Blatov, *Acta Crystallogr. Sect. B*, 2003, **59**, 361–377.

77 J. Kohl, D. Wiedemann, S. Nakhal, P. Bottke, N. Ferro, T. Bredow, E. Kemnitz, M. Wilkening, P. Heitjans and M. Lerch, *J. Mater. Chem.*, 2012, **22**, 15819–15827.

78 J. Kohl, D. Wiedemann, S. I. Troyanov, E. Palamidis and M. Lerch, *Dalton Trans.*, 2015, **44**, 13272–13281.

79 M. Leblanc, V. Maisonneuve and A. Tressaud, *Chem. Rev.*, 2015, **115**, 1191–1254.

80 D. H. McTaggart, J. D. Sundberg, L. M. McRae and S. C. Warren, *Sci. Data*, 2023, **10**, 90.

81 G. George, S. R. Ede and Z. Luo, *Fundamentals of Perovskite Oxides: Synthesis, Structure, Properties and Applications*, CRC Press, 2020.

82 D. Liu, P. Zhou, H. Bai, H. Ai, X. Du, M. Chen, D. Liu, W. F. Ip, K. H. Lo, C. T. Kwok, S. Chen, S. Wang, G. Xing, X. Wang and H. Pan, *Small*, 2021, **17**, 2101605.

83 H. J. Song, H. Yoon, B. Ju and D.-W. Kim, *Adv. Energy Mater.*, 2021, **11**, 2002428.

84 Y. Zhu, W. Zhou, Y. Zhong, Y. Bu, X. Chen, Q. Zhong, M. Liu and Z. Shao, *Adv. Energy Mater.*, 2017, **7**, 1602122.

85 G. George, S. L. Jackson, C. Q. Luo, D. Fang, D. Luo, D. Hu, J. Wen and Z. Luo, *Ceram. Int.*, 2018, **44**, 21982–21992.

86 W. Wang, M. Xu, X. Xu, W. Zhou and Z. Shao, *Angew. Chem., Int. Ed.*, 2020, **59**, 136–152.

87 G. George, S. R. Ede and Z. Luo, *Fundamentals of Perovskite Oxides: Synthesis, Structure, Properties and Applications*, CRC Press, Boca Raton, Florida, 2020.

88 N. Han, M. Race, W. Zhang, R. Marotta, C. Zhang, A. Bokhari and J. J. Klemeš, *J. Clean. Prod.*, 2021, **318**, 128544.

89 F. Zhang, Y. Mao, T.-J. Park and S. S. Wong, *Adv. Funct. Mater.*, 2008, **18**, 103–112.

90 W. Mi, C. Dai, S. Zhou, J. Yang, Q. Li and Q. Xu, *Mater. Lett.*, 2018, **227**, 66–69.

91 W. Rüdorff, G. Lincke and D. Babel, *Z. Anorg. Allg. Chem.*, 1963, **320**, 150–170.

92 L. Zhang, W. Cai and N. Bao, *Adv. Mater.*, 2021, **33**, 2100745.

93 Y. Sun and S. Dai, *Sci. Adv.*, 2021, **7**, eabg1600.

94 Z. Wang, J. You, Y. Zhao, R. Yao, G. Liu, J. Lu and S. Zhao, *J. Environ. Chem. Eng.*, 2023, **11**, 109080.

95 H. Han, J. Woo, Y.-R. Hong, Y.-C. Chung and S. Mhin, *ACS Appl. Energy Mater.*, 2019, **2**, 3999–4007.

96 H. Zhou, R. E. Ruther, J. Adcock, W. Zhou, S. Dai and J. Nanda, *ACS Nano*, 2015, **9**, 2530–2539.

97 S.-W. Kim, N. Pereira, N. A. Chernova, F. Omenya, P. Gao, M. S. Whittingham, G. G. Amatucci, D. Su and F. Wang, *ACS Nano*, 2015, **9**, 10076–10084.

98 K. Liang, L. Guo, K. Marcus, S. Zhang, Z. Yang, D. E. Perea, L. Zhou, Y. Du and Y. Yang, *ACS Catal.*, 2017, **7**, 8406–8412.

99 X. Yue, Y. Jin and P. K. Shen, *J. Mater. Chem. A*, 2017, **5**, 8287–8291.

100 N. Yamada, S. Kitano, Y. Yato, D. Kowalski, Y. Aoki and H. Habazaki, *ACS Appl. Energy Mater.*, 2020, **3**, 12316–12326.

101 K. Lemoine, Z. Gohari-Bajestani, R. Moury, A. Terry, A. Guiet, J.-M. Grenèche, A. Hémon-Ribaud, N. Heidary, V. Maisonneuve, N. Kornienko and J. Lhoste, *ACS Appl. Energy Mater.*, 2021, **4**, 1173–1181.

102 Z. Gohari-Bajestani, X. Wang, A. Guiet, R. Moury, J.-M. Grenèche, A. Hémon-Ribaud, Y. Zhang, D. Chartrand, V. Maisonneuve, A. Seifitokaldani, N. Kornienko and J. Lhoste, *Chem Catal.*, 2022, **2**, 1114–1127.

103 R. Mizuochi, K. Oka, Y. Inaguma and K. Maeda, *Sustain. Energy Fuels*, 2022, **6**, 2423–2427.

104 Y. Zhu, W. Dai, X. Zhong, T. Lu and Y. Pan, *J. Colloid Interface Sci.*, 2021, **602**, 55–63.

105 S. A. Patil, A. C. Khot, V. D. Chavan, I. Rabani, D. Kim, J. Jung, H. Im and N. K. Shrestha, *Chem. Eng. J.*, 2024, **480**, 146545.

106 S. Wang, C.-Z. Yuan, Y. Zheng, Y. Kang, K. S. Hui, K. Wang, H. Gao, D. A. Dinh, Y.-R. Cho and K. N. Hui, *ACS Catal.*, 2024, **14**, 3616–3626.

107 S. Zhang, Y. Xiao, Q. Feng and Z. Lei, *ACS Appl. Nano Mater.*, 2024, **7**, 8978–8987.

108 A. Terry, S. Mathiot, A. Guiet, E. Boivin, Z. Gohari-bajestani, V. Maisonneuve, A. Hémon-Ribaud, R. Moury, N. Kornienko and J. Lhoste, *ACS Appl. Energy Mater.*, 2024, DOI: 10.1021/acsaem.4c00259.

109 M. Jain, D. Gill, S. Monga and S. Bhattacharya, *J. Phys. Chem. C*, 2023, **127**, 15620–15629.

110 H. Wang, K. H. L. Zhang, J. P. Hofmann, V. A. de la, P. O'Shea and F. E. Oropeza, *J. Mater. Chem. A*, 2021, **9**, 19465–19488.

111 M. Chen, N. Kitiphatpiboon, C. Feng, A. Abudula, Y. Ma and G. Guan, *eScience*, 2023, **3**, 100111.

112 H. Sun, X. Xu, G. Chen and Z. Shao, *Carbon Energy*, 2024, e595.

113 C. Zhong, Z. Han, T. Wang, Q. Wang, Z. Shen, Q. Zhou, J. Wang, S. Zhang, X. Jin, S. Li, P. Wang, D. Gao, Y. Zhou and H. Zhang, *J. Mater. Chem. A*, 2020, **8**, 10831–10838.

114 C. Lyu, Y. Li, J. Cheng, Y. Yang, K. Wu, J. Wu, H. Wang, W.-M. Lau, Z. Tian, N. Wang and J. Zheng, *Small*, 2023, **19**, 2302055.

115 K. Kadakia, M. K. Datta, O. I. Velikokhatnyi, P. H. Jampani and P. N. Kumta, *Int. J. Hydrogen Energy*, 2014, **39**, 664–674.

116 S. D. Ghadge, P. P. Patel, M. K. Datta, O. I. Velikokhatnyi, R. Kuruba, P. M. Shanthi and P. N. Kumta, *RSC Adv.*, 2017, **7**, 17311–17324.

117 S. D. Ghadge, O. I. Velikokhatnyi, M. K. Datta, P. M. Shanthi, S. Tan, K. Damodaran and P. N. Kumta, *ACS Catal.*, 2019, **9**, 2134–2157.

118 S. D. Ghadge, O. I. Velikokhatnyi, M. K. Datta, P. M. Shanthi, S. Tan and P. N. Kumta, *ACS Appl. Energy Mater.*, 2020, **3**, 541–557.

119 G. Li, X. Xu, H. Liu, X. Yang and M.-C. Lin, *ChemCatChem*, 2022, **14**, e202201039.

120 H. Jia, X. Yang, X. Meng, G. Zhang and G. Li, *New J. Chem.*, 2023, **47**, 3658–3662.

121 F. Shamsi and M. Rezaei, *Colloids Surf. A Physicochem. Eng. Asp.*, 2023, **670**, 131608.

122 L. Zhang, Q. Xu, S. Wen, H. Zhang, L. Chen, H. Jiang and C. Li, *ACS Nano*, 2024, **18**, 22454–22464.

123 W. Xie, J. Huang, L. Huang, S. Geng, S. Song, P. Tsiakaras and Y. Wang, *Appl. Catal., B*, 2022, **303**, 120871.

124 P. Wang, Q. Cheng, C. Mao, W. Su, L. Yang, G. Wang, L. Zou, Y. Shi, C. Yan, Z. Zou and H. Yang, *J. Power Sources*, 2021, **502**, 229903.

125 H. Zeng, M. Oubla, X. Zhong, N. Alonso-Vante, F. Du, Y. Xie, Y. Huang and J. Ma, *Appl. Catal., B*, 2021, **281**, 119535.

126 J.-Y. Xie, R.-Y. Fan, J.-Y. Fu, Y.-N. Zhen, M.-X. Li, H.-J. Liu, Y. Ma, F.-L. Wang, Y.-M. Chai and B. Dong, *Int. J. Hydrogen Energy*, 2021, **46**, 19962–19970.

127 K. Xiao, Y. Wang, P. Wu, L. Hou and Z.-Q. Liu, *Angew. Chem., Int. Ed.*, 2023, **62**, e202301408.

128 B. Xiong, L. Ge, X. Lei, Y. Wang, J. Yang, W. Li, X. Li, Z. Cheng, Z. Fu and Y. Lu, *Sci. China Mater.*, 2023, **66**, 1793–1800.

129 Y.-G. Ji, J. Wu, H. Wen, S. Wang and L. Feng, *Chem. Eng. J.*, 2024, **496**, 154211.

130 X. Hong, Y. Gao, M. Ji, J. Li, L. Ding, Z. Yu and K. Chang, *J. Alloys Compd.*, 2024, **1007**, 176500.

131 J. Xiong, H. Zhong, J. Li, X. Zhang, J. Shi, W. Cai, K. Qu, C. Zhu, Z. Yang, S. P. Beckman and H. Cheng, *Appl. Catal., B*, 2019, **256**, 117817.

132 T. Wang, J. Fan, C.-L. Do-Thanh, X. Suo, Z. Yang, H. Chen, Y. Yuan, H. Lyu, S. Yang and S. Dai, *Angew. Chem., Int. Ed.*, 2021, **60**, 9953–9958.

133 J. Ran, L. Wang, M. Si, X. Liang and D. Gao, *Small*, 2023, **19**, 2206367.

134 K. Iwase, M. Ohtaka and I. Honma, *Chem. Mater.*, 2023, **35**, 2773–2781.

135 J. Kim, J. Lee, S. Kim and W. Jung, *Electron. Mater. Lett.*, 2024, **20**, 450–458.

136 X. Cao, Y. Hao, J. Zheng, H. Wang, Z. Lin, Y. Zhao, J. Liu, M. Zhang and Z. Shen, *Energy Fuels*, 2024, **38**, 8095–8102.

137 I. A. Cordova, Q. Peng, I. L. Ferrall, A. J. Rieth, P. G. Hoertz and J. T. Glass, *Nanoscale*, 2015, **7**, 8584–8592.

138 X. Lang, L. Chen, Y. Zhu, X. Liu, H. Guo, T. You and H. Zhang, *J. Phys. Chem. C*, 2023, **127**, 11932–11939.

139 P. Gayen, S. Saha and V. Ramani, *Acc. Chem. Res.*, 2022, **55**, 2191–2200.

140 G. A. Kaptagay, T. M. Inerbaev, Yu. A. Mastrikov, E. A. Kotomin and A. T. Akilbekov, *Solid State Ionics*, 2015, **277**, 77–82.

141 B. Modak and S. K. Ghosh, *J. Phys. Chem. C*, 2015, **119**, 7215–7224.

142 E. Fabbri, M. Nachtegaal, X. Cheng and T. J. Schmidt, *Adv. Energy Mater.*, 2015, **5**, 1402033.

143 X. Xu, Y. Pan, W. Zhou, Y. Chen, Z. Zhang and Z. Shao, *Electrochim. Acta*, 2016, **219**, 553–559.

144 T.-H. Shen, L. Spillane, J. Vavra, T. H. M. Pham, J. Peng, Y. Shao-Horn and V. Tileli, *J. Am. Chem. Soc.*, 2020, **142**, 15876–15883.

145 X. Xu, C. Su and Z. Shao, *Energy Fuels*, 2021, **35**, 13585–13609.

146 X. Han, P. Liu, R. Ran, W. Wang, W. Zhou and Z. Shao, *Mater. Today Energy*, 2022, **23**, 100896.

147 S. Wu, J. Liu, B. Cui, Y. Li, Y. Liu, B. Hu, L. He, M. Wang, Z. Zhang, K. Tian and Y. Song, *Electrochim. Acta*, 2019, **299**, 231–244.

148 K. Huang, Z. Zhao, H. Du, P. Du, H. Wang, R. Wang, S. Lin, H. Wei, Y. Long, M. Lei, W. Guo and H. Wu, *ACS Sustain. Chem. Eng.*, 2020, **8**, 6905–6913.

149 H. Li, G. Yan, H. Zhao, P. C. Howlett, X. Wang and J. Fang, *Adv. Mater.*, 2024, **36**, 2311272.

150 P. Ji, D. Zheng, H. Jin and Y. Liao, *Int. J. Hydrogen Energy*, 2024, **57**, 473–480.

151 S. V. Devaguptapu, S. Hwang, S. Karakalos, S. Zhao, S. Gupta, D. Su, H. Xu and G. Wu, *ACS Appl. Mater. Interfaces*, 2017, **9**, 44567–44578.

152 H. Yu, J. Ke and Q. Shao, *Small*, 2023, **19**, 2304307.

153 A. Raza, J. Z. Hassan, U. Qumar, A. Zaheer, Z. U. D. Babar, V. Iannotti and A. Cassinese, *Mater. Today Adv.*, 2024, **22**, 100488.

154 T.-W. Chen, S.-M. Chen, G. Anushya, R. Kannan, P. Veerakumar, M. M. Alam, S. Alargarsamy and R. Ramachandran, *Nanomaterials*, 2023, **13**, 2012.

155 S. Anantharaj, K. Karthick and S. Kundu, *Mater. Today Energy*, 2017, **6**, 1–26.

156 Y. Chen, K. Rui, J. Zhu, S. X. Dou and W. Sun, *Chem.–Eur. J.*, 2019, **25**, 703–713.

157 L. Yang, Z. Liu, S. Zhu, L. Feng and W. Xing, *Mater. Today Phys.*, 2021, **16**, 100292.

158 Z. Yu, Y. Bai, G. Tsekouras and Z. Cheng, *Nano Sel.*, 2022, **3**, 766–791.

159 B. Guo, H. Huo, Q. Zhuang, X. Ren, X. Wen, B. Yang, X. Huang, Q. Chang and S. Li, *Adv. Funct. Mater.*, 2023, **33**, 2300557.

160 S. Nagappan, A. Karmakar, R. Madhu, H. N. Dhandapani, S. S. Roy and S. Kundu, *Catal. Sci. Technol.*, 2023, **13**, 6377–6391.

161 N. Hussain, W. Yang, J. Dou, Y. Chen, Y. Qian and L. Xu, *J. Mater. Chem. A*, 2019, **7**, 9656–9664.

162 J. Lv, X. Yang, K. Li, X. Chen, S. Sun, H.-Y. Zang, Y.-F. Chang, Y.-H. Wang and Y.-G. Li, *Nanoscale Adv.*, 2019, **1**, 4099–4108.

163 Y. Li, X. Zhai, C. Fan, X. Chen, Y. Liu, J. Yang, L. Chen, G. Ge and J. Zhang, *J. Mater. Chem. A*, 2022, **10**, 11774–11783.

164 J. Anthuvan Rajesh, S.-H. Kang and K.-S. Ahn, *Mater. Lett.*, 2022, **308**, 131207.

165 C. Greaves and M. A. Thomas, *Acta Crystallogr. Sect. B*, 1986, **42**, 51–55.

166 K. Lawson, S. P. Wallbridge, A. E. Catling, C. A. Kirk and S. E. Dann, *J. Mater. Chem. A*, 2023, **11**, 789–799.

167 H. Bode, K. Dehmelt and J. Witte, *Electrochim. Acta*, 1966, **11**, 1079–1087.

168 K. I. Pandya, W. E. O'Grady, D. A. Corrigan, J. McBreen and R. W. Hoffman, *J. Phys. Chem.*, 1990, **94**, 21–26.

169 D. S. Hall, D. J. Lockwood, C. Bock and B. R. MacDougall, *Proc. R. Soc. A*, 2015, **471**, 20140792.

170 W. D. Birch, A. Pring, A. Reller and H. W. Schmalle, *Am. Mineral.*, 1993, **78**, 827–834.

171 K. Cysewska, M. Zając, M. Łapiński, J. Karczewski, M. K. Rybarczyk, B. Kamecki, P. Jasiński and S. Molin, *Energy Technol.*, 2021, **9**, 2100688.

172 S. J. Patil, N. R. Chodankar, S.-K. Hwang, G. S. Rama Raju, Y.-S. Huh and Y.-K. Han, *Small*, 2022, **18**, 2103326.

173 P. Muthukumar, P. Nantheeswaran, M. Mariappan, M. Pannipara, A. G. Al-Sehemi and S. P. Anthony, *Dalton Trans.*, 2023, **52**, 4606–4615.

174 L. Li, J. Wu, L. Huang, G. Lan, N. Wang, H. Zhang, X. Chen and X. Ge, *New J. Chem.*, 2022, **46**, 20490–20496.

175 J. Yu, J. Li, R.-T. Gao, Y. Yang and L. Wang, *Small*, 2024, **20**, 2310642.

176 T. Watanabe, K. Tsuchimoto, T. Fukushima, K. Murakoshi, M. Mizuhata and H. Minamimoto, *Sustain. Energy Fuels*, 2024, **8**, 4813–4819.

177 G. Fan, F. Li, D. G. Evans and X. Duan, *Chem. Soc. Rev.*, 2014, **43**, 7040–7066.

178 Z. Liu, C.-L. Dong, Y.-C. Huang, J. Cen, H. Yang, X. Chen, X. Tong, D. Su, Y. Wang and S. Wang, *J. Mater. Chem. A*, 2019, **7**, 14483–14488.

179 S. Cai, H. Liu, H. Cheng, B. Sun, W. Xia, H. Hu and S. Zhou, *ACS Appl. Nano Mater.*, 2023, **6**, 7864–7872.

180 C. Wu, H. Li, Z. Xia, X. Zhang, R. Deng, S. Wang and G. Sun, *ACS Catal.*, 2020, **10**, 11127–11135.

181 F. Dionigi, Z. Zeng, I. Sinev, T. Merzdorf, S. Deshpande, M. B. Lopez, S. Kunze, I. Zegkinoglou, H. Sarodnik, D. Fan, A. Bergmann, J. Drnec, J. F. de Araujo, M. Gliech, D. Teschner, J. Zhu, W.-X. Li, J. Greeley, B. R. Cuenya and P. Strasser, *Nat. Commun.*, 2020, **11**, 2522.

182 C. Pei, Y. Gu, Z. Liu, X. Yu and L. Feng, *ChemSusChem*, 2019, **12**, 3849–3855.

183 M. Li, Y. Gu, Y. Chang, X. Gu, J. Tian, X. Wu and L. Feng, *Chem. Eng. J.*, 2021, **425**, 130686.

184 Z. Zhai, W. Yan and J. Zhang, *Nanoscale*, 2022, **14**, 4156–4169.

185 Y. Yang, Y. Wu, D. Guo and L. Liu, *Appl. Surf. Sci.*, 2024, **644**, 158810.

186 M.-J. Pei, Y.-K. Shuai, X. Gao, J.-C. Chen, Y. Liu, W. Yan and J. Zhang, *Small*, 2024, **20**, 2400139.

187 A. V. der Ven, D. Morgan, Y. S. Meng and G. Ceder, *J. Electrochem. Soc.*, 2005, **153**, A210.

188 P. W. Menezes, S. Yao, R. Beltrán-Suito, J. N. Hausmann, P. V. Menezes and M. Driess, *Angew. Chem.*, 2021, **133**, 4690–4697.

189 J. Wang, L. A. Zhang, Y. Ren and P. Wang, *Electrochim. Acta*, 2023, **437**, 141475.

190 J. Wang, Y. Ren and P. Wang, *J. Mater. Chem. A*, 2023, **11**, 4619–4626.

191 K. Guo, J. Jia, X. Lu, S. Wang, H. Wang, H. Wu and C. Xu, *Inorg. Chem. Front.*, 2024, **11**, 1479–1491.

192 G.-F. Chen, Y. Luo, L.-X. Ding and H. Wang, *ACS Catal.*, 2018, **8**, 526–530.

193 L. Chen, J. Chang, Y. Zhang, Z. Gao, D. Wu, F. Xu, Y. Guo and K. Jiang, *Chem. Commun.*, 2019, **55**, 3406–3409.

194 M. Nishimoto, S. Kitano, D. Kowalski, Y. Aoki and H. Habazaki, *ACS Sustain. Chem. Eng.*, 2021, **9**, 9465–9473.

195 B. M. Kathale, H. Xiao, S. Yang, H. Yin, T. Yu, X. Zhou, L. Qian, J. Xiao, P. Lei and X. Li, *Electrochim. Acta*, 2022, **406**, 139831.

196 Y. Jang, S. Ha, H.-T. Lim and S. Lee, *Chem. Commun.*, 2023, **59**, 8298–8301.

197 M. Shamloofard and S. Shahrokhian, *Inorg. Chem.*, 2023, **62**, 1178–1191.

198 M. Feng, J. Huang, Y. Peng, C. Huang, X. Yue and S. Huang, *ACS Nano*, 2022, **16**, 13834–13844.

199 X. Bai, Q. Wang, G. Xu, Y. Ning, K. Huang, F. He, Z. Wu and J. Zhang, *Chem.–Eur. J.*, 2017, **23**, 16862–16870.

200 X. Chen, M. Wei and J. Zhou, *J. Mater. Chem. A*, 2021, **9**, 22626–22634.

201 Z. Hou, Y. Zhu, W. Du, X. Jia, T. Huang and K.-J. Huang, *J. Ind. Eng. Chem.*, 2022, **112**, 85–95.

202 J. Zhu, X. Zheng, C. Liu, Y. Lu, Y. Liu, D. Li and D. Jiang, *J. Colloid Interface Sci.*, 2023, **630**, 559–569.

203 J. Zhu, J. Chi, T. Cui, L. Guo, S. Wu, B. Li, J. Lai and L. Wang, *Appl. Catal., B*, 2023, **328**, 122487.

204 X. Sun, S. Song, G. Yan, Y. Liu, H. Ding, X. Zhang and Y. Feng, *Dalton Trans.*, 2024, **53**, 8843–8849.

205 P. Hao, W. Zhu, F. Lei, X. Ma, J. Xie, H. Tan, L. Li, H. Liu and B. Tang, *Nanoscale*, 2018, **10**, 20384–20392.

206 W. He, L. Han, Q. Hao, X. Zheng, Y. Li, J. Zhang, C. Liu, H. Liu and H. L. Xin, *ACS Energy Lett.*, 2019, **4**, 2905–2912.

207 H. Kim, K. Min, G. Song, J. Kim, H. C. Ham and S.-H. Baeck, *J. Colloid Interface Sci.*, 2024, **665**, 922–933.

208 K. Li, Y. Tong, D. Feng and P. Chen, *J. Colloid Interface Sci.*, 2022, **625**, 576–584.

209 S. T. Hunt, T. Nimmanwudipong and Y. Román-Leshkov, *Angew. Chem., Int. Ed.*, 2014, **53**, 5131–5136.

210 Y. Xiao, J.-Y. Hwang and Y.-K. Sun, *J. Mater. Chem. A*, 2016, **4**, 10379–10393.

211 Q. Gao, W. Zhang, Z. Shi, L. Yang and Y. Tang, *Adv. Mater.*, 2019, **31**, 1802880.

212 X. Wu, S. Zhou, Z. Wang, J. Liu, W. Pei, P. Yang, J. Zhao and J. Qiu, *Adv. Energy Mater.*, 2019, **9**, 1901333.

213 H. Wang, S. Zhu, J. Deng, W. Zhang, Y. Feng and J. Ma, *Chin. Chem. Lett.*, 2021, **32**, 291–298.

214 Y. Yu, J. Zhou and Z. Sun, *Adv. Funct. Mater.*, 2020, **30**, 2000570.

215 J. Chen, B. Ren, H. Cui and C. Wang, *Small*, 2020, **16**, 1907556.

216 Y. Wang, Q. Wu, B. Zhang, L. Tian, K. Li and X. Zhang, *Catalysts*, 2020, **10**, 1164.

217 X. Yue, C. He, C. Zhong, Y. Chen, S. P. Jiang and P. K. Shen, *Adv. Mater.*, 2016, **28**, 2163–2169.

218 R. S. Ningthoujam and N. S. Gajbhiye, *Prog. Mater. Sci.*, 2015, **70**, 50–154.

219 Y. Zhang, B. Ouyang, J. Xu, G. Jia, S. Chen, R. S. Rawat and H. J. Fan, *Angew. Chem.*, 2016, **128**, 8812–8816.

220 Z. Meng, S. Zheng, R. Luo, H. Tang, R. Wang, R. Zhang, T. Tian and H. Tang, *Nanomaterials*, 2022, **12**, 2660.

221 Y. Lu, Z. Li, Y. Xu, L. Tang, S. Xu, D. Li, J. Zhu and D. Jiang, *Chem. Eng. J.*, 2021, **411**, 128433.

222 L. Yang, L. Zhang, Y. Li, B.-H. Lee, J. Kim, H. S. Lee, J. Bok, Y. Ma, W. Zhou, D. Yuan, A.-L. Wang, M. S. Bootharaju, H. Zhang, T. Hyeon and J. Chen, *J. Am. Chem. Soc.*, 2024, **146**, 12556–12564.

223 X. Chen, X. Yu, G. Zhang, S. Wei, Y. Huang, H. Wang, J. Jiang, Z. Ma and Q. Li, *J. Electroanal. Chem.*, 2024, **958**, 118162.

224 G. Zhang, Z.-A. Lan and X. Wang, *Chem. Sci.*, 2017, **8**, 5261–5274.

225 J. Wu, Z. Liu, X. Lin, E. Jiang, S. Zhang, P. Huo, Y. Yan, P. Zhou and Y. Yan, *Nat. Commun.*, 2022, **13**, 6999.

226 K. Liu, C. Zhang, Y. Sun, G. Zhang, X. Shen, F. Zou, H. Zhang, Z. Wu, E. C. Wegener, C. J. Taubert, J. T. Miller, Z. Peng and Y. Zhu, *ACS Nano*, 2018, **12**, 158–167.

227 W. Wu, S. Luo, Y. Huang, H. He, P. K. Shen and J. Zhu, *Mater. Chem. Front.*, 2024, **8**, 1064–1083.

228 K. Chen, Y. Li, G. Wu, Q. Wang, C. Fan, L. Zhang and S. Han, *Int. J. Hydrogen Energy*, 2024, **51**, 1421–1428.

229 Y. Guo, T. Park, J. W. Yi, J. Henzie, J. Kim, Z. Wang, B. Jiang, Y. Bando, Y. Sugahara, J. Tang and Y. Yamauchi, *Adv. Mater.*, 2019, **31**, 1807134.

230 P. Stelmachowski, J. Duch, D. Sebastián, M. J. Lázaro and A. Kotarba, *Materials*, 2021, **14**, 4984.

231 L. Zhang, J. Xiao, H. Wang and M. Shao, *ACS Catal.*, 2017, **7**, 7855–7865.

232 L. Li, H. Yang, J. Miao, L. Zhang, H.-Y. Wang, Z. Zeng, W. Huang, X. Dong and B. Liu, *ACS Energy Lett.*, 2017, **2**, 294–300.

233 J. Zhang and L. Dai, *Angew. Chem., Int. Ed.*, 2016, **55**, 13296–13300.

234 X. Yue, S. Huang, J. Cai, Y. Jin and P. K. Shen, *J. Mater. Chem. A*, 2017, **5**, 7784–7790.

235 J. Kim, R. Zhou, K. Murakoshi and S. Yasuda, *RSC Adv.*, 2018, **8**, 14152–14156.

236 C. Xing, Y. Xue, B. Huang, H. Yu, L. Hui, Y. Fang, Y. Liu, Y. Zhao, Z. Li and Y. Li, *Angew. Chem., Int. Ed.*, 2019, **58**, 13897–13903.

237 J. Kim, T. Fukushima, R. Zhou and K. Murakoshi, *Materials*, 2019, **12**, 211.

238 Y. Sim, S. J. Kim, G. Janani, Y. Chae, S. Surendran, H. Kim, S. Yoo, D. C. Seok, Y. H. Jung, C. Jeon, J. Moon and U. Sim, *Appl. Surf. Sci.*, 2020, **507**, 145157.

239 Z. Ali, M. Mehmood, J. Ahmad, A. Fatima and M. Ali, *J. Appl. Electrochem.*, 2021, **51**, 1573–1581.

240 M. Tan, Q. Wang, S. Wang, W. Liu, D. Wang, S. Luo, P. Hou, M. Zhou, Y. Zhang, S. Yan and X. Liu, *J. Electrochem. Soc.*, 2022, **169**, 096517.

241 Y. An, Z. Ren, Y. Kong, Y. Tian, B. Jiang and F. Shaik, *Int. J. Hydrogen Energy*, 2024, **58**, 633–645.

242 A. Muthurasu, I. Pathak, D. Acharya, Y. R. Rosyara and H. Y. Kim, *J. Mater. Chem. A*, 2024, **12**, 1826–1839.

243 M. Nadeem, A. Ulfat, A. Kumar, M. H. Bhatti, F. Rabani, U. Yunus, M. Aamir, M. Sher, K. M. Alotaibi and G. Yasin, *Int. J. Hydrogen Energy*, 2024, **53**, 457–467.

244 Z. Luo, A. Oki, L. Carson, L. Adams, G. Neelgund, N. Soboyejo, G. Regisford, M. Stewart, K. Hibbert, G. Beharie, C. Kelly-Brown and P. Traisawatwong, *Chem. Phys. Lett.*, 2011, **513**, 88–93.

245 Q. Hu, G. Li, Z. Han, Z. Wang, X. Huang, H. Yang, Q. Zhang, J. Liu and C. He, *J. Mater. Chem. A*, 2019, **7**, 14380–14390.

246 A. I. Douka, H. Yang, L. Huang, S. Zaman, T. Yue, W. Guo, B. You and B. Y. Xia, *EcoMat*, 2021, **3**, e12067.

247 W. Li, C. Wang and X. Lu, *J. Mater. Chem. A*, 2021, **9**, 3786–3827.

248 M. Zha, C. Pei, Q. Wang, G. Hu and L. Feng, *J. Energy Chem.*, 2020, **47**, 166–171.

249 X. Gu, C. Wu, S. Wang and L. Feng, *Catal. Commun.*, 2022, **162**, 106394.

250 Y. Zhou, H. Liu, X. Gu, X. Wu and L. Feng, *Carbon Energy*, 2022, **4**, 924–938.

251 M. Li, S. Wang, X. Wang, X. Tian, X. Wu, Y. Zhou, G. Hu and L. Feng, *Chem. Eng. J.*, 2022, **442**, 136165.

252 K. Lu, Z. Wang, Y. Wu, X. Zhai, C. Wang, J. Li, Z. Wang, X. Li, Y. He, T. An, K. Yang, D. Yang, F. Yu and B. Dai, *Chem. Eng. J.*, 2023, **451**, 138590.

253 Y. Kuang, R. He, X. Gu, F. Yang, X. Tian and L. Feng, *Chem. Eng. J.*, 2023, **456**, 141055.

254 P. Muthukumar, P. Nantheeswaran, M. Mariappan, M. Pannipara, A. G. Al-Sehemi and S. P. Anthony, *Dalton Trans.*, 2023, **52**, 3877–3883.

255 X. He, L. Chang, H. Wu, G. Liu, Y. Zhang and A. Zhou, *J. Alloys Compd.*, 2023, **967**, 171709.

256 A. M. Tarigan, S. Aulia, M. Rinawati, L.-Y. Chang, Y.-S. Cheng, C.-C. Chang, W.-H. Huang, J.-L. Chen, H. Setyawan and M.-H. Yeh, *Chem. Eng. J.*, 2023, **476**, 146754.

257 Y. Lu, X. Han, Y. Zhang and X. Yu, *Nanomaterials*, 2024, **14**, 16.

258 D. Liu, Z. Qian, Y. Li, Y. Luo, C. Liu and J. Cui, *Adv. Sustainable Syst.*, 2024, **8**, 2300594.

259 Y. Lu, C. Pei, X. Han, Y. Li, H. S. Park, J. K. Kim and X. Yu, *J. Electroanal. Chem.*, 2024, **957**, 118108.

260 Z. Ma, J. Wu, F. Yang, S. Wang, H. Wen and L. Feng, *Chem. Eng. J.*, 2024, **491**, 152113.

261 G. Wang, H. Chi, Y. Feng, J. Fan, N. Deng, W. Kang and B. Cheng, *J. Mater. Chem. A*, 2024, **12**, 19109–19122.

262 R. A. Borse, M. B. Kale, S. H. Sonawane and Y. Wang, *Adv. Funct. Mater.*, 2022, **32**, 2202570.

263 B. B. Xiao, L. Yang, H. Y. Liu, X. B. Jiang, B. Aleksandr, E. H. Song and Q. Jiang, *Appl. Surf. Sci.*, 2021, **537**, 147846.